MICROSCOPY SOCIETY OF SOUTHERN AFRICA

PROCEEDINGS VOLUME 50, 2024

UNIVERSITY OF THE FREE STATE, BLOEMFONTEIN

THE MICROSCOPY SOCIETY OF SOUTHERN AFRICA

www.microscopy.co.za

The aim of the Society is to promote and develop microscopy and associated techniques at all levels in the South African region.

The Society was founded as the Electron Microscopy Society of Southern Africa (EMSSA) in 1962 and became a formal member of IFSM (the International Federation of Societies for Microscopy) in 1966. The Society changed its name to the Microscopy Society of Southern Africa (MSSA) in 1996 to accommodate all forms of microscopy

The primary objectives of the Society are:

- To further microscopy in the broadest sense all branches of science,
- To facilitate communication and co-operation between microscopists and with other scientists,
- To act as a liaison between members of the Society and IFSM,
- To provide an interface between research, education, government and the public.

This is achieved mainly through:

- an annual meeting of the Society,
- publication of a Newsletter,
- maintenance of an Instrument and Skills database,
- the establishment of regional groups to promote closer co-operative ties.
- an email list server: massa@kendy.up.ac.za

Honorary Members:

Prof B I Balinsky, Prof P Berjak, Prof J Coetzee, Dr N R Comins, Mr R H M Cross, Prof JAA Engelbrecht, Dr J T, Fourie, Mr D Geppert, Mr A N Hall, Mr L Harmsen Prof ME Lee, Dr J Murphy, Prof F Nabarro, Prof JH Neethling, Prof B T Sewell, Prof J T Soley, Dr E M Veenstra, Prof T A Villiers, Dr J Wesley-Smith, Prof H Wilsdorf, Prof M J Witcomb, Dr S Wolfe-Coote, Dr A Yarwood.

Cover Micrograph: High Angle Annular Darkfield Scanning Transmission Electron Micrograph of Au-Ni-Pt Core-Shell Nanoparticles

Image taken by Dr G. Marx from Nelson Mandela University

MICROSCOPY SOCIETY OF SOUTHERN AFRICA

MIKROSKOPIEVERENIGING VAN SUIDELIKE AFRIKA

UMBUTHO WABAKOPOLI BAMAZANTSI E-AFRIKA

PROCEEDINGS
VERRIGTINGE
INKQUBO-NGXOXO

VOLUME, UMQULU 50, 2024

UNIVERSITY OF THE FREE STATE, BLOEMFONTEIN

The 58th Annual Conference was held at the University of the Free State, Bloemfontein from 2 to 5 December 2024.

This volume contains the Proceedings of the Microscopy Society of Southern Africa and is published annually to coincide with the conferences of the Society. The Society does not hold itself responsible for errors in the manuscripts and does not necessarily subscribe to the opinions and conclusions of the authors.

Die 58ste Jaarlikse Konferensie het by die Universiteit van die Vrystaat, Bloemfontein plaasgevind vanaf 2 – 5 Desember 2024.

Hierdie volume bevat die Verrigtinge van die Mikroskopievereniging van Suidelike Afrika en word uitgegee om met die konferensies van die Vereniging saam te val. Die Vereniging aanvaar nie verantwoordelikeheid vir foute in die manuskripte nie en stem ook nie noodwendig met die menings en gevolgtrekkings van die outeurs saam nie.

Ingqungquthela yeminyaka yama 58 eyayibanjwelwe kwiziko lengqunqguthela lase University of the Free State, kwisixeko sase Bloemfontein ukusuka kumhla we 2 ukuyokuma kowe 5 kweyoMnga ngonyaka wama 2024.

Lomqulu uqulethe inkqubo-ngxoxo zendibano yequmrhu leziKopoli zase maZantsi e-Afrika epapashwa ngonyaka ukuze ingqamane nale ngqungquthela yeliqumrhu. Eliqumrhu liyazikhulula kwiimpazamo ezingakho kwiingqokelela zeentetho ezikulo mqulu kwaye ungarhumi nezimvo nezigqibo zababhali.

Published by the Microscopy Society of Southern Africa, c/o Lab for Microscopy & Microanalysis, University of Pretoria, Hatfield campus, Pretoria, 0002

MICROSCOPY SOCIETY OF SOUTHERN AFRICA
FIFTY EIGHTH ANNUAL CONFERENCE: 2024

Table of Contents

Invited Lectures

Forty Second John Matthews Memorial Lecture 1
J.K.N. Lindner

Thirty-fifth Boris Balinsky Lecture 2
L. Joubert

Life Sciences

AUTOPHAGY AND MITOCHONDRIAL QUALITY CONTROL ARE KEY PARAMETERS IN THE CELLULAR PATHOLOGY OF ALZHEIMER'S DISEASE 4
B. Loos

MODELING SCHIZOPHRENIA ENDOPHENOTYPES IN Drosophila melanogaster: EFFECTS OF KETAMINE ON NEUROINFLAMMATORY AND NEURODEGENERATIVE RESPONSES 5
A.A. Bello and R.O. Folarin

Nigella sativa OIL MITIGATES THALAMIC AND SUBICULAR DYSFUNCTION IN PENTYLENETETRAZOLE INDUCED EPILEPTOGENESIS IN BALB/C MICE 6
B.M. David and R.O. Folarin

PROBING AUTOPHAGY: COMPARING PLASMIDS, TECHNIQUES AND THE QUEST FOR AN AUTOMATED CLEM ALGORITHM 7
N. Vahrmeijer, E. Sharrat, J. Conradie, L. Engelbrecht, R. Theart and B. Loos

A NOVEL METASYSTEMS CLASSIFIER FOR PLATELET FRAGILITY AND MORPHOLOGY ANALYSIS 8
C. Venter, J.H. Pretorius, D.B. Kell and E. Pretorius

THE EX VIVO EFFECTS OF Bitis arietans AND Naja mossambica VENOM ON BLOOD COAGULOPATHY 9
C. Megaw, J. Bester and M.A. Strydom

MORPHOLOGICAL CHANGES INDUCED BY THE IMIDACLOPRID, USING A RAT LEYDIG CELL LINE (LC-540) 10
M.I.A. Ibrahim, G.C.H. Ferreira, E.A. Venter and C.J. Botha

IMMUNOHISTOCHEMISTRY EVALUATION OF SATELLITE CELL ACTIVATION STATUS IN EXERCISED AND CONTRALATERAL UNEXERCISED MUSCLE 11
M.L. Cowley and K.H. Myburgh

INCREASING THE THERMOSTABILITY OF A CYANIDE-CONVERTING NITRILASE 12
B.T. Sewell, L.S. Dlamini, J.D. Woodward, A.E. Mulelu, J. Reitz and A. Frangakis

AN AGE-OLD MYSTERY: THE SPIKE ON THE LION'S (Panthera leo) TAIL 13
J.R. Dirsuwei, M.R. Crole and S.J. Clift

TAXONOMIC ANALYSIS OF CALANOID COPEPODS IN SOUTH AFRICAN LENTIC ECOSYSTEMS USING SCANNING ELECTRON MICROSCOPY 14
A.X. Kruger, C. Jansen van Rensburg and L.L. Van As

MICROMORPHOLOGY AND ANATOMY OF Tabernaemontana ventricosa (FOREST TOAD TREE) FLORAL COMPONENTS 15

C.M. Naidoo, Y. Naidoo and N.M. Mkolo

POLLINATOR REWARDS IN Nemesia (SCROPHULARIACEAE) 16

H. Grobler, M. Jackson and L. Joubert

POSTERS

INVESTIGATION OF THE EFFECT OF PEG-AuNPs ON COLORECTAL CANCER CELL LINE 17

D. Basson, S. Roux and J. Wesley-Smith

HISTOLOGICAL EFFECTS OF CTCE-9908 AND L-KYNURENINE ON MELANOMA METASTASIS IN A XENOGRAFT MOUSE MODEL 18

M.J. Olfsen, P. Bipath, Y.N. Hlophe and J.C. Serem

HIPPOCAMPAL VULNERABILITIES IN MATERNAL BRAINS: EFFECTS OF INTRAUTERINE GROWTH RESTRICTION IN ADULT FEMALE MICE 19

T.A. Yusuf, R.B. Bamidele, A.A. Bello and P.D. Shallie

BACK TO BASICS WHEN MOLECULAR SEQUENCES ARE NOT IN PLACE, YET 20

L.L. Van As and K.W. Christison

Materials Sciences

CHARACTERISATION OF STEEL MARTENSITE USING ELECTRON BACKSCATTERED DIFFRACTION 21

S. Allies, R.D. Knutsen and J.E. Westraadt

EFFECT OF WELDING ON SECONDARY PHASES IN SERVICE-EXPOSED 12%Cr TMF STEEL 22

G Marx, J.E. Westraadt and E.J. Olivier

DISLOCATION DENSITY MEASUREMENT IN AISI316L STAINLESS STEEL USING ELECTRON CHANNELING CONTRAST IMAGING (ECCI) 23

L. C. M. Pullen, J.E. Westraadt, R.D. Knutsen and D. Ramasimong

MICROSTRUCTURE AND TENSILE PROPERTY EVOLUTION IN TEMPERED Ti-6Al-4VxH MARTENSITE 24

V.N. Vilane, R.D. Knutsen and J.E. Westraadt

MICROSTRUCTURE-BASED CREEP LIFE ASSESSMENT OF 1CrMoV TURBINE ROTORS AFTER PROLONGED SERVICE 25

H.S. Nyembe and J.E. Westraadt

PREVENTION OF HYDROGEN PICKUP DUE TO THE CHROMIUM DOPING OF THE ZrO2 LAYER ON ZIRLO 26

S. Ngongo, A. Janse van Vuuren, J.H. Neethling and V. Uglov

CORRELATION BETWEEN HOMOGENISATION PARAMETERS AND PROPERTY EVOLUTION OF AA3104 CBS AFTER HOT FINISH ROLLING 27

K.E. Lebakeng

PRINTABILITY AND PROPERTIES OF WC-12Co/Mo CEMENTED CARBIDE USING DIRECT INK WRITING 28

N.P. Mphasha, R.M. Genga, C. Polese, N. Sacks, J. Vleugels, S. Huang and S. Ngongo

ENERGY CONSUMPTION OF NBC BASED INSERTS DURING FACE MILLING OF AUTOMOTIVE GCI

M.S. Rabothata, R.M. Genga, N.P. Mphasha, K. Phaka, C. Polese, P. Zeman, S. Huang, J. Vleugels and S. Ngongo

CIRCULAR MANUFACTURING OF FE AND DUPLEX STEEL-BONDED WC HARDMETALS FOR AEROSPACE-GRADE AA7010-T7651 FACE-MILLING 30

R.M. Genga, N.P. Mphasha, T. Nhlanhla, G. Peters, D.E.P. Klenam, M.O. Bodunrin, T. Steenkamp,C. Polese and A. Janse van Vuuren

INVESTIGATION OF 1D BATIO3/CD0.5ZN0.5S HETEROSTRUCTURE FOR PIEZO-PHOTOCATALYTIC REMOVAL ORGANIC POLLUTANTS 31

T.T. Mohlala, T.L. Yusuf, M. Masukume, V. Ojijo and N. Mabuba

ESTABLISHING THE CO-EXISTENCE OF METAL OXIDES IN NANOSTRUCTURED COBALT OXIDEBASED GAS SENSORS. 32

R. Makole, H.C. Swart and D.E. Motaung

IMPACT OF USING CAPPING LIGANDS ON THE EMULSION-LARP SYNTHESIS OF CESIUM LEAD BROMIDE NANOCRYSTALS 33

G.B. Nair, S. Tamboli and H.C. Swart

COMPETITIVE ADSORPTION OF CADMIUM AND MERCURY FROM WATER BY AgNP-NATURAL RUBBER/POLYVINYL ALCOHOL NANOFIBRE COMPOSITE 34

L.B Osei, S. Fosu and S.A. Ndur

ENCAPSULATION OF Eu-Si QDs IN ZEOLITIC IMIDAZOLE FRAMEWORK-8 (ZIF-8) FOR PHOTOLUMINESCENCE TUNING 35

S.J. Panchu, S.E. Punchu, M.M. Duvenhage and H C Swart

SURFACE MODIFICATION AND CATHODOLUMINESCENCE DEGRADATION OF Y2O3:Dy3+, Sm3+ THIN FILM 36

S. Nagarasanakote Jayaramu, E. Coetsee and H.C. Swart

STUDYING RECRYSTALLISATION DYNAMICS OF SWIFT HEAVY ION TRACKS IN YIG 37

M.M. Badenhorst, E.J. Olivier and J.H. O'Connell

THE MICROSTRUCTURAL RESPONSE OF POLYCRYSTALLINE Si3N4 WITH VARYING ALIMPURITY 38

CONCENTRATIONS TO SWIFT HEAVY IONS.

A. Janse van Vuuren, V.A. Skuratov and A. Ibrayeva

TEM ANALYSIS OF THE TETRAGONAL PHASE FRACTION FORMATION IN MONOCLINIC 39

ZIRCONIA AT INTERMEDIATE SHI FLUENCES

M.E. Lee, J.H. O'Connell and V. Skuratov

REAL-TIME OBSERVATION OF MOLECULAR DYNAMICS AND CHEMICAL REACTIONS IN STEM 40

R.R. Zamani, C. Ozsoy-Keskinbora, P. Longo, E. van Cappellen, I. Lazic and S. Lazar

3D RGO HYBRID EVAPORATOR FOR EFFICIENT SOLAR DESALINATION 41

W.J. Lawrence, F.A. Bezza, S.M. Tichapondwa and E.M.N. Chirwa

ASSESSMENT OF CREEP CAVITATION IN SERVICE-EXPOSED 12%Cr TMF STEEL 42

G. Marx, N.W. Mfuma and J.E. Westraadt

IDENTIFICATION OF COPPER AND COBALT-BEARING MINERALS IN COPPER SLAG 43

T.Z. Papo, M.M. Ramakokovhu and J. Mulwanda

COBALT-BASED PEROVSKITE OXIDE CATALYSTS FOR THE PREFERENTIAL OXIDATION OF CARBON MONOXIDE FOR HYDROGEN FUEL CELLS 44

N. Ndila and P.J. Kooyman

RECOVERY OF IRON FROM ROAST-LEACH TITANOMAGNETITE FERROVANADIUM RESIDUE 45

M. Nevondo, L. Koech, M.M. Ramakokovhu, B.M. Sesane and B. Msiza

CONTRAST OPTIMIZATION AIDED BY MACHINE LEARNING APPLIED TO VIRTUAL 4D-STEM IMAGES 46

D.G. Stroppa and R. dos Reis

MEASURING GEOMETRICALLY NECESSARY DISLOCATION DENSITY IN THE SEM USING EBSD: TRUE OR FALSE? 47

R.D. Knutsen

INVESTIGATING EFFECTS OF INTER-PASS TIME DURING HOT FINISH ROLLING ON THE TEXTURE EVOLUTION OF AA3104 CBS 48

N.A Chaole

MORPHOLOGICAL AND PHASE STABILITY OF Cr-SiC COMPOSITES FOR HIGH-TEMPERATURE APPLICATIONS 49

C.E. Maepa, U. Dockrat, T.B. Mashabela, T.B Kadi, M.N. Mirzayev and T.T. Thabethe

POSTERS

PLASMONIC EFFECT OF GOLD NANOPARTICLES ON NaYF4:Er,Yb UP-CONVERTING PHOSPHOR 50

T.M. Abdalkreem, H.C. Swart and R.E. Kroon

SYNERGISTIC ENHANCEMENT OF CO2-EPOXIDE CYCLOADDITION: A STABLE Ti3C2TX@ML-ZIF 9 (MXENE @ MOF) COMPOSITE CATALYST 51

Y.W. Abraha, D.E. Motaung, E.H.G. Langner and H.C. Swart

MICROWAVE-SYNTHESIZED Zn2SnO4 NANOSTRUCTURES: EXPLORING THE EFFECT OF ANNEALING ON MORPHOLOGICAL AND STRUCTURAL PROPERTIES 52

G.M. Choeu, H.C. Swart and K. Shingange

TEM AND XRD INVESTIGATION INTO THE STABILITY OF STRONTIUM-DOPED CSPBI3 PREPARED UNDER ATMOSPHERIC CONDITIONS. 53

M.M. Duvenhage, M.Y.A. Yagoub, E. Lee, H.C. Swart and E. Coetsee

PHASE TRANSFORMATION FROM α-Bi2O3 TO β-Bi2O3 FOR ENHANCED PHOTOCATALYTIC DEGRADATION OF RHODAMINE B 54

J. Divya, N.J. Shivaramu and H.C. Swart

THICKNESS DETERMINATION OF AlxGa1-xAs EPILAYERS BY INFRARED SPECTROSCOPY AND SEM 55

J.A.A. Engelbrecht, M.E. Lee, J.R. Botha, S. Ngongo and E.G. Minnaar

THE SURFACE PROPERTIES OF PULSED LASER-DEPOSITED Y2O3:Ho3+, Yb3+ THIN FILMS 56

V. Makumbane, M.Y.A. Yagoub, R.E. Kroon and H.C. Swart

THE MORPHOLOGY AND TEMPERATURE-DEPENDENT LUMINESCENCE OF Ca4(PO4)2O CODOPED Ce3+ AND Eu2+ PHOSPHORS 57

K.B. Morebodi, S.N. Ogugua and H.C. Swart

CHARACTERISATION OF TiZrN IRRADIATED WITH HELIUM AND SWIFT HEAVY IONS 58

L.Z. Mrwetyana, A. Janse van Vuuren and S. Ngongo

EFFECT OF ANNEALING TEMPERATURE ON BARIUM ZIRCONATE (BaZrO3) PEROVSKITES NANOPARTICLES PREPARED BY SOL-GEL METHOD 59

Q. Nkomo, K.G. Tshabalala, H.C. Swart and S.J. Motloung

STRUCTURAL CORRELATION TOWARDS HIGH-SENSITIVE SENSOR BASED ON In2O3-Co3O4 INTEGRATED WITH N-TYPE-SMOs FOR ACETONE DETECTION 60

K.L. Morulane, Z.P. Tshabalala, H.C. Swart and D.E. Motaung

INFLUENCE OF SYNTHESIS METHOD ON MICROSTRUCTURE AND LUMINESCENCE OF La2Zr2O7:Bi,Tb PYROCHLORE PHOSPHORS 61

B.V. Naveen Kumar and R.E. Kroon

ZEOLITE-ENCAPSULATED SINGLE Pt ATOMS FOR HYDROCRACKING 62

T. Ntlebi and P.J. Kooyman

CHARACTERISATION OF Ti-6Ta-1.5Zr-0.2Ru-5Cu PRINTED BY LASER POWDER BED FUSION 63

N.S. Phala, C. Polese, J. Ciftci, T. Choma and L.A. Cornish

EVOLUTION OF MICROSTRUCTURE AND UPCONVERSION LUMINESCENCE OF Tm,Yb-DOPED YF3 DURING ANNEALING TO FORM Y2O3 64

P.J. Radebe and R.E. Kroon

INSIGHTS INTO THE MORPHOLOGY-PERFORMANCE RELATIONSHIP TOWARDS LPG SENSITIVITY OF Co3O4/rGO GAS SENSORS LOADED WITH SILVER NANOPARTICLES 65

B.C. Tladi, Z.P. Tshabalala, R.E. Kroon, H.C. Swart and D.E. Motaung

PREPARATION OF SrVO3 THIN FILMS USING SPIN COATING 66

E. Lee, R.A. Harris, J.J. Terblans and H.C. Swart

PHASE EVOLUTION AND SURFACE MORPHOLOGY IN COPPER-INDIUM THIN FILMS: STABILITY OF CO-EVAPORATED FILMS 67

L.E. Makoloane, J.J. Terblans, S. Cronje and H.C. Swart

THE STRUCTURAL AND MORPHOLOGICAL STUDY OF MASK-ASSISTED DEPOSITION OF ZnO/Au MICRO-TOWERS 68

D.T. Mashilo, R.A. Harris and H.C. Swart

STUDIES ON THERMAL PROPERTIES OF SPARK PLASMA SINTERED Ti-48Al-2Cr-2Nb ALLOY 69

M.R. Mphahlele, E. Olevsky and P.A. Olubambi

SYNTHESIS AND CHARACTERISATION OF ZIRCONIUM SILICIDE LAYERS ON ZIRCONIUM ALLOY FOR NUCLEAR REACTOR APPLICATION 70

S. Ngongo, A. Janse van Vuuren and J.H. Neethling

ALLOYING INTERMETALLIC AuIn2 AND AuGa2 WITH VARIOUS MACRO AND MICRO ALLOYING ELEMENTS 71

A. Hefer and LA. Cornish

STEM-DPC imaging of what is in between the atomic nuclei

Jörg K.N. Lindner

Nanopatterning, Nanoanalysis & Photonic Materials Group, Department of Physics, Paderborn University, 33098 Paderborn, Germany

The advent of correctors for electron optical lenses has revolutionized the resolution of scanning transmission electron microscopes (STEM) and the development of new detectors/cameras together with advanced computing power enables the collection of an unprecedented wealth of quantitative information about materials. Atomic resolution as high as < 20 pm and the determination of atomic positions with an accuracy in the range of 1 pm has recently been demonstrated[1]. Aberration correction is also beneficial to achieve sub-atomic resolution at reduced electron beam acceleration voltages, important to investigate beam-sensitive materials, such as e.g. 2D materials. The question arises, if we can also "look" in between the atoms, i.e. if we can quantitatively study the electron charge density distribution in materials.

At limited spatial resolution, macroscopic electric and magnetic fields have been frequently analysed in the past using either off-axis electron holography or differential phase contrast (DPC) scanning transmission electron microscopy, a variant of momentum-resolved or 4D-STEM[2]. Much effort has been invested to combine STEM-DPC with the high resolution of aberration-corrected microscopes in order to visualize Coulomb fields in materials at sub-atomic resolution, because from this the projected charge distribution can be calculated using Maxwell's equations. It turns out that STEM-DPC like all other (S)TEM techniques work best for extremely thin samples[3], making monolayers or few-layer stacks of (beam-sensitive) van-der-Waals materials good candidates for the exploration of these new techniques.

In this presentation, an overview of STEM-DPC and 4D-STEM investigations on 2D-materials will be given. A special focus will be placed on experimental and theoretical DPC investigations of the 2D transition metal dichalcogenide WSe_2[4] (Figure 1). It will be demonstrated that even in a film as thin as a single molecule, dynamical diffraction effects need to be taken into account for achieving reliable charge density maps. The application of STEM-DPC to detect the charge state of point defects in 2D-WSe_2 and the substitutional decoration of point defect clusters with impurities will be discussed.

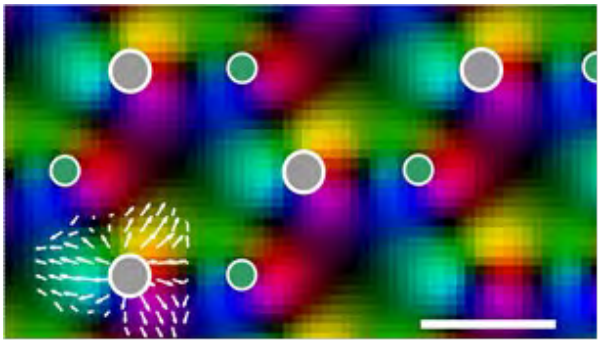

Figure 1. DPC-STEM image of the interatomic electric field distribution in a pristine WSe_2 monolayer with the W and Se atomic positions marked in grey and in green, respectively. Colours represent the direction and strength of electric fields, partially also indicated by vectors. The scale bar is 2 Å.

Corresponding author: *lindner@physik.upb.de*

References
1. Chen Z. et al. (2021) Science 372, 826.
2. Winkler, F. et al. (2020) Ultramicroscopy 210, 112926.
3. Bürger, J., Riedl, T., Lindner, J.K.N. (2020) Ultramicroscopy 219, 113118.
4. Groll, M., et al. (2024) Small 20, 2311635.

Microscopy meanders: highways and backroads to high-resolution imaging in life sciences

L. Joubert

Cryo-EM and Bioimaging Division, Stanford SLAC, Sand Hill Rd, Menlo Park, 94025 CA, USA

The dawn of the new millennium witnessed a period of profound microscopy technology development - now referred to as the 'resolution revolution' [1], which resulted in Nobel prizes in both cryo-Electron Microscopy (cryo-EM) and super-resolution microscopy. The information retrieved from visualizing molecular structures in their native hydrated state in Single Particle Analysis (SPA) cryo-EM has now reached atomic resolution [2]. To visualize macromolecules at increased resolution *in situ* in the context of the cell, cryo-Electron Tomography (cryo-ET; Figure 1) is widely regarded as the new frontier in bioimaging. Additionally, in both cryo-EM and conventional electron microscopy, volume EM (v-EM) and correlative imaging modalities bring enhanced understanding of structures and their function in a three-dimensional environment [3]. Multiscale Bioimaging (Figure 2) has now risen to the forefront in addressing grand challenges in human and planetary health and sustainability.

Aspects that contributed to this rapid growth in microscopy include direct electron detectors, enhanced optics design, increased data storage and computational software development. Currently novel machine learning 'AI' algorithms are developed to aid and accelerate the identification and segmentation of cellular components within cellular volumes. Automation of instrumentation and workflows for sample preparation and data collection is additionally undergoing rapid changes.

For an increased understanding of the function of molecular complexes in metabolically active cells, correlation with a variety of imaging modalities is often applied in sequence during sample preparation and imaging – or also fully integrated into EM instrumentation [4]. Advanced fluorescence microscopy techniques using fluorescent dyes or genetically encoded fluorescent proteins is pivotal to our understanding of cellular processes, and *in situ* fluorescence microscopy in cryogenic Focused Ion Beam-Scanning Electron Microscopy (cryoFIB-SEM) (e.g.) allows for targeted FIB-milling and cryo-ET data collection. Correlation with EDS (energy dispersive X-ray spectroscopy), EELS (electron energy loss spectroscopy) and hard and soft X-ray tomography enhance our understanding of the elemental composition of healthy and diseased cells.

The 'highway' path to apply advanced and high-resolution instrumentation to our research questions have globally become more accessible due to government and privately funded initiatives, and bioimaging consortia and societies that provide not only a path to access, but also directions for training and collaboration using cutting edge technologies. Additionally, alternative paths are increasingly provided by frugal and faster technologies, which also aims at democratizing science and supporting research in the global scientific community [5,6]. The variety of roads that lead to successful scientific endeavors may involve crossing continents and oceans in establishing collaboration and new research paths – not unlike the life of celebrated scientist Boris Ivan Balinsky in whose honor I am presenting this lecture to the Microscopy Society of Southern Africa.

Acknowledgements:

Some of this work was performed at the Stanford-SLAC CryoET Specimen Preparation Center (SCSC), which is supported by the National Institutes of Health Common Fund's Transformative High Resolution Cryoelectron Microscopy program (U24GM139166), and the Stanford-SLAC Cryo-EM Center (S^2C^2), which is supported by the National Institute of General Medical Sciences (1R24GM154186).

References:

1. Kuhlbrandt, W. (2013) Science, 343, 1443
2. Yip, K.M. et al. (2020) Nature, 587, 157
3. Collinson, L.M. et al. (2023) Nature Methods, 20, 777
4. McCafferty, C.L. et al. (2024) Cell, 187(3), 563
5. Callaway, E. (2023) Nature News 17 April
6. Chua, E.Y.D. et al. (2022) Annu Rev Biochem, 21:91,1

Corresponding author: lydiaj@stanford.edu

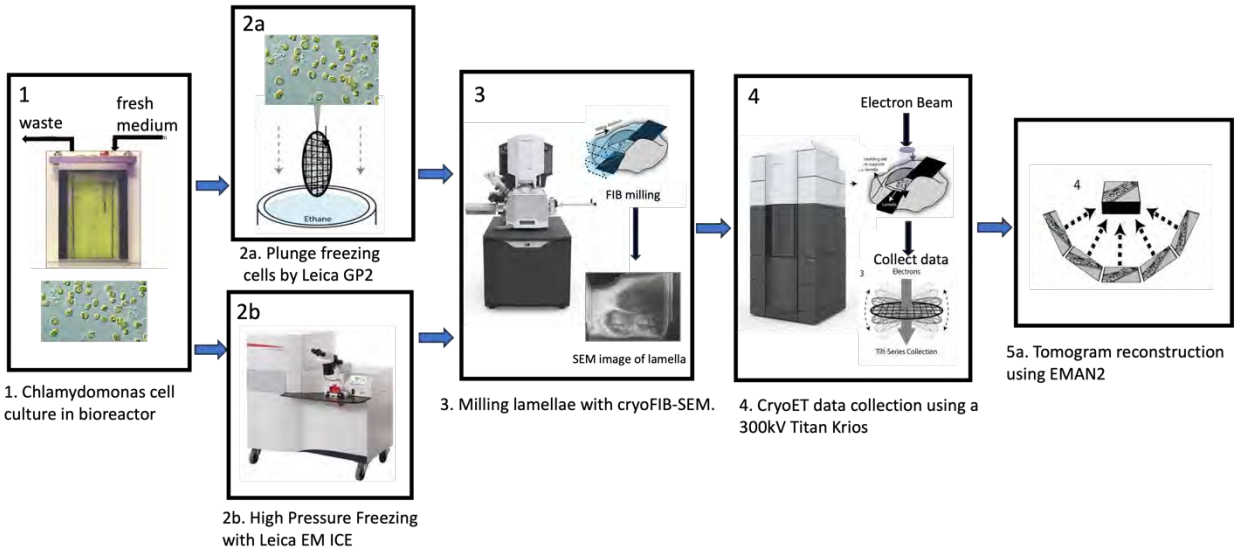

Figure 1: Schematic of workflow for cryo-ET data collection. Cells cultured in bioreactors (1) are either plunge frozen (2a) or high pressure frozen (2b,) followed by cryo-FIB milling of lamellae with a cryoFIB-SEM (3), after which cryo-TEM images are collected as tilt series (4) which are finally reconstructed into 3D tomograms (5).

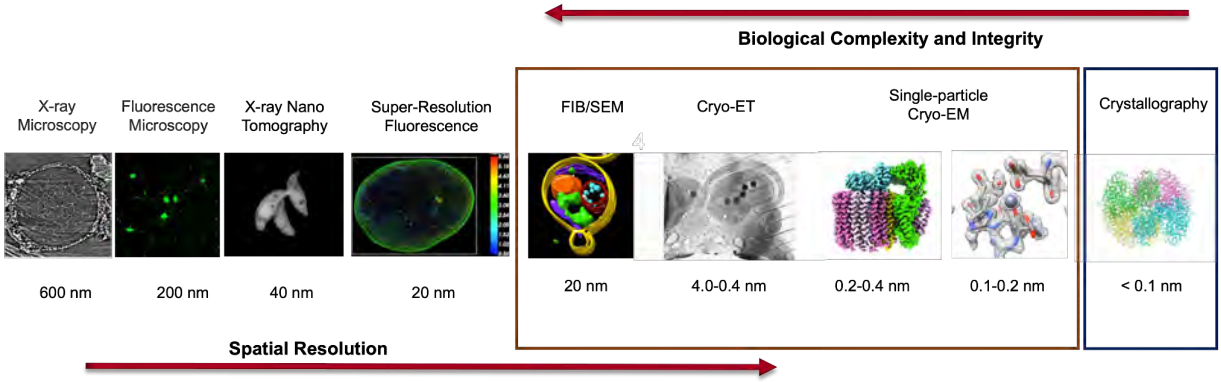

Figure 2: Different imaging modalities of structure determination of biological samples with varying complexities and resolutions.

AUTOPHAGY AND MITOCHONDRIAL QUALITY CONTROL ARE KEY PARAMETERS IN THE CELLULAR PATHOLOGY OF ALZHEIMER'S DISEASE

B. Loos

Department of Physiological Sciences, Stellenbosch University, 7600, Stellenbosch, South Africa

Neurodegenerative diseases, such as Alzheimer's disease are characterized by rapid cognitive decline and memory loss and pose a significant health burden. Currently, no disease modifying treatment exists, creating a major need to accelerate drug discovery. Molecularly, Alzheimer's disease is characterized by lysosomal and mitochondrial dysfunction as well as loss in proteostasis and autophagy, leading to the accumulation of aggregate prone proteins[1]. However, the nature of autophagy decline and mitochondrial dysfunction is poorly understood. Moreover, the relationship between proteotoxic cargo, their targeting to the autophagy machinery and the removal of dysfunctional mitochondria is only recently emerging[2].

Here, we aimed to establish firstly, whether proteotoxic cargo, including amyloid precursor protein, is targeted for degradation, secondly, whether autophagy induction can contribute to enhanced protein clearance and thirdly, whether mitochondria quality control can be quantified more sensitively through fission and fusion analysis, using a single cell model system. Mouse neuroblastoma N2a cells stably expressing the inducible human APP Swedish mutation (N2aSwe), under the transcriptional control of a butyrate-inducible cytomegalovirus promoter or GT1-7 murine neuronal cells were cultured under standard conditions and treated for 12, 24, and 48 h with butyric acid. Images were acquired using a LSM780 ELYRA PS1 confocal/super-resolution microscope platform (Carl Zeiss, Germany) using a 100x oil immersion objective lens. Image processing was performed using the ZEN 2011 imaging software v.2.3 (Carl Zeiss, Germany) or a Python pipeline for thresholding.

Our results reveal that amyloid precursor protein is indeed recruited to the autophagosome and delivered to the lysosome for degradation, with autophagy activity increasing upon APP overexpression. Moreover, neuronal autophagy remains functional even into the onset of apoptosis induction. Autophagy enhancement using spermidine, enhances also autophagosome volume, suggesting increased capacity for cargo removal. Upon memantine exposure, neurons respond with robust mitophagy induction, a decreased fusion (Fig.1) and fission (Fig.2) frequency with a respective mitochondrial phenotype, while enhancing mitochondrial removal and quality control.

These results provide critical evidence that indeed both, the autophagy machinery and mitochondrial quality control systems are strong candidates for drug targeting, with the potential to decrease neurotoxicity and the onset of neuronal cell death in both early and severe pathology of neurodegeneration. Moreover, these targets refelect the molecular dysfunction present in Alzheimer's disease, hence provide greater precision for alleviating neuronal pathology.

References:
1. Nixon, R. and Yang, D. (2011) Neurobiol.Disc. 43(1), 38.
2. Ntsapi, C. *et al.* (2018) Int. Rev. Cell. Mol. Biol. 336(1), 321.

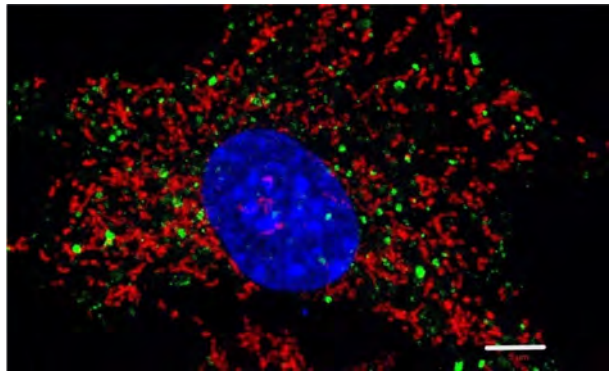

Figure 1. Figure 1. Fluorescence micrograph indicating robust mitochondrial fission, using TMRE, GFP-LC3 and Hoechst 33342 nuclear counterstain. Scale bar: 5 µm

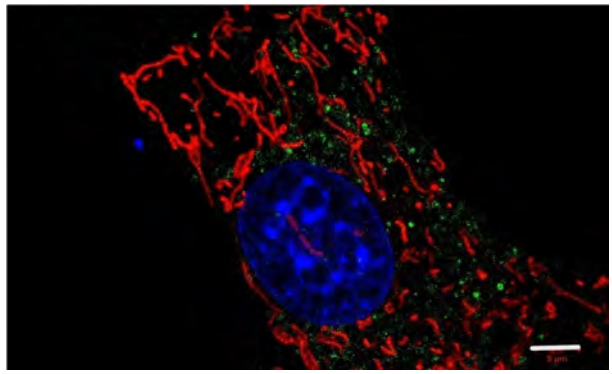

Figure 2. Figure 2. Fluorescence micrograph indicating major mitochondrial fusion, using TMRE, GFP-LC3 and Hoechst 33342 nuclear counterstain. Scale bar: 5 µm

Corresponding author: bloos@sun.ac.za

MODELING SCHIZOPHRENIA ENDOPHENOTYPES IN *Drosophila melanogaster*: EFFECTS OF KETAMINE ON NEUROINFLAMMATORY AND NEURODEGENERATIVE RESPONSES

A.A. Bello and R.O. Folarin

Group for Biopsychiatry Research and Innovative Neuroscience (G-BRaIN), Department of Anatomy, Olabisi Onabanjo, University, Sagamu, Nigeria

Schizophrenia presents a significant challenge in mental health, characterized by a profound distortion of reality, often accompanied by hallucinations, delusions, cognitive deficits, and neuroinflammatory processes. Ketamine, an NMDA receptor antagonist, has been widely used as a pharmacological agent to model schizophrenia symptoms in both human and animal studies. However, the potential of ketamine to induce schizophrenia-like phenotypes in *Drosophila melanogaster* remains under-investigated. This study explored the effects of ketamine on neuroinflammatory and neurodegenerative responses in *Drosophila melanogaster*, as a preliminary step toward developing a pharmacological model of schizophrenia in this organism.

Virgin male and female Oregon-R flies were collected post-eclosion and exposed to four different concentrations of ketamine (100, 250, 500, 1000 µg/mL) for one week under standard laboratory conditions (22-25°C, 50-60% humidity). Experimental groups consisted of 10 vials, each containing 10 flies. Immunohistochemistry was employed to detect the expression of key neuroinflammatory markers. TNF-α; a key pro-inflammatory cytokine involved in neurodegenerative processes and GFAP; a marker for astrocyte activation were used. Sections of whole *Drosophila* heads obtained at 5µm using a rotary microtome were incubated with primary antibodies, followed by fluorescently labelled secondary antibodies. Imaging was performed using a Zeiss LSM-700 confocal microscope. The fluorescence intensity was measured using Image J software. Histological analysis was performed using Hematoxylin and Eosin (H&E) staining to visualize the overall brain architecture and evaluate neurodegenerative changes.
The results of the immunohistochemical analysis showed a dose-dependent increase in TNF-α and GFAP mean fluorescence intensity across treatment groups, indicating an upregulation of both TNF and GFAP expressions. These findings suggest a robust pro-inflammatory and astrogliotic response to ketamine administration, supporting the emerging neuroinflammatory endophenotype theory of schizophrenia aetiology. Histopathological analysis further supported these findings, showing clear signs of dose-dependent neurodegeneration across the treatment groups. Ketamine-treated flies exhibited varying degrees of vacuolation and disorganization of neuropil fibres, with more severe degeneration observed at higher doses. These structural changes suggest that ketamine induces neurotoxicity. The neurodegenerative effects of ketamine in *Drosophila* are consistent with those seen in mammalian models, reinforcing the value of this model for studying schizophrenia-related neuroinflammation and neurodegeneration. In conclusion the findings suggest that ketamine has potential in inducing schizophrenia-like endophenotypes and as a model for investigating potential therapeutic interventions.

References:
1. Anticevic, A. *et al.* (2015) Biolog. Psychiatry, 77(6), 569.
2. Bellen, H. J., Tong, C., and Tsuda, H. (2010) Nature Reviews. Neurosci. 11(7), 514.
3. Borsini, A. *et al.*, (2015) Trends in Neurosci. 38(3), 145.

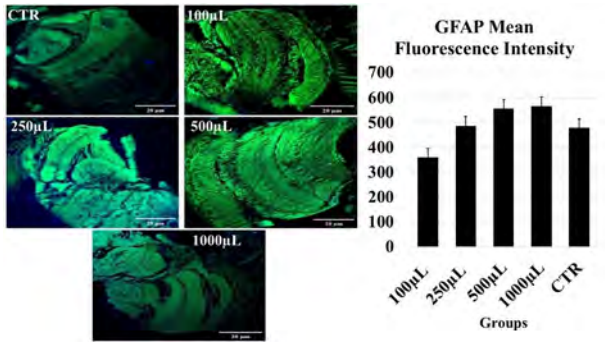

Figure 1. Section of *Drosophila* brain showing the distribution and localization of GFAP.

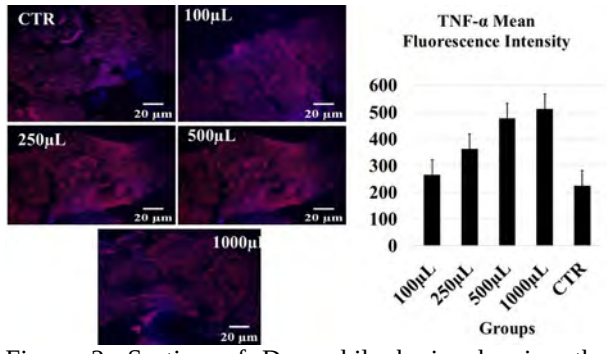

Figure 2. Section of Drosophila brain showing the distribution and localization of TNF-α.*Drosophila* brain showing the distribution and localization of TNF-α.

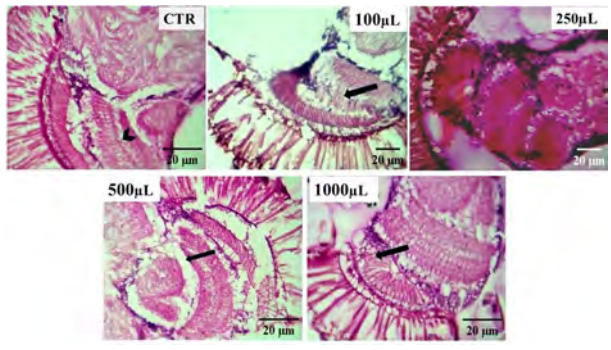

Figure 3. Section of *Drosophila* head showing the brain stained using H and E stain.

Corresponding author:
royhaan.folarin@oouagoiwoye.edu.ng

Nigella sativa OIL MITIGATES THALAMIC AND SUBICULAR DYSFUNCTION IN PENTYLENETETRAZOLE-INDUCED EPILEPTOGENESIS IN BALB/C MICE

B.M. David[1,2] and R.O. Folarin[1]

[1]Department of Anatomy, Olabisi Onabanjo University, Ogun State, Nigeria., [2]Department of Anatomy, Babcock University, Ogun State, Nigeria.

Epileptogenesis is the transformation of a normal functioning brain network into a hyper-excitable and hyper-synchrony neural network in which recurrent, spontaneous seizures occur. This can result in development of epileptic condition It poses a significant global health challenge, affecting over 50 million people worldwide.[1] Despite significant progress in understanding how epilepsy develops, a treatment devoid of side effects that can prevent the development or worsening of epilepsy in at-risk patients remains elusive.[2] Hence a shift in research focus to natural compounds that offer anti-epileptic and neuroprotective benefits with minimal or no side effects. *Nigella sativa*, identified as black seed, serves as a potent herb notable for its wide range of health benefits. It is from the Ranunculaceae family, originally found in Southwest Asia. Its seeds and oil, packed with beneficial compounds like thymoquinone and polyphenols, offer a vast array of health benefits.[2,3] This study explored the effects of *N. sativa* oil (NSO) on the thalamus and subiculum brain regions involved in the development and propagation of epilepsy—through their roles in information processing, oscillatory activity, and synaptic plasticity—in pentylenetetrazole (PTZ)-induced BALB/c mouse models of epileptogenesis.

Forty-four male and forty-four female BALB/c mice were randomly allocated into four experimental groups. (1) PTZ only (PTZ), (2) PTZ and NSO concurrently (PTZNS), (3) NSO prior to PTZ (NSPTZ), and (4) NSO before PTZ and NSO concurrently (NSCPTZ). PTZ was administered at 35 mg/kg, and NSO at 12 ml/kg, alternately every 24 hours for 20 days. Seizure dynamics were assessed using the Racine scale, [4, 5] and behavioral manifestations were inspected from videotaped surveillance. Spatial memory and muscular strength were evaluated using object location[6] and grip strength tests,[7] respectively. Histological analysis was performed using Hematoxylin and Eosin (H&E) staining for histoarchitectural integrity, and Cresyl Fast Violet (CFV) staining to quantify Nissl substance. The photomicrographs were analyzed using Image J software and Graphpad Prisms for statistical comparison ($P<0.05$).

NSO treatment significantly mitigated seizures through the reduction of seizure latency, frequency, duration, and intensity. It also enhanced motor function, reduced neuronal damage, and improved cellular integrity, particularly in the NSO-pretreated groups. However, NSO and PTZ did not impact spatial memory. Compared to NSPTZ and NSCPTZ groups, PTZ and PTZNS groups expressed abnormal increase in neuronal nissl positivity indicating neuronal hypertrophy and hyperactive protein synthesis; a compensatory mechanism in response to neuronal stress.

In conclusion, NSO demonstrates neuroprotective properties by reducing the adverse effects of PTZ, suggesting its potential to complement current treatments for epilepsy.

References:
1. Thijs, R. D. *et al.* (2019). Lancet, 393(10172), 689.
2. Pitkänen, A. (2010). Epilepsia, 51, 2.
3. Rohman, A. *et al.* (2019). Food Res. 3 (6): 628.
4. Ilhan, A. *et al.* (2005). Neuropharmacology, 49(4), 456.
5. Aleshin, Vasily A. *et al.* (2023). Int. J. Mol. Sci. 24(15): 12405.
6. Vogel-Ciernia, A. and Wood, M. A. (2014). Curr. Protoc. Neurosci. 69(1), 8-31.
7. Deacon, R. M. (2013). J. Vis. Exp. 76, e2610.

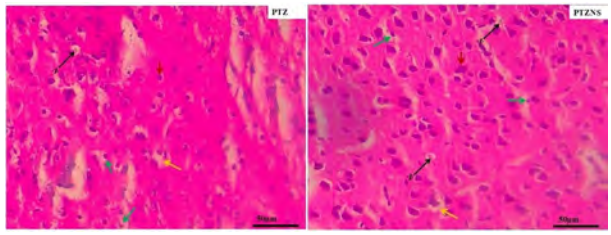

Figure 1. Effect of NSO on PTZ-induced epileptogenesis in the thalamus (x400) Red arrow head indicates viable neurons; green is pyknosis; black arrow (N) indicates necrosis and yellow arrow indicates vacuolation. a) PTZ = PTZ only.

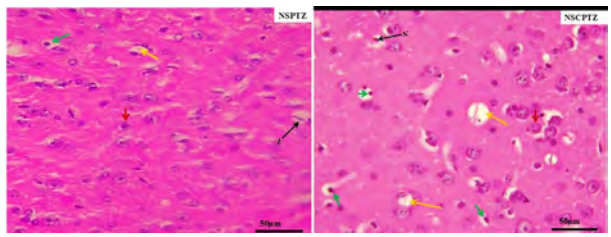

Figure 2. Effect of NSO on PTZ-induced epileptogenesis in the thalamus (x400) Red arrow head indicates viable neurons; green is pyknosis; black arrow (N) indicates necrosis and yellow arrow indicates vacuolation. NSPTZ=NSO before PTZ.

Corresponding author:
royhaan.folarin@oouagoiwoye.edu.ng

PROBING AUTOPHAGY: COMPARING PLASMIDS, TECHNIQUES AND THE QUEST FOR AN AUTOMATED CLEM ALGORITHM

N. Vahrmeijer[1], E. Sharrat[2], J. Conradie[3], L. Engelbrecht[3], R. Theart[4] and B. Loos[1]

[1]Department of Physiological Sciences, [2]Department of Mechanical and Megatronic Engineering, [3]Central Analytical Facilities, [4]Department of Electrical and Electronic Engineering, Stellenbosch University, Stellenbosch

Autophagy, a vital intracellular degradation process of cytosolic proteins and organelles, has fascinated researchers since its discovery through electron microscopy in the 1950's1, owing to its distinctive, double-membraned vesicular structure. Currently, three generations of fluorescent probes are commonly employed to monitor autophagy: GFP-LC32, mRGP-LC3-GFP3 and GFP-LC3-RFP-LC3ΔG4, offering unique advantages but also limitations. Currently, no standardised method for quantitatively assessing autophagy exists, and to assess autophagy activity, with its pathway intermediates (i.e. autophagosomes, autolysosomes and lysosomes) is extremely time-consuming and expertise dependent.

This study therefore had two aims, firstly to compare the three most widely used autophagy probes, and secondly, as a point of departure, to develop an automated image analysis algorithm, AutoPhinder, to allow researchers to assess autophagy in its entirety with ease and limited expertise using, the gold standard, electron micrographs only.

In this study mouse embryonic fibroblasts (MEF) cells were either stably transfected with GFP-LC3 or transiently transfected with either mRFP-GFP-LC3 or GFP-LC3-RFP-LC3ΔG plasmids. To assess autophagy flux under basal and induced conditions, cells were treated with either 400 nM Bafilomycin A1 (Baf) or 25 nM Rapamycin (Rapa) for 2 hours and 4 hours, respectively, fixed with 4% buffered PFA and imaged using a Carl ZEISS Confocal Elyra PSI microscope for confocal and super resolution (SR)-SIM image acquisition. For electron microscopy (EM), cells were fixed using a Megametal staining protocol5 and imaged using either a ThermoFischer Apreo FESEM for 2D image acquisition or a Zeiss Crossbeam 540 Focused Ion Beam SEM (FIB-SEM) for 3D image acquisition for micrographs used to train AutoPhinder. Image analysis for puncta counts was performed using a python-based algorithm (AutoVIPP) whilst Zooniverse (Etch-a-Cell) will be used to train the automated autophagy detection algorithm.

Our results reveal that each autophagy plasmids resulted in differences in autophagy intermediate pool size in terms of fluorescent punctate structures (Fig. 1A) and abundance. We further highlight the importance of indentifying pathway intermediates and conducting pool size analysis (Fig. 1B). Moreover, we highlight the importance of CLEM and its power in allowing successful identification of autophagy intermediates in electron micrographs by bringing together the molecular identity and the ultrastructural context of each organelle respectively (Fig. 1C). Our findings emphasize the variability introduced by differed autophagy probes and imaging techniques, and highlights the need to standardise acquisition and analysis techniques when assessing a highly dynamic process such as autophagy. Additionally, through developing AutoPhinder, we demonstrate the potential for streamlining autophagy analysis through automating identification, quantification and segmentation of pathway intermediates using EM data only, allowing rapid exploration of autophagy with unparalleled ease, providing a powerful toolbox for studying autophagy in health and disease.

References:

1. de Duve C. and Wattiaux R. (1966) Ann. Rev. Physiol. 28, 435. doi: 10.1146/annurev.ph.28.030166.002251
2. Kabeya Y. (2000) EMBO J. 19, 5720. doi: 10.1093/emboj/19.21.5720
3. Kimura S., Noda T. and Yoshimori T. (2007) Autophagy 3,452. doi: 10.4161/auto.4451
4. Kaizuka T. *et al*. (2016) Mol. Cell 64,835. doi: 10.1016/j.molcel.2016.09.037

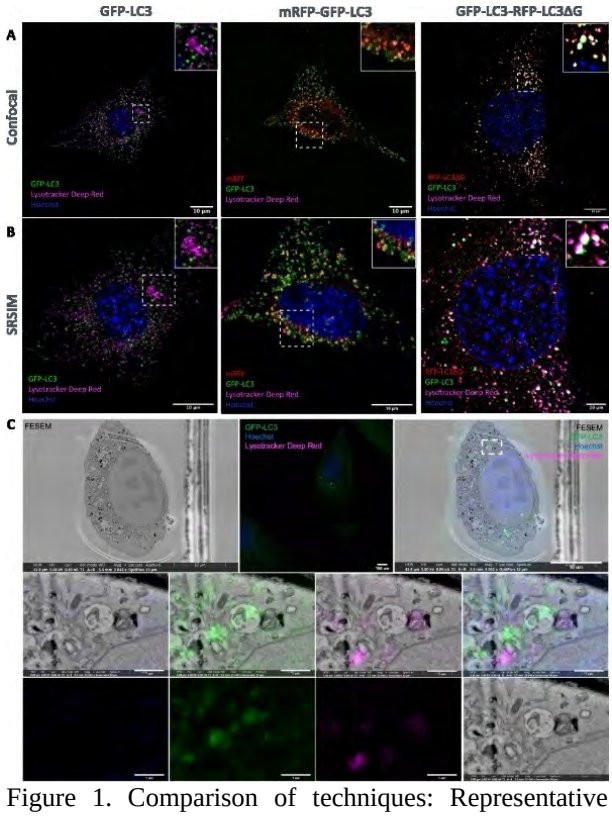

Figure 1. Comparison of techniques: Representative fluorescence micrographs of control groups using (A) Confocal Microscopy, (B) SRSIM and (C) CLEM.

Corresponding author: 20186282@sun.ac.za

A NOVEL METASYSTEMS CLASSIFIER FOR PLATELET FRAGILITY AND MORPHOLOGY ANALYSIS

C. Venter[1], J.H. Pretorius[2], D.B. Kell[1,3,4] and E. Pretorius[1]

[1]Dept. of Physiological Sci., [2]Dept. of Economics, Stellenbosch Univ., SA, [3]Dept. of Biochem. and Systems Biology, Univ. of Liverpool, UK, [4]The Novo Nordisk Foundation Centre for Biosustainability, TU Denmark, Denmark.

Platelets play a crucial role in coagulation and also contribute to pathological clotting. When a blood vessel is damaged, platelets rush to the site of injury and stick to the damaged blood vessel walls, forming a plug to prevent further bleeding. However, platelets can also contribute to the development of inflammatory diseases, as they can become activated and aggregate inappropriately. Such pathological processes can lead to serious events such as heart attacks, stroke, deep vein thrombosis, and pulmonary embolisms[1]. In recent articles published by our group the effects on the coagulation system have been noticed after exposure to COVID-19 and later in Long COVID patients. Changes include platelet hyperactivation and microclot formation in the blood[2,3,4.]

Various techniques are available in a typical haematology laboratory to study platelet numbers, sizes and function. These tests can be used to diagnose platelet disorders, assess antiplatelet therapy effectiveness, and assess bleeding risk in patients. Unlike methods that study platelets in whole blood, buffy coat, or platelet-rich plasma, with stabilizers to prevent activation, our approach involves centrifuging whole blood to create platelet poor plasma. This is followed by analyzing the platelets in the remaining hematocrit fraction, without the addition of platelet stabilizers, providing a more accurate assessment of platelet fragility, with the use of our grading system[2]. With the potential biases in manual microscopy analysis, machine learning software can help eliminate sample bias. Thus, the aim of the study was to develop an automated platelet analysis method using an automated MetaSytems classifier for platelets, to remove any bias of a manual platelet grading system[2], and to test this by using health controls and Long COVID patients.

Human blood was collected from healthy individuals and Long COVID patients (Ethical ref.: N19/03/043, 9521) and centrifuged at 3000xg for 15 minutes. For the fluorescence platelet analysis, CD62P-PE (IM1759U, Beckman Coulter) and PAC-1 FITC (340507, BD Biosciences) were added to the haematocrit for 30 minutes. To visualize the platelets, the excitation wavelength for PAC-1 was set at 450-488nm and the emission at 499-529nm and for the CD62P marker it was set at 540-570nm and the emission 577-607nm. The samples were viewed using a Zeiss Axio Observer 7 fluorescent microscope testing two approaches: a) manually, using the platelet criteria system[2], and b) using the MetaSystems Metafer software (Version 4.3, MetaSystems, Altlußheim, Germany), where we developed a novel MetaCyte Metafer classifier for the platelets. Statistical analysis was done using GraphPad Prism (version 10.3), where the Sapiro-Wilk test was used to assess distribution followed by the non-parametric data analysis and unpaired T-test analysis where necessary. Analysis of deidentified data was done in R-statistical software (version 4.2.2) and Microsoft Excel.

Results showed that the automated method yields accurate, consistent, and unbiased data (not all data shown here), making it accessible to research and pathology labs with minimal training. The study confirmed substantial platelet activation in Long COVID patients compared to healthy controls, aligning with existing literature on altered platelet dynamics in Long COVID[3,4]. Statistical analysis revealed significant differences in platelet size distributions between controls and Long COVID participants (Fig.1). The automated MetaSystems classifier provided detailed metrics such as area, count, and roundness, advancing platelet analysis. This approach may help identify subtle changes in platelet structure and activation based on morphology, contributing to a deeper understanding of platelet pathology in Long COVID and other thrombo-inflammatory conditions.

References:
1. Kell, D.B. and Pretorius, E. (2022) Biochem. J. 479, 1653.
2. Laubscher, G.J. *et al.* (2021) J. Clin. Med. 10(22), 5381.
3. Kruger, A. *et al.* (2022) Cardiovasc Diabetol. 21, 190.
4. Venter, C. *et al.* (2020) Int. J. Mol. Sci. 21. 8234.

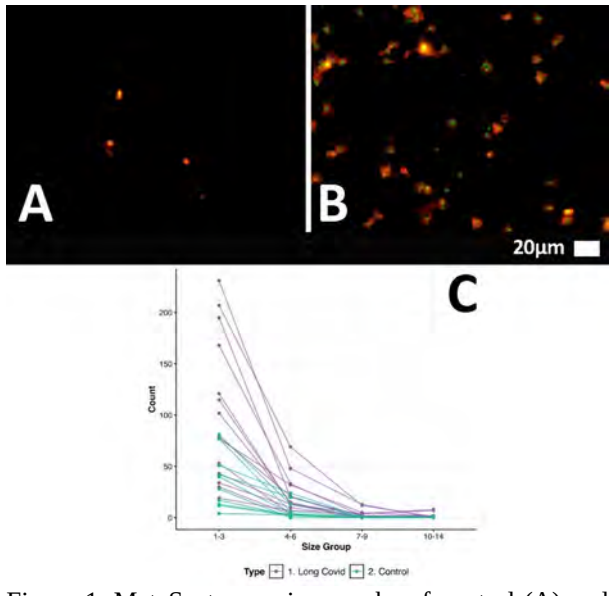

Figure 1. MetaSystems micrographs of control (A) and Long COVID (B) platelets. (C) Parallel coordinate plot of size versus count of platelets for control (green) and Long COVID (purple) samples.

Corresponding author: chantellev@sun.ac.za

THE *EX VIVO* EFFECTS OF *Bitis arietans* AND *Naja mossambica* VENOM ON BLOOD COAGULOPATHY

C. Megaw[1], J. Bester[2] and M.A. Strydom[1]

[1]Department of Pharmacology, [2]Department of Physiology, School of Medicine, Faculty of Health Sciences, University of Pretoria

In 2017, venomous snake bites were recognised and categorised as a category A neglected tropical disease (NTD), by the World Health Organization (WHO), thus allowing for the allocation of funds to allow for increased research in this field. Statistics show that between 1.2 and 5.5 million snakebite incidents occur annually, with between 81 000 and 138 000 fatalities and 400 000 victims suffering from long-term physiological or neurological problems. Given the frequency of *Bitis arietans* and *Naja mossambica* snake bites, research into the venom's effects is essential in developing more efficient treatments. Very little is known about the coagulative changes that *B. arietans* and *N. mossambica* venom induces in humans, other than the cytotoxic properties of *B. arietans* and *N. mossambica* venom.

This study investigated the *ex vivo* effects of *B. arietans* and *N. mossambica* venom on human blood, focusing on platelet activity, ultrastructure, and viscoelastic properties. The objectives were to assess red blood cell (RBC) deformation using light microscopy (LM), examine fibrin fibres, platelets, and RBC ultrastructure using scanning electron microscopy (SEM), and evaluate whole blood clot kinetics with Thromboelastography® (TEG®).

This analytical, laboratory-based study involved healthy volunteers aged 18 to 60 without chronic disorders. Blood samples from participants were exposed *ex vivo* to a final concentration of 2.0 ng/µL of *B. arietans* venom and a final concentration of 0.025 ng/µL of *N. mossambica* venom. SEM, LM and TEG® were employed to assess the venom's impact on RBCs, platelets, fibrin fibres, and clot structure in whole blood. A standard SEM preparation protocol was used with primary fixation (4% formaldehyde solution, from a 36.5-38% stock solution), secondary fixation (1% OsO_4), graded dehydration (for 3 minutes each in 30%, 50%, 70% and 90% ethanol with a three times 3 minute repeat for 100% ethanol) and drying for 30 minutes (HDMS) followed by loosening of the slides and adding a single drop of HDMS, left to dry overnight. For light microscopy slide preparation, methanol (5 minutes) was used to fix the blood smears, and methylene blue (5 minutes) and eosin (1 minute) were used for staining with washing and drying steps in between the fixation and staining steps. For TEG®, 20 µL $CaCl_2$ was added to 340 µL blood in a TEG® cup and the test was run.

This study demonstrates that exposure to snake venom markedly affects the red blood cell (RBC) morphology, platelet activation, and clot structure observed in control samples (Figs 1 A-C). Specifically, *N. mossambica* venom had a pronounced impact on RBC morphology, causing extensive eryptosis and producing denser clots with fibrin fibres that appeared "melted." Microscopic analysis revealed abnormal fibrin networks, signs of eryptosis, and altered RBC morphology (Figs 1 D-F). In contrast, *B. arietans* venom induced clusters of activated platelets in exposed samples, and resulted in smaller, dispersed clots in response to thrombin (Figs 1 G-I). The TEG® results further indicated a prolonged clot initiation time and reduced maximum amplitude in venom-exposed samples compared to controls, suggesting the presence of thrombocytopenia and secondary fibrinolysis.

The findings of the study confirm that *B. arietans* and *N. mossambica* venom interferes with platelet function and affects fibrin clot formation. These insights can improve the understanding of the effect these venoms can have on human coagulation, allowing for the creation of venom profiles for identification in snakebite victims.

References:
1. Williams, D.J. *et al.* (2019) PLos ONE 13(2), e0007059.
2. Marais, J. [Internet]. (2021) Puff adder. African Snakebite Institute; [cited 2023 Feb 7]. Available from: https://www.africansnakebiteinstitute.com/snake/puff-adder/.
3. Tilbury, C.R. (1982) S. Afr. Med. J. 61, 308.

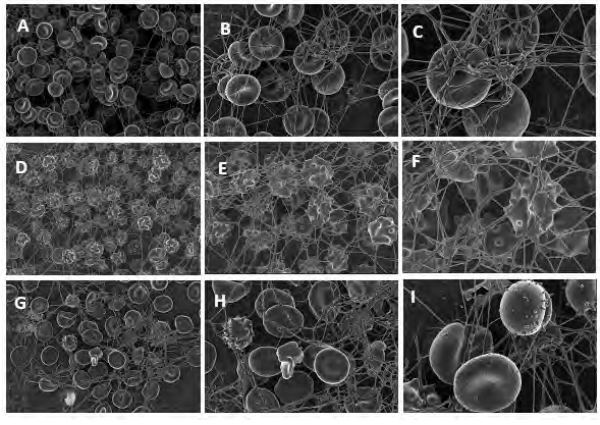

Figure 1. A-C, Control sample containing thrombin, showing normal cell morphology and fibrin network before treatment.
D-F, Whole blood sample exposed to *Naja mossambica* venom and thrombin. Abnormally shaped red blood cells and fibrin fibres can be observed.
G-I, Whole blood sample exposed to *Bitis arietans* venom and thrombin. Some abnormally shaped red blood cells, sparser clot formation and abnormally thin fibrin fibres can be observed.

Corresponding author: u18127577@tuks.co.za

MORPHOLOGICAL CHANGES INDUCED BY THE IMIDACLOPRID, USING A RAT LEYDIG CELL LINE (LC-540)

M.I.A. Ibrahim, G.C.H. Ferreira, E.A. Venter and C.J. Botha

Dept. of Paraclinical Sciences, Faculty of Veterinary Science, University of Pretoria, Onderstepoort, South Africa

Imidacloprid is a systemic neonicotinoid insecticide widely used to combat agricultural pests and flea infestations in dogs and cats [1]. Despite its low toxicity to mammals, imidacloprid is reported to cause male reproductive toxicity [2]. The objectives of this study were to evaluate changes in certain cytoskeletal proteins and assess ultrastructural changes in the rat Leydig tumour cell line (LC-540) exposed to imidacloprid.

A Fischer rat testis Leydig tumor cell line (LC-540, JCRB9064) was used in this study. Cells were seeded in EMEM medium supplemented with 5% fetal bovine serum in tissue culture microplates providing optimum growth area and ease of processing of the cells as required by the different cell assays used in this study. After exposing the Leydig cells to various concentrations of imidacloprid (75–800 µM) for 24, 48, and 72 h, cytotoxicity was evaluated using cell viability assays. Subsequently, the effects of exposure to 300, 400, and 500 µM imidacloprid for 72 on cytoskeletal proteins (ß-tubulin-C4585 and F-actin-P5282), mitochondrial morphology (MitoTracker® Orange CMTMRos-M7510), lysosomal acidity (LysoSensor™ Green DND-189), and ultrastructure was investigated. Images were captured with confocal microscopy (Zeiss LSM-880), and transmission electron microscopy (JEOL JEM 1400-FLASH). Fiji-ImageJ software [3] with plugins for diffraction PSF 3D and iterative deconvolution 3D [4] were used to process the images.

The results of this study indicated that cell viability was markedly reduced after 48 and 72 h of exposure to imidacloprid concentrations of more than 600 and 300 µM, respectively. Furthermore, immunofluorescence analysis revealed that there was a disruption and disorganization of F-actin microfilaments, and microtubules in Leydig cells following exposure to 400 and 500 µM imidacloprid for 72 h (Fig. 1). Ultrastructurally, cytoplasmic vacuoles, autophagic vacuoles, lysosomes, and mitochondrial damage were detected in cells treated with 300, 400, and 500 µM imidacloprid, while autophagic vacuoles were only observed at 400 and 500 µM imidacloprid (Fig. 2). Additionally, changes in the mitochondrial morphology and lysosomes induced by imidacloprid were confirmed. Cytoskeletal proteins play numerous functions in general cellular processes and are also involved in Leydig cell steroidogenic processes [5]. Mitochondria are essential in cellular metabolism, and the response to stresses [6], and they play a major role in testosterone biosynthesis [7]. Therefore, the results of this study suggest that the reduction in the viability of LC-540 cells could be due to the changes in mitochondrial morphology and cytoskeletal proteins disruption induced by imidacloprid. Thus, it is possible to speculate that imidacloprid might cause male infertility.

The Microscopy and Microanalysis Laboratory, University of Pretoria is acknowledged.

References:
1. Tomizawa, M. and Casida, J.E. (2005) Annu. Rev. Pharmacol. Toxicol., 45**,** 247.
2. Bal, R *et al.* (2012) Cell Biochem. Funct., 30 (6)**,** 492.
3. Schindelin, J. *et al.* (2012) Nat. Methods, 9 (7)**,** 676.
4. Dougherty, R. (2005) 11th AIAA/CEAS aeroacoustics conference, 2961.
5. Sewer, M. B. and Li, D. (2008) Lipids, 43**,** 1109.
6. Vakifahmetoglu-Norberg, H., Ouchida, A. T. and Norberg, E. (2017) Biochem. Biophys. Res. Commun., 482 (3)**,** 426.
7. Zirkin, B. R. and Papadopoulos, V. (2018) Biol. Reprod., 99 (1)**,** 101.

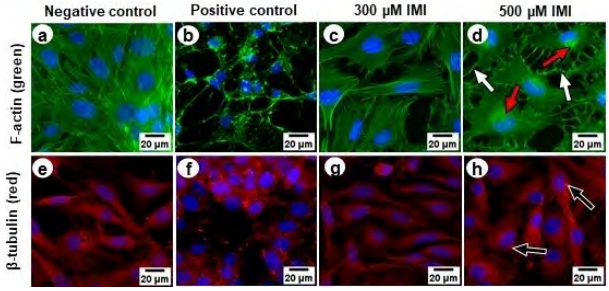

Figure 1. Fluorescence labelling of F-actin (green, a-d) and β-tubulin (red, e-h). Negative controls (media only). Positive controls Cytochalasin-D (b) and Vinblastine sulphate (f). White arrows: Aggregation and of F-actin filaments and microtubules (arrows). Counterstain DAPI (blue).

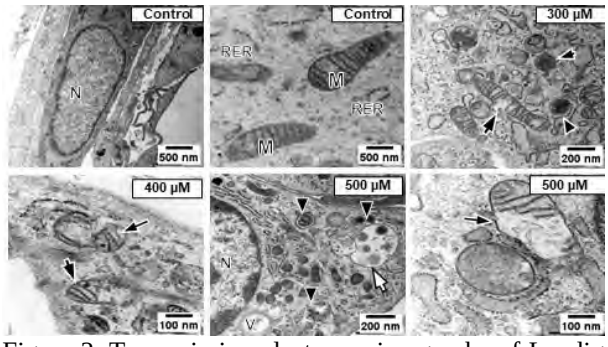

Figure 2. Transmission electron micrographs of Leydig cells. Damaged mitochondria (black arrows) and lysosomes (black arrowheads). White arrows indicate distinct autophagic vacuoles with mitochondria and cellular debris. M, Mitochondria; N, Nucleus; RER, Rough Endoplasmic Reticulum; V, Vacuole.

Corresponding author: wadibrahim352@gmail.com

IMMUNOHISTOCHEMISTRY EVALUATION OF SATELLITE CELL ACTIVATION STATUS IN EXERCISED AND CONTRALATERAL UNEXERCISED MUSCLE

M.L. Cowley and K.H. Myburgh

Department of Physiological Sciences, Stellenbosch University, Stellenbosch

Satellite cell (SC) activation is central in skeletal muscle repair and remodelling following exercise-induced damage. SC activation is observed 24 hours after an acute bout of damaging eccentric exercise in the exercised muscle1, as well as increased strength in the contralateral unexercised muscle2. This suggests a contralateral protective adaptation. This study investigates how SC dynamics are influenced in both the exercised and contralateral unexercised muscle post-exercise, considering different exercise test modes and volumes.

Thirty-two recreationally active males (21 ± 2 yrs) were randomly allocated into four exercise groups. Experimental groups consisted of either 100 or 300 eccentric contractions on an isokinetic dynamometer (resistance applied on Biodex), or 100 or 300 unilateral split squat jumps (4x n=8). Skeletal muscle biopsies from the *vastus lateralis* were collected 7 days before exercise and 24 hours post-exercise and frozen in liquid nitrogen embedded with the optimal cutting temperature (OCT) method. After cryosectioning (-30 degrees centigrade) the tissue samples in the cross-sectional orientation at a thickness of 8 um, SC were identified using fluorescence staining with a Pax7 primary mouse antibody with activation assessed using a Delta-like factor 1 (DLK1) primary rabbit antibody. After staining with secondary antibodies, fluorescent images (Fig. 1A) were obtained with a confocal microscope using the 20x objective and 2x3 tile scan. The number of SCs that were Pax7+ and activated (Pax7+/DLK1+) was determined using available software.

In general, DLK1 labelling results showed a significant increase in activated SCs 24 hours post-exercise. With resistance exercise the number of activated SCs in the exercised leg increased significantly and similarly for both repeat volumes (100 repetitions – 0.05±0.004; 300 repetitions – 0.05±0.006) compared to baseline (100 repetitions – 0.015±0.004; 300 repetitions – 0.014±0.004). In the unexercised leg, the activated SC number was lower but still significantly elevated over the baseline (100 repetitions - 0.039±0.004; 300 repetitions – 0.035±0.004). With unilateral jumping exercise the increase in the number of activated SCs in the exercised leg was also significant (100 repetitions – 0.03±0.004; 300 repetitions – 0.05±0.005) compared to baseline (100 repetitions – 0.015±0.003; 300 repetitions – 0.012±0.006) and slightly lower in the unexercised leg (100 repetitions - 0.023±0.003; 300 repetitions – 0.037±0.006). Here it was interesting to note that increased exercise repeats resulted in a significant difference in activated SC numbers in both the exercised and unexercised leg ($p<0.05$).

In summary, Pax7/DLK1 immunohistochemical co-staining and subsequent quantitative analysis successfully indicated SC activation status was changed by exercise intervention. For the first time, we show that SCs in both the exercised and contralateral unexercised leg react to a single bout of training. In resistance training SC activation in either leg was not dependent on exercise volume, whereas the number of jumps did influence SC activation status. This suggests that the focus during injury rehabilitation should include strengthening the contralateral uninjured muscles. The exercise type and repeats should also be carefully considered.

References:
1. Cermak, N.M. *et al.* (2013) Medicine & Science in Sports and Exercise. 45(2), 230.
2. Chen, H.L. *et al.* (2018) Medicine & Science in Sports & Exercise. 50(3), 542.

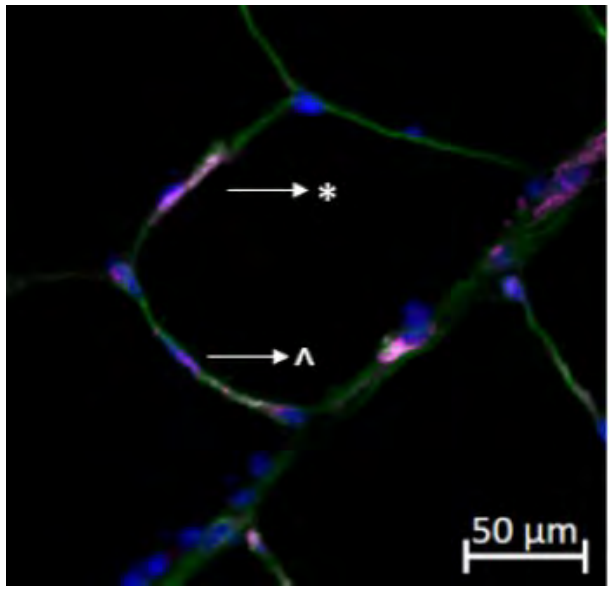

Figure 1. Cross-sectional view of a human muscle biopsy sample indicating a satellite cell (^) and an activated (*) satellite cell. Scale bar 50um.

Corresponding author: khm@sun.ac.za

INCREASING THE THERMOSTABILITY OF A CYANIDE-CONVERTING NITRILASE

B.T. Sewell[1], L.S. Dlamini[1], J.D. Woodward[2], A.E. Mulelu[1], J. Reitz[3] and A. Frangakis[3]

[1]Department of IBMS, UCT, [2]Electron Microscope Unit. UCT, [3]IMLS, Goethe University Frankfurt, Germany

Cyanide detoxification is a significant problem in mining and electroplating industries. Enzymatic conversion of the cyanide to formic acid and ammonia offers the potential for on-site detoxification. To achieve this goal the thermostability of naturally occurring cyanide-converting enzymes must be substantially enhanced.

We have determined the structures of the nitrilase from *Bacillus pumilus* isolated from cyanide-containing mining wastewater and a thermostable variant produced by random mutagenesis (Q86R). These structures were used to predict mutations that would further enhance thermostability using the computer program FoldX[1]. The structure of a predicted thermostable variant (E155R) was determined by cryo-EM using a Titan Krios II Electron Microscope and single particle reconstruction with CryoSPARC[2]. An atomic model was built and refined with Phenix[3] and finally fitted by molecular dynamics flexible fitting with Isolde[4], a plug-in to ChimeraX[5].

Nitrilases are hollow-cored helical structures made up of a repeating asymmetric unit comprising four monomers, each having approximately 330 amino acids (depending on species). The asymmetric unit, in which the monomers associate across two surfaces (designated A and C), has a two-fold axis that is perpendicular to the helix axis (Fig 1). The C-terminal regions of the monomers associate on the inside of the helix, forming a beta-sheet that lines the hollow core. The formation of the helices, and hence the A and C interfaces, occurs in all known nitrilases and is essential for activity. Successive gyres of the helix are separated by a groove across which only one interaction (Q86 with the symmetry-related, opposing Q86) occurs in the wild-type enzyme. Substituting this residue with an arginine results in an interesting modification in which the R86 forms an ionic bridge between opposing glutamates (E90). The predicted E155R variant is even more interesting. R155 interacts with either of E96 or N121 of the subunit on the other side of the groove. In doing so, it alters the helical twist, thus relocating Q86 so that it now hydrogen bonds to the side chain of Q320 in the C-terminal "tail" of a neighboring subunit.

Thermostability is conferred by the introduction of hydrogen bonding and ionic interactions that stabilize the helical structure. Such interactions, on the surface of the monomers, lead to an elongation of the helical structure in such a way that observed fibre length correlates well with thermostability as measured by DDG.

References:
1. Saposhnikov, Y. *et al*. (2023) BMC Bioinformatics 24, 426.
2. Punjani, A. *et al.* (2017) Nature Methods 14(3), 290.
3. Afonine, P.V. *et al*. (2018) Acta Cryst. Section D: Structural Biology 74(6), 531.
4. Croll, T.I. (2018) Acta Cryst. Section D: Structural Biology 74(6), 519.
5. Pettersen, E.F. *et al.* (2021) Protein Science 30(1), 70.

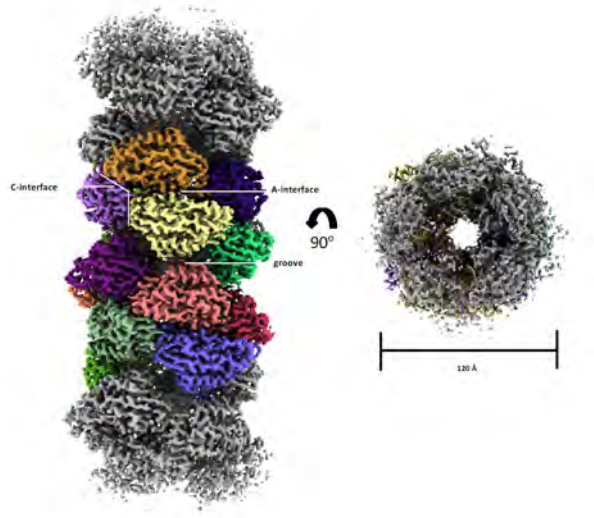

Figure 1. Surface representation of a 3.15 Å resolution charge density map of a reconstruction of the nitrilase from *Bacillus pumilus* ($CynD_{pum}$) variant (Q86R/H232K/H305K/H323K). Map deposited as EMD-16437. Atomic co-ordinates deposited as PDB - 8c5i.

Corresponding author: trevor.sewel@uct.ac.za

AN AGE-OLD MYSTERY: THE SPIKE ON THE LION'S (*Panthera leo*) TAIL

J.R. Dirsuwei, M.R. Crole and S.J. Clift

Department of Anatomy and Physiology, Faculty of Veterinary Science, University of Pretoria, Onderstepoort, South Africa, 0110.

A unique feature of the lion's tail is the tuft of long dark hairs. Within this tuft is a claw-like structure at the most distal extremity[1]. The functional significance of this "nail" has not been determined[2]. Ancient folklore and beliefs argued it may have been used as a sting when the lion hunted its prey[1]. This structure has been previously described and a conclusion was made that the claw at the end of the lions tail was "merely a papilla endowed with blood vessels and nerves"[1]. Another historic belief was that the spike on the distal extremity of the lion's tail could be used by the lion to spike itself "in defiance of his enemies" in order to increase the lions' anger[3].

Tails from two sub-adult lion carcasses, fixed in 10% neutral-buffered formalin, were used. The distal 30 mm of each tail was removed. The hair was scraped off and the external features of the tail tip described and photographed using a stereo microscope. For histology preparation each tail tip was sectioned and routinely prepared for light microscopy. Sections were stained with haematoxylin and eosin (H&E), Masson's trichrome and Verhoef's stain. Immunohistochemical (IHC) labelling for Alpha-smooth muscle actin (SMA) was performed. Microscopically there were two notable features of the tail tip, namely, the vascular system associated with a central fat body and the tail tip, and the dermis and epidermis on the central, distal extremity which formed the tail spine (Fig. 1). The arteries terminated in the tail tip as the *Corpora caudalia* (Fig. 1). In the preglomic arterioles an internal elastic lamina was present and the *Tunica media* was a thick muscle layer which demonstrated positive IHC labelling for SMA. These branched to smaller arterioles, without an elastic lamina, and which fed directly into the Sucquet Hoyer canals (both vascular and nodular forms). In longitudinal section the spine could be distinguished into a lip, a moat, a wall and the point (Fig. 1). The collagen fibres of the dermis were circularly arranged around the terminal *Corpora caudalia.* As cylindrical structures bend and collapse on themselves, the volume held inside of them decreases[4]. This decrease in volume, combined with the deformation ability and elasticity of adipose tissue from the fat pad, could place pressure on the blood vessels within the glomus bodies. This increased pressure may act as a type of pressure pump for the blood vessels. Another possible contributing factor to the mechanical blood flow at the distal extremity of the tail could be the centrifugal force of the tail as it moves. This movement could aid in the pooling of blood into the glomus bodies, increasing the hydrostatic pressure and filling them. The abundant elastic fibres present in the lion tail, as well as the preglomic arterioles with internal elastic lamina, would allow a considerable amount of filling with blood and could also cause a pumping action pushing blood more proximally from the tail tip once the centrifugal force or pressure has ceased. Additionally, the bulges seen in Sucquet-Hoyer canals could also aid in filling with blood and allow increased expansion of the vessels when filled with blood. The possible mechanisms mentioned above involving the cylindrical structure of the tail tip may help to further enhance the blood flow and therefore increase perfusion to the tail tip of the lion. The function of the spine itself could be to act as an anchor for the skin and connective tissue to attach to. The base of conical structures has relatively large surface areas[4]. This relatively large surface area would allow tension applied to the spine to be dissipated[5]. Rather than a peculiar, stand-alone structure, the tail spine may rather be part of a system that has evolved to assist with blood flow and blood supply to the distal extremity of the tail. It may act as an exoskeleton support for the pumping of blood in the tail tip to prevent necrosis of the most distal extremity of the lion.

References:
1. Turner (1873) J. Anat. Physiol. 7, 271.
2. Nowak, R.M. (2018) Walker's mammals. Monotremes, marsupials, afrotherians, xenarthrans, and sundatherians. Baltimore, MD: Johns Hopkins University Press.
3. Owen, R. (1832) Proceedings of the Committee of Science and Correspondence of the Zoological Society of London Part II, Society
4. Sommerville, D.M.Y. (2016) Analytical geometry of three dimensions, Cambridge University Press
5. Karmokar, T. *et al.* (2021) Eng. Struct. 243, 112615.

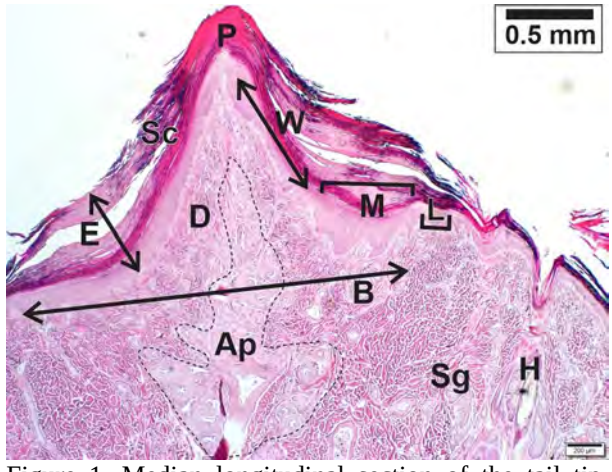

Figure 1. Median longitudinal section of the tail tip. Components of the spine are the base (B), lip (L), moat (M), wall (W) and the point (P). The *Str. corneum* is thicker in the region of the moat. The arterioles forming a plexus (Ap) (*Corpora caudalia*) are outlined. Epidermis (E), dermis (D), sebaceous gland (Sg) and hair follicle (H).

Corresponding author: martina.crole@up.ac.za

TAXONOMIC ANALYSIS OF CALANOID COPEPODS IN SOUTH AFRICAN LENTIC ECOSYSTEMS USING SCANNING ELECTRON MICROSCOPY

A.X. Kruger, C. Jansen van Rensburg and L.L. Van As

Dept. of Zoology and Entomology, University of the Free State, Bloemfontein

Taxonomic studies on Copepoda Milne Edwards, 1840, in southern Africa are limited and often outdated by up to 50 years. Traditionally, copepod morphological analysis has relied on line drawings. However, advancements in scanning electron microscopy (SEM) allow researchers to capture highly detailed images of important structures, enhancing documentation and aiding in creating more accurate line drawings. This study uses SEM techniques alongside traditional methods to provide detailed re-descriptions of known copepod species from lentic ecosystems in two South African regions. By integrating SEM micrographs with morphological data, we seek to fill significant taxonomic gaps and enhance the accuracy of copepod identification and classification. The largest family in the order Calanoida Sars GO, 1903 is Diaptomidae Baird, 1850, an exclusively freshwater family present in southern Africa. Two subfamilies, i.e. Paradiaptominae Kiefer, 1932 (*Lovenula* Schmeil, 1898, *Paradiaptomus* Sars GO, 1895 and *Metadiaptomus* Methuen, 1910) and Diaptominae Kiefer, 1932 (*Tropodiaptomus* Kiefer, 1932 and *Thermodiaptomus* Kiefer, 1932) have been recorded in Africa. Knowledge of the distribution of these subfamilies has been hampered by incomplete taxonomic knowledge and lack of available information[1,2]. Over two years, Copepoda specimens were collected from seven lentic systems in two South African provinces (Free State and KwaZulu-Natal). More than 500 specimens, representing diverse taxa, were analysed using light and scanning electron microscopy.

Specimens were preserved in 70% ethanol and prepared for SEM using adapted standard techniques[3], cleaned KOH to remove dirt, and larger species dried using hexamethyldisilazane (HMDS) instead of critical point drying[4]. Samples were sputter-coated with gold and analysed with a JEOL JSM IT200 SEM (Tokyo, Japan).

SEM analysis provided highly detailed images of copepod morphological structures, revealing diagnostic features for *Metadiaptomus transvaalensis* Methuen, 1910, *Tropodiaptomus schmeili* (Kiefer, 1926) and *Lovenula falcifera* (Lovén, 1846). This study updated morphological data, highlighting critical features using light and scanning electron micrographs, and included additional distribution data. The large 5th pereopod (P5) is the most critical diagnostic feature for calanoid copepods. Subtle differences in the P5, not always distinguishable with light microscopy, are better observed with SEM's 3D visualization. The P5 of *M. transvaalensis* females (Fig. 1A) shares similarities with that of *T. schmeili* (Fig. 1B). SEM provided detailed information to distinguish and differentiate these species. Smaller structures, such as spines, spinules, and setae on the antennules, offer valuable insights for species identification, particularly in male calanoids. A thumb-like structure on the antennule of *T. schmeili* (Fig. 2), typically a defining feature for *Tropodiaptomus hutchinsoni* (Kiefer, 1927), was clearly identified and documented. Lovenula species are distinguished by enlarged mandibles, but SEM micrographs are necessary to capture finer details for accurate differentiation. Additionally, the shape, position, size, and texture of larger spines on male calanoid antennules (Fig. 3) were documented to ensure comprehensive species descriptions. This study demonstrated the significant advantages of using scanning electron microscopy (SEM) in conjunction with traditional morphological techniques for taxonomic analysis of Copepoda. SEM provides highly detailed images of critical diagnostic features, which are often not visible using light microscopy alone. By accurately documenting these features, SEM enhances species identification and reduces potential confusion, ensuring more precise re-descriptions and identification of both known and new species. This integrative approach sets a robust foundation for future taxonomic and ecological research on copepods.

References:
1. Rayner N.A. and Heeg J. (1994) Hydrobiologia 272, 47.
2. Rayner N.A. (2001) Guides to the Freshwater Invertebrates of southern Africa. Pretoria, Water Research Commission.
3. Humphreys W.J., Spurlock B.O. and Johnson J.S. (1974) Proc. Illinois Tech SEM symposium, 1974, Chicago.
4. Braet F., De Zanger R. and Wisse E. (1997) J. Microsc. 186(1), 84.

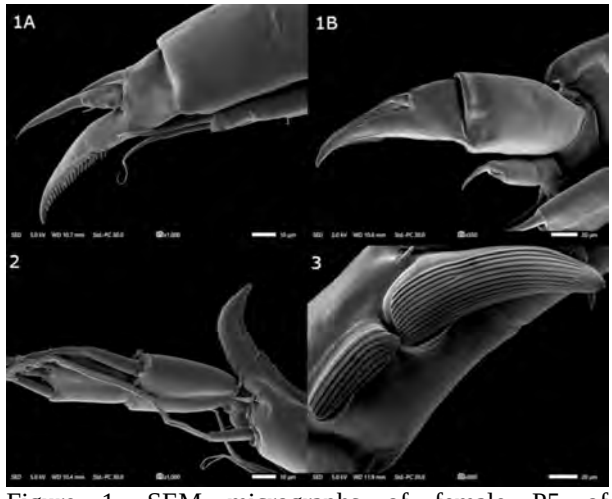

Figure 1. SEM micrographs of female P5 of *Metadiaptomus meridianus* (1A) and *Tropodiaptomus schmeili* (1B). Figures 2 and 3. Thumb-like spine (2) and large spine (3) on male antennule.

Corresponding author: anekekruger@gmail.com

MICROMORPHOLOGY AND ANATOMY OF *Tabernaemontana ventricosa* (FOREST TOAD TREE) FLORAL COMPONENTS

C.M. Naidoo[1], Y. Naidoo[2] and N.M. Mkolo[1]

[1]Dept. of Biology and Environmental Sciences, Sefako Makgatho Health Sciences University, [2]School of Life Sciences, University of KwaZulu-Natal, South Africa.

While laticifers are thought to constitute a synapomorphy in the Apocynaceae family, little is known about their distribution and form in the reproductive organs of their respective species[1]. *Tabernaemontana ventricosa* is a small to medium-sized, evergreen tree that may reach a height of 15 meters, and it is disjunctively distributed in Eastern Nigeria, Cameroon, Kenya, the Democratic Republic of Congo, South Africa, and several other countries[2]. The species grows best in disturbed, shaded environments and may be found in open woods and thickets in woodlands[3]. The bark, stems, and leaves of *T. ventricosa* are used in KwaZulu-Natal ethnomedicine to cure wounds, lower blood pressure, ease fever, and soothe painful eyes[2].

Research on *T. ventricosa*, is limited to a few studies on its chemical composition and biological activities, but none on the flower morphology of the species, hence the study was conducted to determine the general morphology, anatomy, and type of laticifers in the floral components of *T. ventricosa.*

The description of the floral morphology and anatomy were determined using stereo, light, and electron microscopy techniques. For stereomicroscopy, samples were viewed using the NIS-Elements D software on the Nikon AZ100 stereomicroscope equipped with a Nikon fiber Illuminator (Nikon, Tokyo, Japan). For scanning microscopy samples were prepared by fixed in 2.5% buffered glutaraldehyde, washed with phosphate buffer, post-fixed in osmium tetroxide (1%), dehydrated in a graded ethanol series, critical point-dried, mounted onto aluminium stubs, and sputter-coated with gold. The samples were viewed using a scanning electron microscope LEO 1450 (Zeiss) and images were captured using SmartSEM software.

For light microscopy, samples were prepared by fixation in glutaraldehyde for 24 hours, washed with phosphate buffer, post-fixed with osmium tetroxide (1%), dehydrated in acetone, and infiltrated with a Spurr's resin mixture. The samples were then embedded in resin and polymerized. The resin block samples were sectioned using a Leica EM UC7 ultra-microtome, and serial survey sections were analyzed using NIS-Elements D imaging software on the Nikon Eclipse 80i light equipped with Nikon DS-Fi1 compound microscope (Nikon, Japan).

The overall morphological findings confirmed that the inflorescence has a corymb pattern that extends 5-15 cm. The blooms are bisexual, salver-shaped, and whitish-yellow. In terms of anatomy, the colleters were present in the internal surface of the sepals and it was discovered that the laticifers, which showed intricate branching conformations, were randomly dispersed across the collora and calyx of staminate and pistillate flowers. Many species show laticifers in the sepals and pedicel of shorter-styled flowers, while they also occur in the sepals and pedicel of longer-styled flowers in most species belonging to the Apocynaceae family. Laticifers are often observed in the calyx of many other species studied and occasionally in the pistil[4].

References:
1. Marinho, C. and Teixeira, S.P. (2018) Plant Sys. and Evol. 305 (13),1.
2. Naidoo, C.M. *et al.* (2020). Plants. 9 (6), 686.
3. Schmelzer, G.B. and Gurib-Fakim, A. (2008). Medicinal Plants; plant resources of tropical Africa. Backhuys Publishers, Wageningen.
4. El Ajouz, B. *et al.* (2022). Protoplasma. 259 (2), 427.

Figure 1. Micrograph showing a cross-section of the bud of T. ventricosa. Scale bar = 2 mm.*T. ventricosa.* Scale bar = 2 mm.

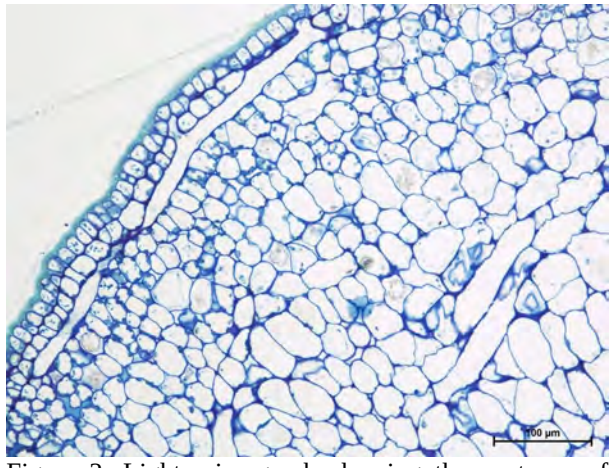

Figure 2. Light micrograph showing the anatomy of laticifers in the sepal of T. ventricosa. Scale bar = 100 µm. *T. ventricosa*. Scale bar = 100 µm.

Corresponding author: clarissa.naidoo@smu.ac.za

POLLINATOR REWARDS IN *Nemesia* (SCROPHULARIACEAE)

H. Grobler[1,2], M. Jackson[1] and L. Joubert[1]

[1]Department of Plant Sciences (Botany), University of the Free State (UFS), Bfn, [2]Centre for Microscopy, UFS, Bfn

Most flowering plants rely on biotic vectors, such as insects or vertebrate animals, for pollination[1]. Several floral innovations evolved for attracting and rewarding pollinators or otherwise manipulating pollinator behaviour, to promote reproductive success of the plant. One example of such an innovation is the floral spur, a hollow, tubular outgrowth of a floral organ, which generally secretes and/or contains a pollinator reward, such as nectar or oil. In *Nemesia* (a genus of nearly 77 flowering plant species, endemic to southern Africa) the floral spur of several species has been found to contain nectar, while others appeared to be empty[2]. Since *Nemesia* is closely related to genera which contain oil-secreting trichomes inside and/or around their spurs[3], the possibility of oil as a pollinator reward in *Nemesia* should be investigated.

The aim of this study was to investigate the pollinator rewards (nectar, oil or none) and secretory structures present inside the spur of *Nemesia*. For this study, three *Nemesia* species with variation in spur shape and size were selected, namely: *N. strumosa* (Fig. 1A) with a broad saccate spur, *N. barbata* (Fig. 1B) with a conical spur and *N. macrocarpa* (Fig. 1C) with a narrow tubular spur. The internal spur epidermal surface was observed using scanning electron microscopy (SEM) and histological staining was performed to identify possible precursors of pollinator rewards, such as lipids, starch and carbohydrates within the epidermal cells and glandular trichomes of the spurs.

Sample preparation for SEM included fixation, dehydration, critical point drying, specimen mounting and sputter coating. Images were captured using a JEOL JSM-7800F SEM. For histological investigation, specimens were embedded in epoxy resin or paraffin wax, sectioned and stained using Toluidine Blue O (lipids), Safranin O and Orange G (starch) and Periodic Acid-Schiff (insoluble polysaccharides). Sections were imaged with a Nikon ECLIPSE TE200-E microscope.

This study is the first to investigate secretory structures in the spur of *Nemesia*, and several trichome types were identified. Results of SEM and histochemical staining for *N. strumosa* (Fig. 2A, D) and *N. barbata* (Fig. 2B, E) showed potential for secretion from glandular trichomes, while no characteristics associated with secretion were observed for the clavate trichomes of N. *macrocarpa* (Fig. 2C, F). It could not be confirmed whether nectar or oil is secreted by the former two species, and further staining and microscopy techniques should be explored.

Nemesia displays a variety of spur shapes and potentially also provides a range of different pollinator rewards. This makes it an ideal model system for investigating the role of pollinator shifts and floral key innovations in driving diversification in flowering plants and insect pollinators.

References:
1. Ollerton, J., Winfree, R. and Tarrant, S. (2011) Oikos 120: 321.
2. Steiner, K.E. (1996) Systematic Botany 21: 63.
3. Possobom, C.C.F. and Machado, S.R. (2017) Acta Botanica Brasilica 31(3): 503.

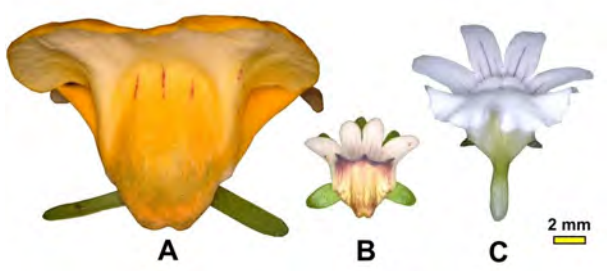

Figure 1. (A) *Nemesia strumosa*, (B) *N. barbat*a and (C) *N. macrocarpa*. Scale bar = 2 mm.

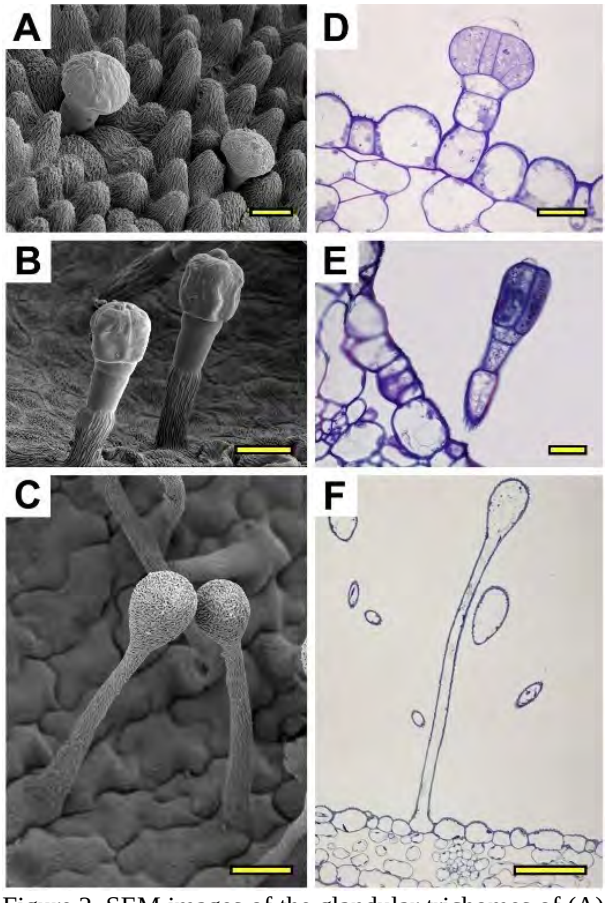

Figure 2. SEM images of the glandular trichomes of (A) *N. strumosa* and (B) *N. barbata.* (C) The clavate trichomes of *N. macrocarpa*. Toluidine Blue O (TBO) stained cross-sections of trichomes in (D) *N. strumosa*, (E) *N. barbata* and (F) *N. macrocarpa*. Scale bar: (A - E) = 20 µm, (F) = 60 µm.

Corresponding author: groblerh@ufs.ac.za

INVESTIGATION OF THE EFFECT OF PEG-AuNPs ON COLORECTAL CANCER CELL LINE

D. Basson [1], S. Roux[1] and J. Wesley-Smith[2]

[1]Department of Physiology, Nelson Mandela University, Gqeberha , [2]Empower Microscopy

Colorectal cancer (CRC) is the third most diagnosed cancer globally. Despite a growing understanding on the causes of CRC, the incidence of CRC has continued to increase, presenting 1.9 million new cases globally in 2020[1]. The limitations in current treatments result in high mortality figures, highlighting the need for more effective therapeutic approaches. Gold nanoparticles (AuNPs) have emerged as a promising avenue for cancer treatment, attracting researchers due to their biocompatibility, thermal activity, optical and electrical properties[2]. However, AuNPs face limitations in therapeutic use due to their instability and tendency to aggregate in biological media[3]. Polyethylene glycol (PEG) modification reportedly stabilizes AuNPs in high ionic solutions, as well as increase their biocompatibility[4]. The unique anatomical and pathophysiological nature of tumours allows a disproportionate accumulation of nanoparticles in the tumour microenvironment, which is known as the "enhanced permeability and retention (EPR) effect"[5]. The increased permeability of the tumour vasculature and poor lymphatic drainage allows nanoparticles to specifically target the tumour environment through passive targeting[5] Once accumulated, PEG-AuNPs have shown to cause cell damage through the generation of reactive oxygen species (ROS)[6]. The aim of this project is to synthesize PEGylated AuNPs and determine their potential cytotoxicity and specificity *in vitro* using a colorectal cancer cell line, HT-29.

Citrate-capped AuNPs (c-AuNPs) were synthesised using the Turkevich-Frens method[7,8] followed by a surface modification step with PEG through ligand exchange to produce PEG-AuNPs. The stability and size of the NPs were characterized using ultraviolet–visible spectroscopy, dynamic light scattering, and zeta-potential. For ultrastructural studies, coverslips with cells previously treated with 200 ug/mL PEG-AuNPs were fixed in 2% buffered glutaraldehyde, post-fixed in 1% aqueous osmium tetroxide and dehydrated in a graded acetone series (25-100%). They were infiltrated and embedded in epoxy resin, sectioned to 1µm thickness for light microscopy (LM) and 70 nm for transmission electron microscopy (TEM) observation. For SEM, samples in 100% acetone were exposed to increasing hexamethyldisilane concentrations (30, 60, 100%) and allowed to dry slowly.

The synthesised c-AuNPs showed a strong absorption peak at 518 nm (Fig. 1a), a mean hydrodynamic size of 20.5 nm and a core size of 14.7 nm (Fig.1b). After PEGylation, there is a red shift in the absorption spectra to 523 nm, and an increase in the hydrodynamic size to 23.8 nm, indicating successful surface modification. LM of HT-29 cells treated with 200 ug/mL PEG-AuNPs (Fig. 2b) showed evidence of membrane blebbing and deformed nuclei, which were not observed in cancer control cells (Fig. 2a). TEM revealed an uptake of PEG-AuNPs into the cytoplasm of treated cells (not shown). SEM examination of the surface topography of the HT-29 cells confirmed the presence of pronounced membrane blebbing in PEG-AuNPs treated cells (Fig. 3b) which contrasted with the normal membrane evaginations and substrate attachments of control cells (Fig. 3a). Both nuclear irregularities and membrane blebbing are morphological characteristics commonly associated with cellular stress and apoptosis, confirming the cytotoxicity and preference of PEG-AuNPs to target tumour cells.

References:
1. Sung, H. *et al*. (2021) CA Cancer J. Clin. 71(3), 209.
2. Jin, C. *et al.* (2020) Int. J. Med. Sci. 17(18), 2964.
3. Anik, M. I. *et al*. (2022). Nano Select. 3(4), 799.
4. Guerrini, L., Alvarez-Puebla, R.A. and Pazos-Perez, N. (2018) Materials (Basel) 11(7), 1154.
5.Yang,W. *et al*. (2019) Sust. Mat. and Technol. 22:e00109.
6. Patlolla, A.K., Kumari, S.A. and Tchounwou, P.B. (2019) Int. J. Nanomed. 14, 639
7. Turkevich, J. Stevenson P.C. and Hillier, J. (1951) Faraday Discuss Chem Soc. 11, 55.
8. Frens, G. (1973) Nat Phys Sci. 241, 20.

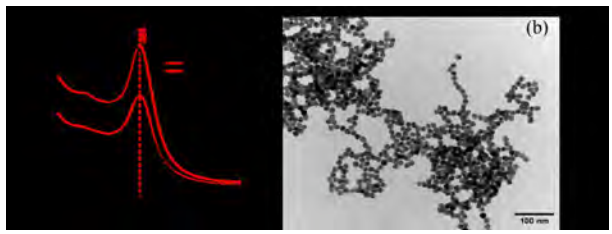

Figure 1. (a) Absorption spectra of c-AuNPs and PEG-AuNPs. (b) TEM image of c-AuNPs synthesised.

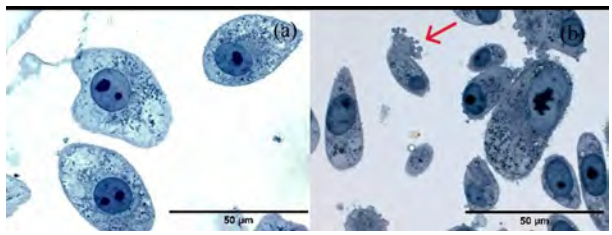

Figure 2. (a) Control; (b) PEG-AuNP treated cells showing nuclear irregularities and membrane blebbing (arrow).

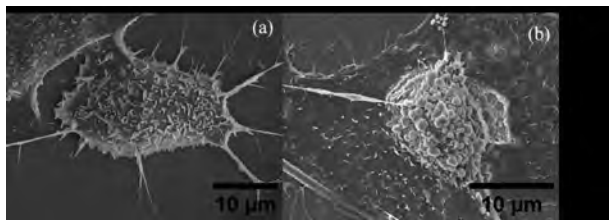

Figure 3. SEM images of HT-29 cells (a) control, and (b) PEG-AuNP treated showing extensive membrane blebbing.

Corresponding author: s219222649@mandela.ac.za

HISTOLOGICAL EFFECTS OF CTCE-9908 AND L-KYNURENINE ON MELANOMA METASTASIS IN A XENOGRAFT MOUSE MODEL

M.J. Olfsen[1], P. Bipath[2], Y.N. Hlophe[2] and J.C. Serem[1]

[1]Dept. of Anatomy, [2]Dept. of Physiology, University of Pretoria, Pretoria

Melanoma, an aggressive skin cancer, is on the rise in South Africa and worldwide[1]. CTCE-9908, a chemokine receptor 4 inhibitor and L-kynurenine, a tryptophan-kynurenine pathway metabolite, have shown to inhibit melanoma in vitro[1]. This study was designed to analyse the histological effects of CTCE-9908 and L-kynurenine individually and in combination on the liver, kidneys and lungs of a xenograft immunocompetent (C57BL/6) mouse model with the B16F10 melanoma cell line.

Forty-two immunocompetent mice were used: two as negative controls without tumours and forty xenografted with 1X106 per mL B16F10 melanoma cells, grouped into five: tumour only (no treatment), positive control (nocodazole treated), CTCE-9908 treated and L-kynurenine treated individually and in combination. The liver, kidney and lungs were collected, embedded in paraffin wax, stained using haematoxylin-eosin and Masson's Trichrome stains, and then stained using light microscopy.

Histological analysis with haematoxylin-eosin staining revealed normal architecture in the liver, kidney, and lungs of the negative control groups. In contrast, the tumour groups showed severe damage and cellular alterations. The liver exhibited hepatocellular hypertrophy and necrosis[2], the kidneys presented with tubule dilation and intensely stained eosinophilic cytoplasm[3], and the lungs showed severe alveolar haemorrhage, edema, alveolar epithelial thickening and bronchiole epithelial necrosis[4]. In the treated groups, the liver's architecture in the positive control and CTCE-9908 groups was normal, with the L-kynurenine group exhibiting sinusoidal dilation and karyocytomegaly[2]. The kidney's architecture in the positive control and CTCE-9908 group was normal, with mild tubular dilation, slight loss of brush borders and renal tubular epithelium in the CTCE-9908/L-kynurenine treated group[3]. The lung's architecture in the positive control and the CTCE-9908/L-kynurenine group presented normal, with severe haemorrhage and congestion in the L-kynurenine treated group[4]. Masson's Trichrome staining revealed normal collagen deposition in the negative controls and increased collagen deposition and fibrosis in the tumour groups (Fig. 1B), and the CTCE-9908/L-kynurenine kidney group (Fig. 1C). No changes were observed with any of the treatments, besides the CTCE-9908/L-kynurenine kidney group (Fig. 1C) that showed tubulointerstitial fibrosis[5].

CTCE-9908 shows potential as an effective treatment for melanoma metastases to the liver and kidney. Additionally, the CTCE-9908/L-kynurenine combination group shows promise for the treatment of metastases to the lungs.

References:
1. Nkandeu, D.S. *et al.* (2022) Cell Biochem. and Funct. 40(6), 608. DOI: 10.1002/cbf.3731.

2. Thoolen, B. *et al.* (2010) Toxicol. Path. 38(7_suppl), 5S.

3. Nguyen, T.T.U. *et al.* (2024) Scient. Rep. 14(1), 9010.

4. Almeida, C. *et al.* (2013) PLoS ONE. 8(1), e53628.

5. Cao, Q. *et al.* (2022) JCI Insight 7(4).

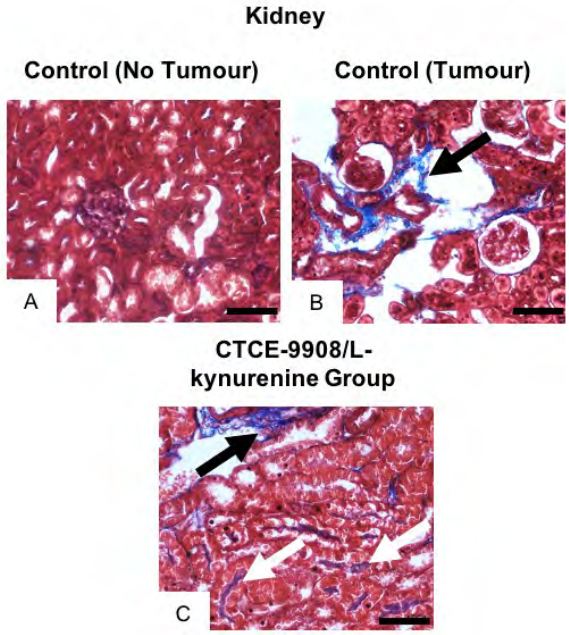

Figure 1. A. Control (negative); kidney. B. Tumour control (no treatment); kidney. C. CTCE-9908/L-kynurenine treated group; kidney. Masson's Trichrome stain of rodent (mouse) kidney tissue. Severe fibrosis (black arrow) is visible in the tumour control (B) and in the CTCE-9908/L-kynurenine treated group (C). Tubulointerstital fibrosis (white arrow) is displayed in the CTCE-9908/L-kynurenine group (C). Scale bar = 20 µm

Corresponding author: meganolfsen9@gmail.com

HIPPOCAMPAL VULNERABILITIES IN MATERNAL BRAINS: EFFECTS OF INTRAUTERINE GROWTH RESTRICTION IN ADULT FEMALE MICE

T.A. Yusuf , R.B. Bamidele , A.A. Bello and P.D. Shallie

Department of Anatomy, Olabisi Onabanjo University, Ogun State, Nigeria

Intrauterine growth restriction (IUGR) is a significant prenatal complication characterized by suboptimal fetal growth and significant perinatal mortality. It results from impaired nutrient and oxygen delivery to the fetus, affecting approximately 10% of pregnancies worldwide. IUGR is associated with numerous adverse outcomes, including developmental delays and increased risk of neurological disorders. While the adverse effects of IUGR on fetal brain development are well-documented, the potential impact on the maternal brain has been largely overlooked. The hippocampus, a critical region involved in memory and learning, is particularly susceptible to developmental disturbances, making it a focal point for studying the effects of IUGR. Both gestational malaria and preeclampsia are established risk factors for IUGR. This study aims to investigate the effects of early onset IUGR, induced by a double knockout model using *Plasmodium berghei* (PB) to simulate gestational malaria and L-Nitro Arginine Methyl Ester (L-NAME) to induce preeclampsia, on the histoarchitectural integrity of the hippocampus in adult female mice.

Forty adult female BALB/c mice were divided into 5 groups prior to mating: Group A (Non-pregnant Control), Group B (Pregnant Control), Group C (PB only), Group D (L-NAME only), and Group E (PB + L-NAME). PB was administered intraperitoneally at 0.2 ml once, while L-NAME was administered subcutaneously at 50 mg/kg/day from gestational days 7 to 17. Neurobehavioral assessment using the Y-maze test was conducted post-induction to evaluate spatial reference memory. Following behavioral testing, mice were sacrificed and hippocampal tissues were analyzed histologically using Hematoxylin and Eosin (H&E) and Kluver-Barrera stains to assess histoarchitectural changes.

Neurobehavioral results revealed significant impairments in the IUGR-induced groups (PB and PB + L-NAME), evidenced by reduced exploration of the novel arm in the Y-maze, indicating spatial memory deficits. Marked hippocampal alterations, including distorted histoarchitectural integrity, pyknotic cells bodies, loss of myelin integrity and neuronal degeneration were observed in the dentate gyrus granular layer in the induced groups (PB and PB + L-NAME) compared to controls. Notably, no significant histopathological changes were observed in the L-NAME only group, suggesting that the combination of gestational malaria and preeclampsia poses a greater risk to hippocampal integrity.

These findings demonstrate that the adverse effects of early onset IUGR extend beyond the fetal brain, impacting the maternal brain's structural and functional integrity. This study underscores the importance of considering maternal neurological health in the context of prenatal complications.

References:
1. Brown, A. S. *et al.* (2021) eNeuro, 8(5).
2. Sharma D. *et al.* (2016) J. Matern. Fetal Neonatal Med. 7, 1.
3. Fattal-Valevski A. *et al.*, (2009) J Child Neurol. 24, 846.

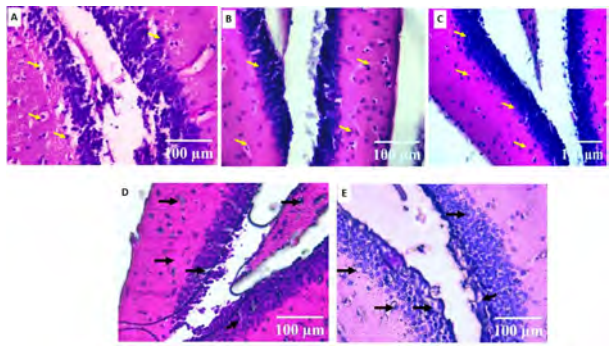

Figure 1. H&E A) Negative control, B) Neg. control pregnant, C) L-NAME D) *P. berghei* E) L-NAME + *P. berghei* groups exhibiting cellular degeneration and pyknotic changes (black arrows)

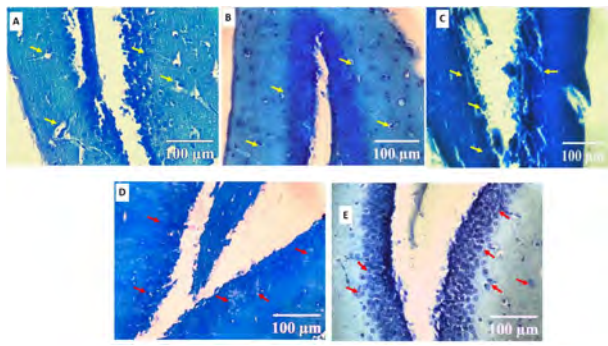

Figure 2. KB, X400 A) Negative control B) Neg. control pregnant C) L-NAME D) P. berghei E) L-NAME + P. berghei with granule neuron degeneration and more poorly stained neurons (red arrows) *P. berghei* E) L-NAME + *P. berghei* with granule neuron degeneration and more poorly stained neurons (red arrows)

Corresponding author: adesholabaylow@gmail.com

BACK TO BASICS WHEN MOLECULAR SEQUENCES ARE NOT IN PLACE, YET

L.L. Van As[1] and K.W. Christison[2]

[1]Dept of Zoology and Entomology, University of the Free State, [2]Dept. of Forestry, Fisheries and Environment, SA

Argulus Thiele, 1900 is the only genus of the Argulidae with a worldwide distribution, with more than 150 known species. Six species are known from South Africa, with four species, i.e. *A. belones* van Kampen, 1909, *A. multipocula* Barnard, 1955, *A. kosus* Avenant-Oldewage, 1994, and *A. izintwala* van As and van As, 2001, described from marine or estuarine fishes, and two *A. capensis* Barnard, 1955 and the introduced *A. japonicus* Thiele, 1900 infect freshwater fish. *Argulus kosus* was originally described from Kosi Bay, from the strepie *Salpa salpa*, based on the female[1]. Five years later, *A. kosus* male was collected in St. Lucia from eight other fish hosts, with additional body measurements and information provided for the female[2].

During fish health surveys conducted by the Dept. of Forestry, Fisheries and the Environment in Kwa-Zulu Natal (KZN), argulid specimens were collected from a semi-closed pond system from *Pomadasys commersonii* (Spotted grunter) and *Rhabdosargus holubi* (Cape stumpnose).

By examination of the literature[1,2], preserved material in the collection of the Aquatic Parasitology lab (UFS) and comparison of the newly collected KZN material, sufficient morphological data were obtained to identify the aquaculture derived specimens as *A. kosus.* These were done using standard stereo- and scanning electron microscopy (SEM) techniques. Figures were produced with the aid of a Zeiss Lab 18 microscope and attached drawing tube. Micrographs were taken on a JEOL JSM 7800F at 5 kV.

All taxonomic characteristics between the material examined were the same. These included features of the cephalic lobe with scale studded frontal region (Figs 1A,B); antennae (Fig. 2A,B); antennule; sucker; maxilla with basal plate and accessory spines (Figs 3. A,B); respiratory areas; thorax with scabrous areas (Figs 1A,C); legs; natatory lobes; abdomen with testis or spermathecae, depending on the sex.

Molecular sequences available on GenBank, reveals data of only nine species, i.e. *A. americanus, A. bicolor, A. benegalensis, A. flavescens, A. foliaceus, A. japonicus, A. nobili, A. pugettensis* and *A. siamensis* from USA, India and China. In the absence of molecular sequence data available from South African Argulids on existing databases, these robust morphological characters still allow for unambiguous taxonomic assignment to *A. kosus.* Sequence data generated from the aquaculture-derived specimens (KZN) are being processed, however with no published molecular information from South Africa or even other African species, no phylogenetic conclusion could be made yet.

Therefore, depending on the taxon in question and the systematic information available, such as the presence of robust, valid, comparative, taxonomic characteristics, the modern taxonomist is often obliged to go back to the basics. This will imply comparison of morphological information using microscopy.

References:
1. Avenant-Oldewage, A. (1994) Koedoe, 37, 89.
2.Van As, J.G., Van Niekerk, J.P. and Olivier, P.A.S. (1999). Systematic Parasitology, 43, 75.

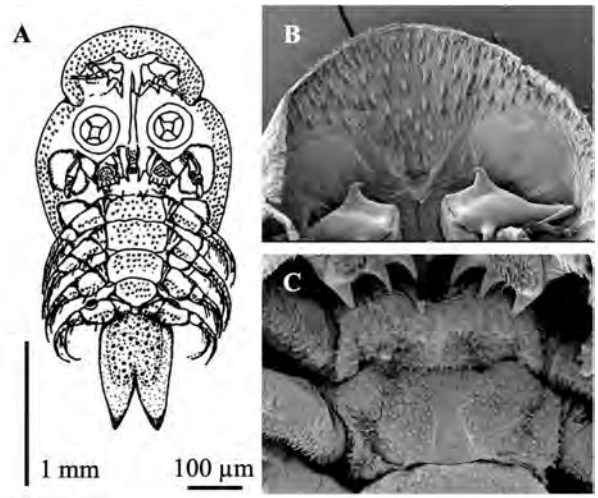

Figure 1. Figure 1. Microscope drawing (A) and SEM micrographs (B, C) of *Argulus kosus*. A. Male, ventral view; B. Frontal region of anterior carapace; C. Thoracic segment with scabrous areas.

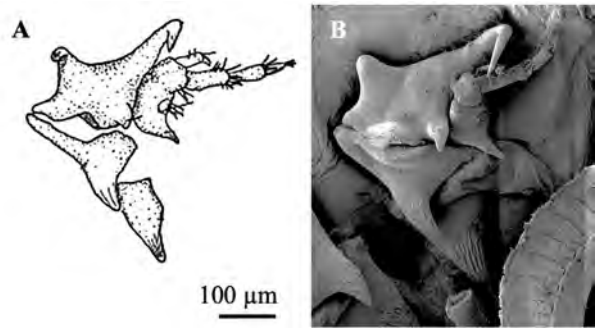

Figure 2. Figure 2. Microscope drawing (A) and SEM micrograph (B) of antenna of Argulus kosus.*Argulus kosus.*

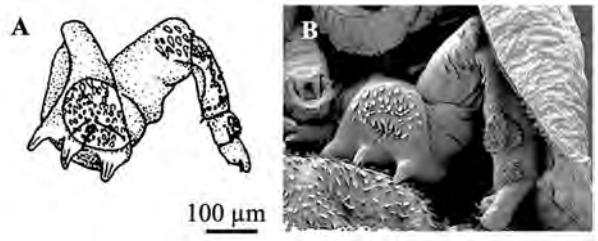

Figure 3. Figure 3. Microscope drawing (A) and SEM micrograph (B) of maxilla with scabrous areas of Argulus kosus. *Argulus kosus.*

Corresponding author: vanasll@ufs.ac.za

CHARACTERISATION OF STEEL MARTENSITE USING ELECTRON BACKSCATTERED DIFFRACTION

S. Allies[1,2], R.D. Knutsen[1,2] and J.E. Westraadt[3]

[1]Electron Microscope Unit, [2]Centre for Materials Engineering, UCT, South Africa, [3]The Ohio State University, USA

The mechanism of martensite (α′) formation in steels, although highly complex, is now well understood. However, the morphology, size and variant selection can vary substantially depending on steel composition and thermal processing[1]. In the present case, a power plant 12Cr steel, referred to as X20 steel, has been subjected to a non-standard heat treatment that involves incomplete α′ formation prior to reheating for the tempering cycle. Consequently, the initial untransformed austenite that survives the tempering cycle forms second generation α′ on final cooling to room temperature. During conventional heat treatment the M_s-M_f range is 275-750 °C, but if cooling is terminated at 250 °C and reheated to 760 °C, the residual austenite transforms to α′ at 390 °C upon cooling. The higher M_s temperature for the formation of second-generation α′ is indicative of lower solute content in the austenite but also possibly leads to differences in the α′ characteristics which could impact on mechanical property development. Orientation imaging using electron backscattered diffraction (EBSD) in the scanning electron microscope (SEM) has been used to compare the two α′ generations.

Samples representing the conventional martensitic heat treatment (100% primary α′ = X20AP) and the incomplete primary α′ heat treatment containing an approximate mix of 20% primary and 80% secondary α′ (X20AS) were investigated. The X20AS sample was subjected to the incomplete cooling and reheating cycle described above. Orientation imaging was performed using a Tescan MIRA 3 SEM fitted with an Oxford Instruments EBSD detector. The SEM was operated at 15 kV and probe current in the range 2-3 nA. Data was acquired at step size in the range 0.08-0.2 µm and processed using AztecCrystal 3.1 software. The Euler colour orientation images for the X20AP and X20AS samples are presented in Figs. 1 and 2 respectively.

Interpretation of the orientation images focused on analysing the special grain boundaries that develop during lath and plate α′ formation. The 24 variants that occur as a result of the Kurdjumov-Sachs orientation relationship between austenite and α′ produce the following possible grain boundary misorientations[1]: 10.5°[011]; 49.5°[011]; 60°[011] and 70.5°[011]. The latter misorientation is equivalent to the 60°[111] twin relationship. The relative fractions of these boundaries are reported to be sensitive to composition and can be used to characterize the α′. However, a problem is noted to occur when the 60°[111] is included due to the incidence of pseudo-symmetry (p-s) measurements of the same orientation. Distinguishing between 60°[111] variant boundaries and p-s measurements is difficult. For example, for the X20AP sample, the fraction of 60°[111] boundaries can change from 44% to 37% when 60°[111] boundaries of selective minimum size, suggesting pseudo-symmetry, are removed. But there is little confidence that this approach eliminates all p-s data points or indeed if it also eliminates variant misorientations. Thus, the proportion of all other special grain boundaries is affected by the uncertainty in the classification of the 60°[111] boundaries.

A more objective approach has been affirmed by determining the combined 49.5°[011] and 60°[011] boundary length per area. In this case the average for X20AP is 0.48µm^{-1} and 0.23 µm^{-1} for X20AS. These values are consistent with the size difference of the α′ block boundaries (>45°) indicated as white lines in the orientation images below. Given that the major fraction of α′ in X20AS started to form at 390 °C, it is evident that the α′ morphology is much coarser for the X20AS heat treatment cycle compared to the α′ that forms during the conventional initial cooling to room temperature.

References:
1. Morito, S. *et al*, (2003) Acta Mater. 51, 1789.

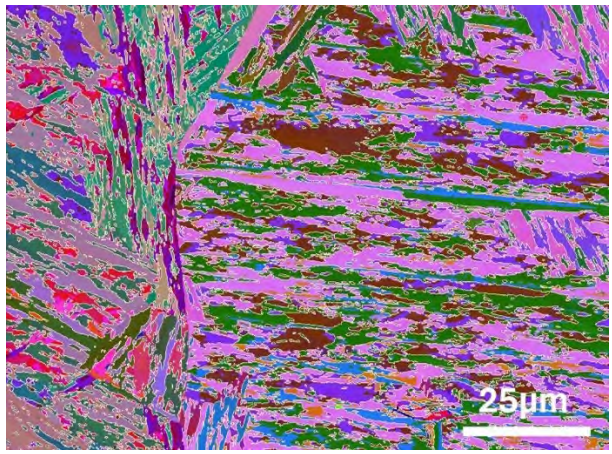

Figure 1. EBSD orientation image (Euler colour) for sample X20AP.

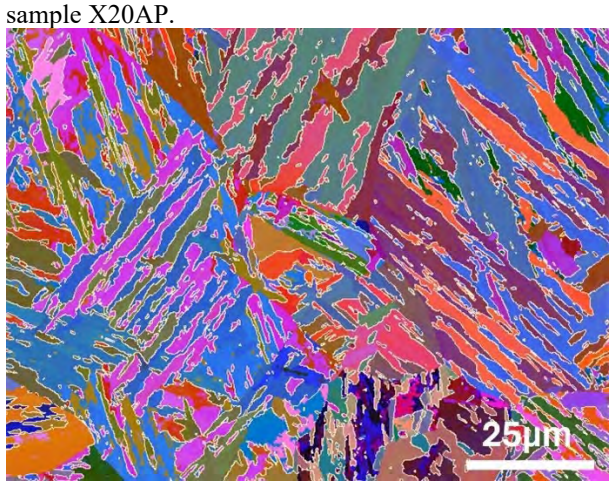

Figure 2. EBSD orientation image (Euler colour) for sample X20AS.

Corresponding author: ALLSOR002@myuct.ac.za

EFFECT OF WELDING ON SECONDARY PHASES IN SERVICE-EXPOSED 12%Cr TMF STEEL

G Marx[1], J.E. Westraadt[2] and E.J. Olivier[1,3]

[1]Centre for HRTEM, Nelson Mandela University, Gqeberha, [2]Centre for Electron Microscopy and Analysis, The Ohio State University, Ohio, USA, [3]Department of Physics, Nelson Mandela University, Gqeberha

The current economic climate drives partial component replacement in the existing infrastructure at fossil-fuel power plants. This entails welding on the service-exposed components. Tempered martensite ferritic (TMF) steels with 9-12% Cr are mainly used in the steam pipes, turbines and boilers. These steels are stable during creep (service) due to the strengthening offered by Cr-enriched $M_{23}C_6$ carbides located at the grain boundaries, and the V-enriched MX carbonitrides distributed homogeneously throughout the ferrite matrix1. Other secondary phases such as Mo-enriched Laves and modified Z-phase (Cr(Nb,V)N) precipitate during creep[1,2]. Z-phase formation involves the dissolution of the MX carbonitrides. It has been found that cross-welds of virgin onto service-exposed X20 (12% Cr) steel failed consistently in the fine-grained heat-affected zone (FGHAZ) of the crept material, which is known as Type IV cracking[3]. Accelerated precipitate coarsening and dissolution occur in the FGHAZ. This results in insufficient grain boundary pinning and subsequent sliding, leading to void formation from the decohesion between the precipitate and matrix. Hence, retained precipitates act as preferred nucleation sites for creep voids. Not much is known about the evolution of the existing precipitates when welding on service-exposed TMF steels. This study investigates the effect of welding on the secondary phases in a service-exposed TMF steel. The results are then used to identify any contributions to Type IV cracking.

The material used for this study was service-exposed (555°C; 17.0 MPa; 130 kh) X20CrMoV11-1 (12% Cr) stainless steel. Weld thermal cycle simulation on a Gleeble™ 3800 (T_p = 980 °C, 200 °C/s heating rate, 4 s hold) and post-weld heat treatment (740 °C, 45 min) was performed on the bulk parent X20 steel for larger sampling areas of homogeneous FGHAZ microstructure. Electron-transparent thin foils were prepared using twin-jet electropolishing and extraction replicas were prepared by extracting precipitates from the surface of a pre-polished bulk sample onto a thick carbon layer. Backscattered electron (BSE) images (5 kV, 0.20 nA, 4 mm working distance) were acquired from the thin foil specimens using an FEI Helios Nanolab 650 Focused Ion Beam (FIB)-SEM. Cr and V elemental maps were acquired with energy-filtered transmission electron microscopy (EFTEM) using a Gatan Quantum GIF fitted to a JEM JEOL2100 (LaB_6) TEM operated at 200 kV. Further TEM analysis was performed using a double-aberration corrected JEOL JEM-ARM 200F operated at 200 kV and equipped with a Gatan GIF 965ERS dual electron-energy loss spectrometer (EELS) (results not shown). Features were extracted from the various images for further measurements using the MIPAR™ image analysis software[4].

Fig. 1 shows how the various precipitates have been identified for analysis from the BSE images and EFTEM elemental maps. Statistically low numbers of Laves phase precipitates were observed in all the specimens. Z-phase precipitates were observed from the EFTEM RGB composite maps as areas of overlap between the Cr (green) and V (red) elemental maps as shown in Fig. 1(b). Both the service-exposed parent and FGHAZ X20 contained Z-phase precipitates. During FGHAZ simulation it was found that for both the $M_{23}C_6$ and MX precipitates, there is a decrease in mean size d, an increase in number density N_v and a large variation in the interparticle spacing λ, which is ascribed to the dissolution of precipitates and subsequent nucleation of fine new precipitates or Ostwald ripening of retained precipitates during welding. Considerably large $M_{23}C_6$ carbides (d > 300 nm) were observed in the service-exposed FGHAZ material.

Coupling the presence of the Z-phase and large $M_{23}C_6$ precipitates in the service-exposed FGHAZ with high coarsening rates in the FGHAZ, it can be concluded that (1) the creep strength will decrease detrimentally due to MX dissolution and (2) accelerated void formation will occur which explains the consistent failure of service-exposed weldments by Type IV cracking. It was expected that there would be no Z-phase present in the FGHAZ since previous studies have shown that Z-phase precipitates dissolve and reform MX above 800 °C[2]. This warrants further investigation. Future work will include quantitative analysis of the Z-phase precipitates.

References:
1. Kostka, A. *et al.* (2007) Acta Mat. 55(2), 539.
2. Danielsen, H.K. and Hald, J. (2006) Energy Mater. 1, 49.
3. Rasiawan, T. (2017) MEng Dissertation, University of Cape Town, South Africa.
4. Sosa, J.M. et al. (2014) Integr. Mater. Manuf. Innov. 3(1),10.

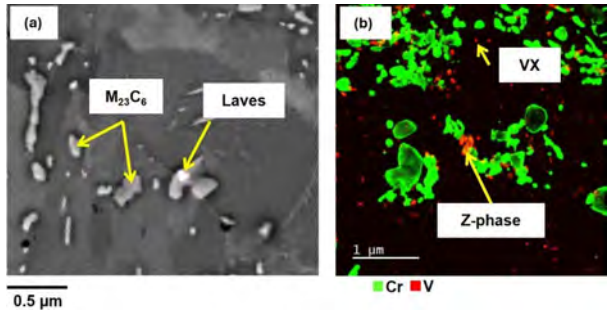

Figure 1. (a) BSE image from thin foil specimen and (b) EFTEM RGB composite map of Cr (green) and V (red) elemental maps acquired from extraction replica specimen of the service-exposed FGHAZ X20 steel.

Corresponding author: Geneveve.Marx@mandela.ac.za

DISLOCATION DENSITY MEASUREMENT IN AISI316L STAINLESS STEEL USING ELECTRON CHANNELING CONTRAST IMAGING (ECCI)

L. C. M. Pullen[1], J.E. Westraadt[2], R.D. Knutsen[3] and D. Ramasimong[3]

[1]Center for HRTEM, Department of Physics, Nelson Mandela University, [2]Center for Electron Microscopy and Analysis (CEMAS), The Ohio State University, [3]Centre for Materials Engineering, University of Cape Town

Dislocations play an important role in the mechanical properties of steels which continuously evolve during component manufacturing and subsequent in-service exposure due to creep and/or fatigue. The dislocation density of the steels can potentially be used as a fingerprint to identify at-risk components that has either reached end-of-life or that was incorrectly manufactured due to forming or heat treatments. Traditionally, dislocation measurements are performed using transmission electron microscopy (TEM) performed on thin foils samples. However, accurate and precise measurements of the dislocation density in steels using TEM remain a challenge due to the time-consuming nature, small sampling volumes, and effects of sample preparation on the quantitative results. The aim of this study is to evaluate and establish electron channelling contrast imaging (ECCI) as a scanning electron microscopy method of quantifying the dislocation densities of power plant steels.

Samples consisting of AISI316L stainless steel were used as a model alloy (large grain size ~100 µm) to compare dislocation imaging using annual dark field (ADF)-scanning TEM (STEM) and ECCI. Three materials states consisting of a cold drawn rod (high dislocation density), annealed rod (low dislocation density), and an annealed sample subjected to cyclic fatigue testing (medium dislocation density) were investigated. Systematic investigations into the data acquisition parameters showed that an incident beam energy (20 kV), beam current (~4 nA), pixel size (5 nm), and working distance (4-5 mm) on a JEOL7001F SEM fitted with a retractable BSE detector could successfully image the dislocation structures for the material states used in this study. The ECCI technique was then successfully used to determine the dislocation density in the three material states and the quantitative results showed similar trends as the ADF-STEM quantification results, but with less effort.

The application of ECCI on polycrystalline materials smaller grain sizes (<10 µm) remain a challenge since the dislocation contrast is very sensitive to the grain orientation. Future studies using electron backscattered diffraction (EBSD) orientation mapping combined with electron channelling pattern (ECP) calibrations using a single crystal Si sample will allow for ECCI imaging under controlled grain orientations. Furthermore, accurate image segmentation of dislocations from a micrograph remains a key limitation, which can be improved with the use of advanced image analysis based on deep learning approaches.

References:
1. Gutierrez-Urrutia, I., Raabe, D. (2011) Scripta Materialia 66, 343 – 346.
2. Andrea, B. (2019) Automatic Characterization of dislocation Structures via Scanning Electron Microscopy. Masters' Thesis. Politecnico Di Torino.

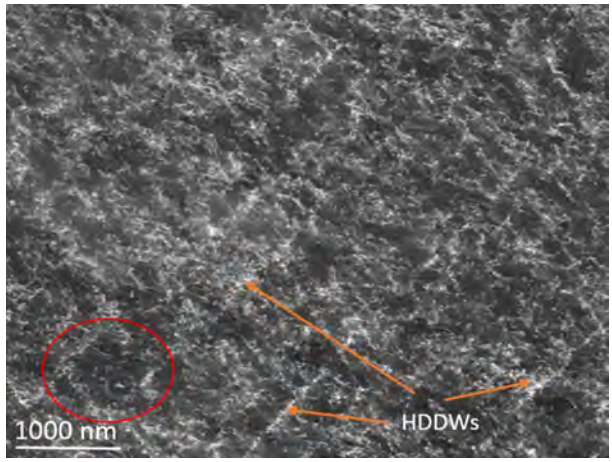

Figure 1. ECC image of the beginning of a dislocation cell (in red) and high-density dislocation walls (HDDWs) in an AISI 316L stainless steel sample that underwent 11M cycles of fatigue loading.

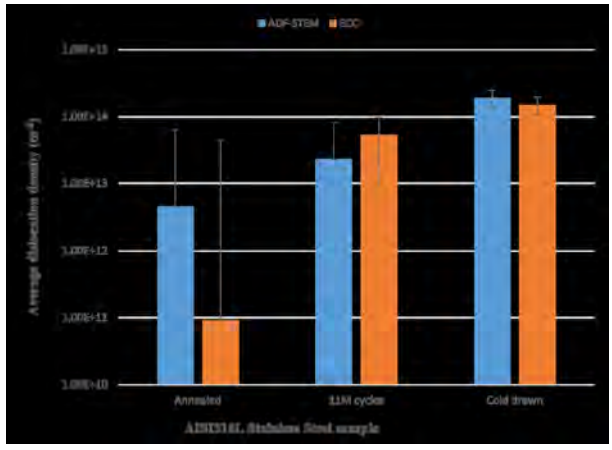

Figure 2. Comparison of the average dislocation density obtained from AISI 316L stainless steel samples, using both ADF-STEM and ECCI.

Corresponding author: s215323548@mandela.ac.za

MICROSTRUCTURE AND TENSILE PROPERTY EVOLUTION IN TEMPERED Ti-6Al-4VxH MARTENSITE

V.N. Vilane[1], R.D. Knutsen[2,3] and J.E. Westraadt[1]

[1]CHRTEM, Department of Physics, Nelson Mandela University, Gqeberha, [2]Centre for Materials Engineering, Department of Mechanical Engineering, University of Cape Town, [3]Electron Microscope Unit, University of Cape Town, Rondebosch

Temporary hydrogen alloying (THA) can refine the microstructure of cast Ti-6Al-4V and enhance mechanical properties. However, THA does not always improve performance, it can also drastically reduce ductility to severe embrittlement due to hydrogen-induced titanium aluminide (Ti_3Al) precipitation[1].This study discusses microstructure and tensile performance evolution in hydrogenated and non-hydrogenated martensite, with particular focus on the effect of Ti_3Al precipitation on tensile performance.

Wrought Ti-6Al-4V rods were converted to simulated cast (Sim. Cast) Ti-6Al-4V by annealing at 1100ºC for 2 hours. Sim. Cast rods were hydrogenated to 20at.%H at 650ºC, solution treated at 900ºC and quenched, tempered for 3 hours at 580ºC, and dehydrogenated (DH) at 675ºC or 750ºC. Control samples were vacuum annealed (VA) at 650ºC, solution treated at 1080ºC, tempered for 3 hours at 580ºC and VA at 675ºC or 750ºC. Hydrogen concentration was confirmed by inert gas fusion and tensile properties were evaluated at room temperature. X-ray diffraction (XRD) using *Co radiation* confirmed bulk constituent phases. Electron backscatter diffraction (EBSD), transmission Kikuchi diffraction (TKD), and Energy Dispersive Spectroscopy (EDS) were performed in the SEM (JEOL 700) and TEM (JEOL 2100 LaB_6) respectively. High angle annular dark field (HAADF) imaging was performed in the JEOL 2100 and the JEOL ARM200F.

Alloying with 20 at.%H lowers the beta transus temperature from 1050ºC to 800ºC, ensuring martensite formation in all samples when quenched from 1080ºC and 900ºC. Fig. 1 highlights a significant increase in yield strength (YS) and a decrease in ductility, attributed to martensite formation. The strength increase, reaching up to 190 MPa, is more pronounced in samples quenched from 1080ºC due to the direct correlation between quenching temperature and strength. Raising the VA temperature from 675ºC (B1) to 750ºC (B2) resulted in a 70 MPa decrease in strength and a 13 % recovery in ductility due to martensite softening. A similar 70 MPa reduction in yield strength was observed in hydrogenated samples (A1, A2), but with a greater ductility recovery of up to 30 %. After accounting for the 13 % recovery, a net 17 % increase in ductility, unique to hydrogenated martensite, remains. This indicates that there are additional factors contributing to embrittlement which are linked to hydrogen-promoted martensite evolution.

Hydrogen alters the transformation pathway, with the presence of orthorhombic martensite (α'') possibly promoting spinodal decomposition[2]. Hydrogenated martensite decomposed to a nanobanded structure consisting of Al-rich, V-rich nanobands where the Al enrichment stabilized Ti_3Al within 3 hours of tempering[2]. Expected Al partitioning occurred in non-hydrogenated samples, but not to the extent of stabilizing Ti_3Al. Figs. (2a-d) show that the nanobanded structure and Ti_3Al were retained after 675ºC and 750ºC dehydrogenation, as confirmed by selected area electron diffraction (SAED) and fast Fourier transform (FFT) analyses at [101] and [012] zone axes. The embrittlement caused by Ti_3Al at 675ºC, was alleviated by increased Ti_3Al dissolution at (750ºC), leading to greater ductility recovery.

References:
1. Vilane, V.N., Knutsen, R.D. and Westraadt, J.E. (2022) Mater. Char. 184, 111698.
2. Vilane, V.N., Knutsen, R.D. and Westraadt, J.E. (2024) Mater. Today Commun. 39, 108826.

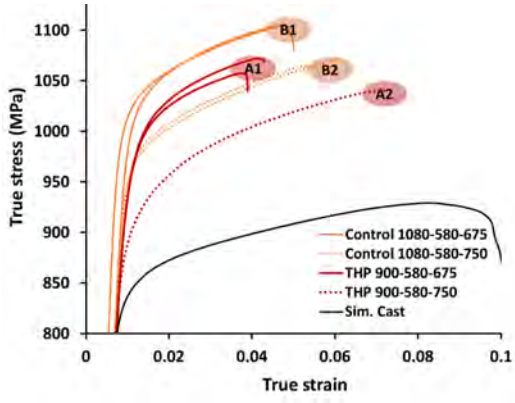

Figure 1. Tensile performance of Sim. Cast and tempered martensite which was DH (A1, A2) or VA (B1, B2) at 675ºC or 750ºC.

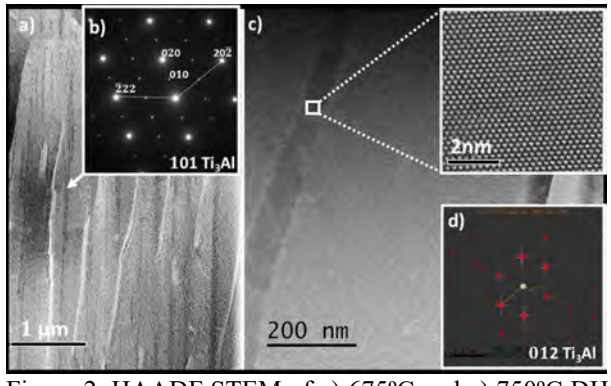

Figure 2. HAADF STEM of a) 675ºC and c) 750ºC DH martensite showing retained Al-rich (dark), V-rich (bright) nanobands and Ti_3Al precipitates confirmed by b) SAED and d) FFT analyses at [101] and [012] zone axes. The Fourier transform in d) was derived from inset c.

Corresponding author: velile.vilane@mandela.ac.za

MICROSTRUCTURE-BASED CREEP LIFE ASSESSMENT OF 1CrMoV TURBINE ROTORS AFTER PROLONGED SERVICE

H.S. Nyembe and J.E. Westraadt

Centre for HRTEM, Department of Physics, Nelson Mandela University, Gqeberha

Some South African thermal power plants rely on aging power-generating rotors made of 1CrMoV steel. While these rotors are creep resistant, prolonged exposure to high temperatures can lead to deterioration in their microstructure and properties due to creep[1]. Surface replication and optical microscopy are commonly used to assess and quantify creep cavities. Then, remaining life assessment (RLA) models are used to predict creep-life exhaustion. However, these models are conservative, resulting in the premature retirement of the rotor[1]. The development of a microstructural-based RLA method is urgently needed to improve the RLA of 1CrMoV rotors. This study aims to evaluate the use of quantitative electron microscopy as a tool for the microstructure-based RLA of 1CrMoV rotor steels that have been in long-term service.

Four 1CrMoV rotors which operated for 270-300 kh were investigated. The core samples (1, 2, 3, and 4) were removed from the highest creep-damaged area in the rotor using the Weldcore® technology. In this area, the operating temperature and stresses are ~538 °C and ~70 MPa. Rotor 1 was sampled at two regions (H3 and H4) that were 180° apart to determine rotor homogeneity. A reference sample (R) was removed from the non-stressed region of the rotor, which experienced the temperature of ±226 °C during operation. All analyses were carried out using a JEOL JSM 7001F SEM. The cavity density (N_A) was quantified from SEM-BSE images. The fractional creep-life exhaustion (t/t_r) was then estimated using the creep cavitation model previously described in reference[1]. The characteristic of the grain structure (particularly PAGs and bainitic laths) was determined using EBSD. From the EBSD data, the volume-weighted average size (d_V) and surface-to-volume ratio (S_V) of bainitic laths were determined.

Table 1 presents the operating times, cavity N_A and corresponding t/t_r, and lath d_V and S_V for each sample. Cavities resulting from creep damage were observed in all core samples. The rotors revealed a duplex grain structure consisting of a mixture of large and small PAGs as shown in figure 1. In rotor 1, there is an inconsistency in the estimated t/t_r due to the non-uniform bainitic lath size. The bainitic lath d_V does not show clear evidence of lath coarsening or refinement due to prolonged exposure to creep. However, there is a good correlation between the average lath d_V and S_V with t/t_r (Fig. 2). Although, it is unclear whether creep exposure or initial grain structure characteristics are responsible for the correlation.

SEM-BSE and EBSD techniques are valuable tools for quantifying cavities and grains in 1CrMoV rotors. However, the heterogeneity of the bainitic lath structure limits the effectiveness of using bainitic laths for microstructure-based life assessment. Further research is needed to establish a more reliable correlation between microstructure and creep-life exhaustion in 1CrMoV rotors.

References:
1. Nyembe, H.S., *et al.* (2024) J. Fail. Anal. and Preven. 24,559

Table 1. Operating time, cavity NA, t/tr, lath dV, and SV.N_A, t/t_r, lath d_V, and S_V.

	T (kh)	N_A (mm^{-2})	t/t_r	d_V (µm)	S_V (µm^{-1})
R	0	0	0	12	0.57
1 (H3)	288.5	345	0.75	6	0.70
1 (H4)		238	0.6	12	0.56
2	272.3	1398	>1	5	0.75
3	300.4	1413	>1	5	0.86
4	273.6	195	0.52	10	0.73

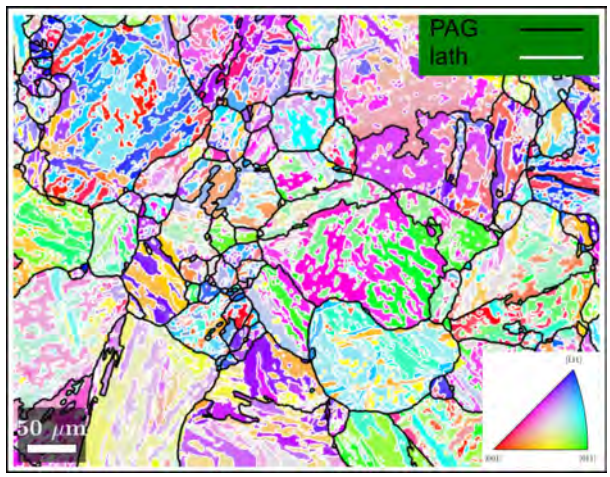

Figure 1. Typical EBSD orientation map showing bainitic laths and PAGs for the rotor.

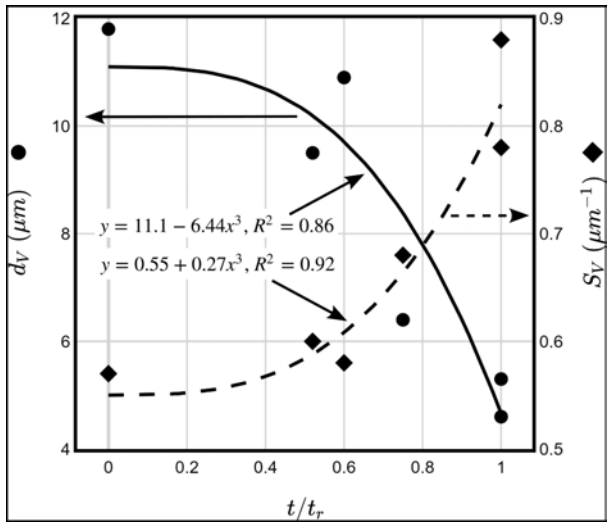

Figure 2. Evolution of lath dV and SV as a function of t/tr.d_V and S_V as a function of t/t_r.

Corresponding author: Johan.Westraadt@gmail.com

PREVENTION OF HYDROGEN PICKUP DUE TO THE CHROMIUM DOPING OF THE ZrO_2 LAYER ON ZIRLO

S. Ngongo[1], A. Janse van Vuuren[1], J.H. Neethling[1] and V. Uglov[2]

[1]Centre for HRTEM, Nelson Mandela University, Gqeberha, [2]Belarusian State University, Minsk, Belarus

Zirconium alloy is the main physical barrier between the coolant system and the fuel cell in the nuclear power plant core[1]. The primary role of the alloy is to keep radioactive fission products contained within the fuel pin[1] during reactor operation. One of the major issues contributing to material failure is due to the possible absorption of hydrogen by the zirconium alloys during reactor operation. The hydrogen diffusion into the zirconium fuel tube has been shown to be responsible for the formation of brittle zirconium hydrides[2]. Theoretical prediction by Youssef and co-workers[3] where they combined statistical thermodynamics and density-functional-theory calculations showed that Cr was the dopant that reduces hydrogen solubility in ZrO_2 at 600 K (i.e. operational temperature) the most when compared to a number of other dopants which are mainly transition elements[3].

In this work compression plasma flow (CPF) was used to produce a chromium-doped, oxidized ZIRLO (which is the commercial zirconium alloy) surface layer. CPF is generated by quasi-stationary plasma accelerators with their own magnetic field. Such plasma flows are characterized by long life-time (about 100 μs) and high energy density absorbed by the target (from 10 to 100 J/cm^2). When CPF interacts with the surface, the top layer is melted and a mixing process takes place in the layer. If a metal coating is deposited on the surface of the treated sample, the CPF impact will provide mixing of both coating and the substrate.

A chromium coating with a thickness of 1 μm was deposited on the oxidized ZIRLO surface. The CPF treatment was done in a nitrogen atmosphere (400 Pa pressure). The chromium alloyed ZIRLO samples were sectioned using a diamond wire saw and mounted on a stub. Surface morphology of the sample was analysed and areas of interest were identified using SEM imaging. A FEI Helios NanoLab FIBSEM was used to cut TEM lamellae from specific areas of interest. The TEM lamellae were investigated in a JEOL 2100 LaB_6 TEM operated at 200 kV.

The TEM results for this investigation indicated that the alloying process of the oxide layer by the CPF method was successful as shown in Figure 1. The thickness of the chromium modified oxide layer was ~ 2 μm. The distribution of chromium in the oxide was observed. Testing of hydrogen pickup was conducted on the modified sample by irradiation of hydrogen at different energies (12.5 keV + 50 keV + 97.5 keV H ions to a dose of 2×10^{17} H ions/cm^{-2}). After irradiation sample was annealed at 500 °C in order for hydrogen to escape the sample. TEM imaging was used to determine the presence of crack formation within the modified oxide layer. The SRIM ranges shown on Figure 2 (a) indicates that the cracks should be formed between ~ (0.1 – 0.6) μm. The TEM image shown in Figure 2 (b) does not reveal crack formation on the modified sample that is due to the hydrogen on the range (0.1 – 0.6) μm as predicted by the SRIM calculations. This is in agreement with the theoretical predictions by Youssef and co-workers[3] where they indicated that doping oxide layer with chromium minimize hydrogen absorption.

References:
1. Kim, H.H. *et al.* (2010) J. Mater. Sci. Technol. 26(9) 827.
2. Motta, A.T., and Chen, L.Q. (2012) *JOM* 64, 1403.
3. Youssef, M. *et al.* (2016) Phys. Rev. Applied. 59(014008).

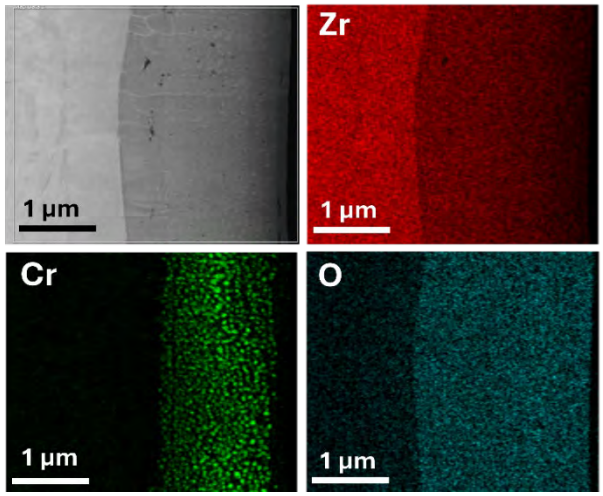

Figure 1. ADF STEM micrograph of a cross section cut from sample with its corresponding EDS results showing the distribution of chromium on the oxide layer

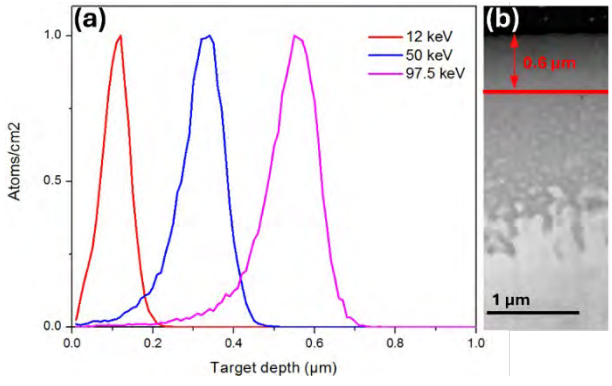

Figure 2. (a) SRIM calculations for the projected ranges of hydrogen ions in ZrO_2 for energies of 12, 50 and 97.5 keV (b) the corresponding TEM image showing where cracks are expected to be observed.

Corresponding author: ngongosamkelo@gmail.com

CORRELATION BETWEEN HOMOGENISATION PARAMETERS AND PROPERTY EVOLUTION OF AA3104 CBS AFTER HOT FINISH ROLLING

K.E. Lebakeng

Centre for Materials Engineering, Department of Mechanical Engineering, University of Cape Town, South Africa

South Africa produces a full-aluminium beverage can using AA3104 aluminium alloy for the can body stock material. This material is locally produced, and optimization of the thermomechanical processing would be beneficial. Process optimisation can be achieved through lab-scale experimentation. Typically, lab-scale research focuses on individual steps within the full process route. AA3104 can body stock production involves direct chill (DC) casting, hot and cold rolling, coiling, and finally forming at the can-maker. A critical stage in this process route is homogenisation, which occurs after DC casting. Homogenisation is critical for the removal of segregation and for critical phase transformations of features, such as intermetallic particles (IMP) and dispersoids. The IMP are critical to maintaining adequate galling resistance during can forming processes of drawing and wall-ironing[1]. Galling resistance is enhanced by optimising the α-phase to β-phase IMP ratio. Dispersoids influence the recovery and recrystallisation kinetics during hot and cold rolling and thus directly affect texture and earing. Earing can be reduced by achieving a more isotropic texture through Particle Stimulated Nucleation (PSN)[2]. PSN associated with IMP during annealing helps nucleate new grains with random orientations. Homogenisation promotes the transformation from β-phase to α-phase, with a higher α to β ratio beneficial for PSN3. Homogenisation introduces sub-micron dispersoids into the matrix, which act to impede grain boundary migration through a Zener drag mechanism. This work aims to assess the effect of three homogenisation practices on the simulated hot rolled mechanical properties and microstructure after exposure to a controlled full lab-scale simulation of the rolling practice, including homogenisation, hot rough rolling and hot finish rolling of AA3104 CBS.

The experimental procedure involved multiple steps guided by industry norms. Firstly, homogenisation and secondly hot rolling of samples. The starting material was extracted from the equiaxed zone of a slice of DC-cast AA3104 ingot, as supplied by industry. A programmable furnace was utilised to homogenise the samples at designated temperatures for the three homogenisation protocols. A summary of the main parameters is shown in Table 1. The homogenized microstructures were characterised using SEM with backscatter imaging and EDS was used to analyse the microstructural composition of the dispersoids. Post homogenisation, the samples underwent a controlled lab-scale hot rough rolling process to breakdown the microstructure following a strain and temperature protocol guided by industry norms. The rolled material was then prepared for plane strain compression (PSC) testing on a Gleeble 3800 to simulate hot finish rolling.

Microstructural characterisation revealed a large variability in microstructural features, namely the size and distribution of IMP and dispersoids. Visual inspection of the SEM (BSE imaging) images of the homogenised samples showed larger dispersoids in the Homog-1 and the IMP display significant spheroidization owing to diffusion. The IMP and dispersoid structures for Homg-1 are shown in Figure 1. Homog-2 and Homog-3 samples retain the interconnected IMP structures, but display smaller dispersoid sizes. The size, morphology and presence of both IMP phases must be characterized to assess the extent of the β-phase to α-phase transformation for all practices, but preliminary results indicate that temperatures of over 560 °C are required for this transformation.

Preliminary results indicate that extended homogenisation at elevated temperatures leads to larger dispersoids and spheroidised IMP structures owing to the increased progression of diffusion of silicon, manganese and iron. The impact of the homogenized structures on the flow stress during plane strain compression is not evident, but this does not negate the effect on the microstructural development. Further conclusions will be drawn upon the collection of additional data relating to the final texture after post deformation recrystallisation annealing.

References:
1. Wycliffe, P et al. (1999) Patent US5913989A.
2. Smith, C.S. (2010) Metall Mater Trans A 41(5), 15.
3. Králík, R. et al. (2021) Applied Physics of Condensed Matter. Slovak Republic.

Table 1. Homogenisation Experiment Matrix

Protocol	Main temperature	Time range
Homogenisation 1	600 °C	4-8 hours
Homogenisation 2	560 °C	4-8 hours
Homogenisation 3	520 °C	4-8 hours

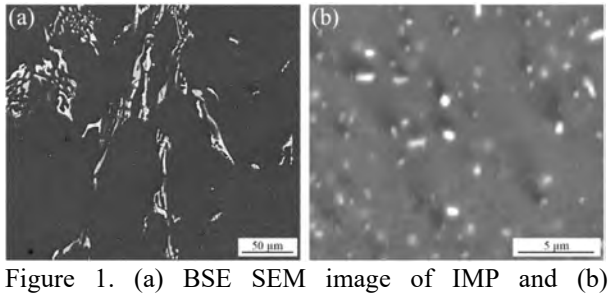

Figure 1. (a) BSE SEM image of IMP and (b) dispersoid structures in Homog-1 sample.

Corresponding author: lbkkhe001@myuct.ac.za

PRINTABILITY AND PROPERTIES OF WC-12Co/Mo CEMENTED CARBIDE USING DIRECT INK WRITING

N.P. Mphasha[1], R.M. Genga[2,3], C. Polese[3,4], N. Sacks[5], J. Vleugels[6], S. Huang[6] and S. Ngongo[7]

[1]School of Chemical and Metallurgical Engineering,, University of the Witwatersrand, Johannesburg, [2]Academic Development Unit, University of the Witwatersrand, Johannesburg, [3]School of Mechanical, Industrial and Aeronautical Engineering, University of the Witwatersrand, Johannesburg, [4]4ARUA Centre of Excellence in Materials, Energy and Nanotechnology, University of the Witwatersrand, Johannesburg, [5]Department of Industrial Engineering, Stellenbosch University, Stellenbosch, [6]Department of Materials Engineering, KU Leuven, Belgium, [7]Centre for HRTEM, Nelson Mandela University

Tungsten carbide-cobalt (WC-Co) cemented carbides are extensively used in applications requiring a good combination of high wear resistance, hardness, and toughness, making them ideal for applications in cutting mining and drilling operations[1]. However, conventional manufacturing techniques, such as liquid phase sintering, have limitations in terms of design flexibility and material efficiency. To overcome these limitations, direct ink writing (DIW), also known as robocasting, has emerged as a promising additive manufacturing technique for fabricating complex geometries with tailored properties[2] comparable to conventional sintering. This study explores the printability and properties of WC-12Co/Mo cemented carbides fabricated via DIW, focusing on the influence of material formulation, processing parameters, and the resultant microstructure and mechanical properties.

Printability, microstructure and properties of WC-12Co/Mo cemented carbides prepared using varying slurry (ink) solids loading (62.8 – 64.8 vol%) were investigated. Sintered samples were characterized by optical and scanning electron microscopy. Figure 1 shows delamination and cracking at the uppermost layers due to insufficient overlapping and suboptimal drying conditions. Increasing the solid loading (64.8 vol%) minimized the formation of cracks and pores (Figure 2). Smaller WC grains dissolved in the Co-based binder phase and re-precipitated on larger WC grains, resulting in larger WC grains with a slight rounding of edges (Figure 2). The rounding of WC grain edges can be ascribed to the dissolution of Mo into both the WC grains and the binder phase. Samples showed a random WC grain orientation with a less pronounced texture due to uniform cooling and the absence of strong directional solidification.

Microstructure evolution revealed that increasing the solid loading improved particle packing, thus enhancing the density and hardness. This is despite the anisotropy in mechanical properties as shown in Table 1. The reduction in microcracking can be ascribed to better bonding between layers which minimized the effect of drying conditions. However, several challenges remain in the DIW of WC-12Co/Mo cemented carbides. Optimization of slurry formulation is critical, as variations in particle size distribution and solvent ratio can significantly affect the printability and resultant properties of the components. Moreover, the drying process should be precisely controlled to avoid oxidation and cracking, which compromises the material's performance.

References:
1. Upadhyaya, G.S. (1998) Cemented Tungsten Carbide Production, Properties and Testing. USA, Noyes Publications
2. Bose et al. (2024) Int. J. Refract. Met. Hard Mater. 119, 106493

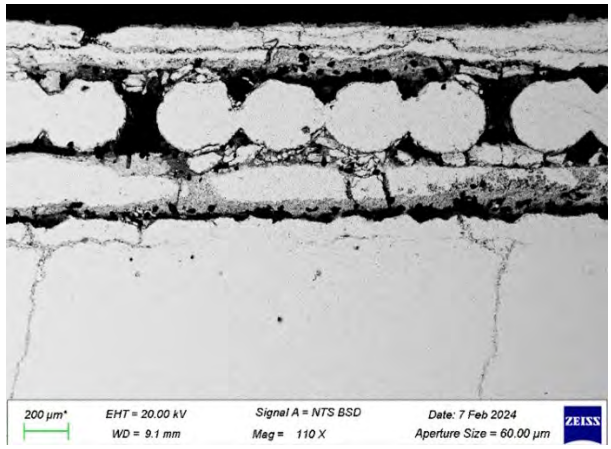

Figure 1. SEM-BSD image of WC-12Co/Mo (62.8 vol% solid loading), showing cracking, delamination and pores.

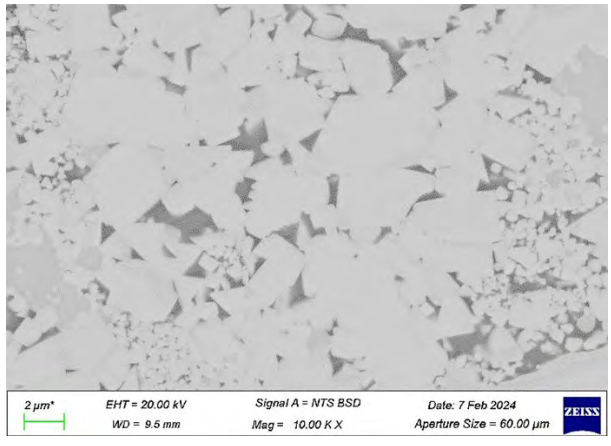

Figure 2. SEM-BSD image of WC-12Co/Mo (64.8 vol% solid loading), showing slightly rounded WC (light) edges and Co-based binder (dark).

Table 1. Properties of WC-12Co/Mo fabricated by DIW

Solid loading (vol%)	Densification (%)	Hardness (HV_{30})
62.8	90.83	1001±54
63.5	91.25	1061±51
64.1	91.79	1110±42
64.8	93.01	1094±20

Corresponding author: nthape.mphasha@wits.ac.za

ENERGY CONSUMPTION OF NBC BASED INSERTS DURING FACE MILLING OF AUTOMOTIVE GCI

M.S. Rabothata[1,2], R.M. Genga[1,2,3], N.P. Mphasha[4], K. Phaka[2], C. Polese[2,3], P. Zeman[5], S. Huang[6], J. Vleugels[6] and S. Ngongo[7]

[1]Academic Development Unit, [2]School of Mechanical, Industrial and Aeronautical Engineering, University of Witwatersrand, [3]DSI-NRF Centre of Excellence in Strong Materials, [4]School of Chemical and Metallurgical Engineering, University of Witwatersrand, [5]Materials Research Centre of Manufacturing Technology, Czech Technical University in Prague, Czech Republic, [6]Department of Materials Engineering, KU Leuven, [7]CHRTEM, Nelson Mandela University, South Africa

Over the past decade, South Africa has struggled with significant energy generation and supply challenges, leading the country's power utility to implement various stages of load shedding. In 2023, the situation reached a record low, making it the worst year to date. This energy crisis has caused serious harm to the manufacturing industry. Hence, the effects of femtosecond (f) laser surface modification (LSM) and molybdenum (Mo), titanium carbide (TiC), and Mo plus TiC additions as secondary hardening phases and grain growth inhibitors on the energy consumption and machining performance of niobium carbide (NbC)-based cermets during dry face-milling of automotive grey cast iron (a-GCI) were investigated in this study.

An LD50C femtosecond laser was used to create shark skin (S) and pyramid (P) micro textures (patterns) on the cutting edges of inserts with compositions NbC-12Ni (wt.%) (N2S), NbC-12[Ni/Mo] (wt.%) (N2MS), NbC-10TiC-12Ni (wt.%) (R2S), and NbC-10TiC-12[Ni/Mo] (wt.%) (R2MS) produced by pulsed electric current sintering (PECS). During the dry face-milling of a-GCI, the feed (f) was 0.1 mm/tooth, the cutting speed (v_c) was 200 /min, the depth of cut (a_p) was 1 mm, and the spindle speed was 800 rpm. The machining forces were measured using a Kistler force dynamometer, and the crater and flank wear were evaluated by optical microscopy, scanning electron microscopy (SEM), and high-angular annular dark-field (HAADF)-scanning transmission electron microscopy (STEM). Regardless of composition, Mo fully dissolved during sintering and was detected to be inside the carbide phases of samples by HAADF- STEM. In contrast, TiC did not fully dissolve in both R2S and R2MS, as shown by the EDS mapping in Figure 1. The undissolved TiC has been reported to enhance the hardness and abrasion wear resistance of cutting inserts, improving the performance of inserts during machining[1].

The P-R2MS insert had the lowest energy consumption (U_c) (22.07 J/mm^3), while its shark skin counterpart S-R2MS exhibited the highest U_c compared to all the other inserts. In general, the P-microtextured cutting inserts had relatively lower energy consumption than the S-microtextured inserts. This was attributed to the entrapment of relatively higher volumes of chips on the S-microtextured inserts during machining, which increased the cutting forces that are directly proportional to energy consumption. Figure 2 shows optical images of the flank and rake faces of P-R2MS and S-R2MS inserts after 20 minutes of dry face-milling. The main wear mechanisms of cutting inserts during a-GCI machining were characterized by abrasion wear, attrition wear, and mechanical fracture. All the cutting inserts, apart from S-N2MS, achieved the maximum insert tool life of 20 minutes. This exceptional performance was attributed to the S- and P-microtextures by the f-LSM technique, which improved the hardness, strengthened the cutting edges of the inserts, and enhanced abrasion wear resistance[1].

References:
1. Genga et al. (2019), Int. J. Refract. Met & Hard Mat, 86.

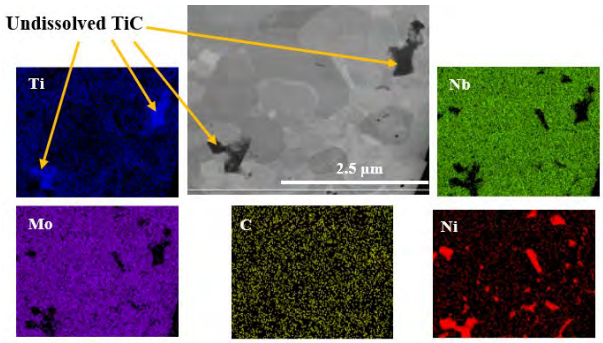

Figure 1. HAADF-STEM image and EDS maps of NbC-10TiC-12[Ni/Mo] (R2MS).sample. showing: Nb (green), Ni (red), Mo (purple), C (yellow), and Ti (blue).

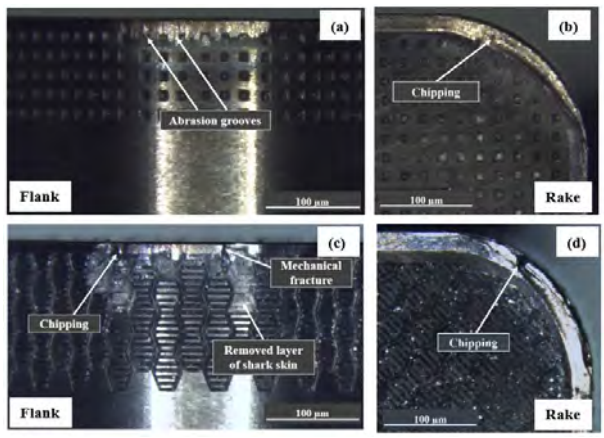

Figure 2. Optical images of (a) flank (b) rake faces of P-R2MS insert, and (c) flank and (d) rake faces of S-R2MS

Corresponding author: Mahlatse.Rabothata@wits.ac.za

CIRCULAR MANUFACTURING OF FE AND DUPLEX STEEL-BONDED WC HARDMETALS FOR AEROSPACE-GRADE AA7010-T7651 FACE-MILLING

R.M. Genga[1,2,3], N.P. Mphasha[2,4], T. Nhlanhla[3], G. Peters[5], D.E.P. Klenam[2,4], M.O. Bodunrin[2,4], T. Steenkamp[6], C. Polese[2,3] and A. Janse van Vuuren[7]

[1]Academic Development Unit (ADU), University of the Witwatersrand, [2]DST-NRF Centre of Excellence in Strong Materials, hosted by the University of the Witwatersrand, [3]School of Mechanical, Industrial and Aeronautical Engineering, University of the Witwatersrand, [4]School of Chemical and Metallurgical Engineering, University of the Witwatersrand, [5]School of Physics, University of the Witwatersrand, [6]Pilot Tools (Pty) Ltd., South Africa, [7]CHRTEM, Physics Department, Nelson Mandela University, Gqeberha

The manufacturing sector significantly contributes to global greenhouse gas emissions, accounting for approximately 24% as of 2020[1]. Circular manufacturing (CM), which emphasizes waste reduction and resource optimization, is essential for creating sustainable industries in the 21st century. Hardmetals, commonly used in manufacturing, depend on critical raw materials like tungsten carbide (WC) and cobalt (Co), but sustainable alternatives are emerging. Using iron (Fe) or iron alloys as binders instead of Co can enhance hardmetal recyclability, reduce environmental impact, and lower costs. This study compares Fe and SAF2205 duplex steel-bonded WC hardmetals, with titanium carbide (TiC) additions, to conventional WC-Co in terms of their physical, structural, and mechanical properties.

WC-Co, WC-Fe, and WC-duplex steel-based (SAF2205) samples were successfully produced by liquid phase sintering (LPS). Cutting inserts manufactured from these samples were used for face-milling of aerospace-grade AA7010-T7651 at cutting speeds (v_c) of 300–600 m/min and depths of cut (a_p) of 0.5–1.0 mm. Insert performance was assessed on tool life and cutting force. Insert wear was characterized using optical microscopy, scanning electron microscopy (SEM), and annular dark field (ADF) scanning transmission electron microscopy (STEM).

In the WC-TiC-Fe/SAF2205 samples, Fe and SAF2205 duplex steel binders were primarily located between the WC grains rather than around the TiC grains, as confirmed by ADF-STEM mapping (Fig. 1). Undissolved TiC was also present, contributing to increased hardness and abrasion resistance. However, the uneven binder distribution in the WC-TiC-Fe/SAF2205 samples resulted in reduced fracture toughness (K_{IC}) compared to conventional WC-Co.

During semi-finishing (v_c = 300 m/min, a_p = 1.0 mm), the WC-TiC-SAF2205 (WC-4TiC-12Fe (DS)) and WC-Fe-based inserts exhibited similar flank wear rates (5.28 µm/min and 5.22 µm/min, respectively) to WC-Co-based insert (5.00 µm/min). Adding TiC to the SAF2205-bonded inserts improved tool life by ~100%. While the WC-Fe-based inserts performed well, wear was still visible on the cutting edges. For example, Figure 2 presents the ADF-STEM map of the Fe-bonded WC insert (WC-12Fe (wt%)) at the cutting edge/workpiece interface, showing fractures on the cutting edge, likely due to abrasive wear. Additionally, exposed binder was observed, suggesting WC grain pull-out due to adhesive wear. Similarly, during finishing (v_c = 600 m/min, a_p = 0.5 mm), the WC-Co-based inserts had the lowest flank wear rates. However, the addition of TiC to both SAF2205 (DS) and Fe-bonded inserts significantly improved the tool life by ~300%. Thus, although Fe-bonded WC inserts generally outperformed SAF2205-bonded inserts, the alternative ferrous binders demonstrated comparable performance to WC-Co inserts, highlighting their potential as sustainable substitutes.

References:
1. Ritchie H (2024) Our World in Data
2. Genga R.M. *et al.* (2020) Int. J. Refract. Met. Hard. Mater., 86, 105128.

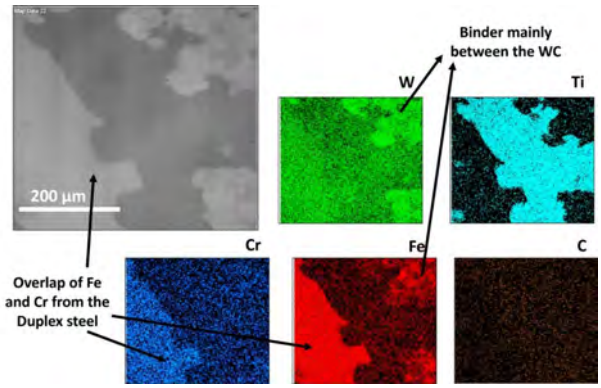

Figure 1. ADF-STEM mapping images of WC-TiC-12SAF2205 wt% sample, showing: WC (green), Ti (light blue), Cr (dark blue), Fe (red), and C (brown)

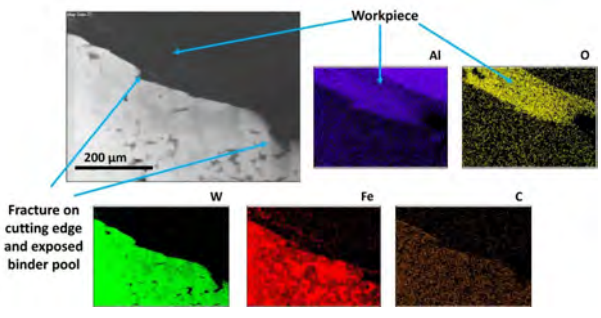

Figure 2. ADF-STEM mapping images of WC-12Fe (wt%) sample, showing: Al (purple), O (yellow), WC (green), Fe (red), and C (brown)

Corresponding author: Rodney.Genga@wits.ac.za

INVESTIGATION OF 1D $BATIO_3/CD_{0.5}ZN_{0.5}S$ HETEROSTRUCTURE FOR PIEZO-PHOTOCATALYTIC REMOVAL ORGANIC POLLUTANTS

T.T. Mohlala[1], T.L. Yusuf[2], M. Masukume[3], V. Ojijo[3] and N. Mabuba[4]

[1]Chemical Sciences, University of Johannesburg, Johannesburg, [2]Dept. Of Chemistry, University of Pretoria, Pretoria, [3]Chemical Engineering, CSIR, Pretoria Campus, [4]Centre for Nanomaterial Science Research, University of Johannesburg, Johannesburg

Understanding and controlling the morphology of semiconductors and piezoelectric nanostructures is crucial for optimizing their performance in various applications, from water purification to energy production. Piezoelectric semiconductors are used for the remediation of water via piezo and piezo-photocatalysis as a form of water treatment of organic contaminants[1,2]. An S-scheme n-n heterojunction between $BaTiO_3$ and CdZnS was fabricated for oxidation of CIP in synthetic and real waste water.

The $BaTiO_3/Cd_{0.5}Zn_{0.5}S$ was synthesized via solvothermal deposition of $Cd_{0.5}Zn_{0.5}S$ (CZS) onto $BaTiO_3$ (BTO) nanorods[3]. Three ratios were prepared: 25%CZS, 50% CZS, and 100% CZS (1:1), and among them, the heterojunction that exhibited superior photocatalytic activity was the 1:1 ratio. The ratio was characterized using electrochemical techniques to determine its superiority over the other ratios. BET was also used for the evaluation of surface properties, XPS for charge transfer properties, PL for electron lifetime, XRD for crystallography, DRS for optical properties, and SEM and TEM for morphology. Based on its crystallographic properties, BTO is cubic, while CZS has exhibited hexagonal crystal structures.

The 1:1 ratio was used for piezo-photocatalytic degradation of CIP for 90 minutes using ultrasonication power of 20 W and a visible lamp of 70 W. Degrdataion effeciency was calculated to be ~83% using the UV-Vis. The extent of mineralization reached 46.7% analyzed when analyzed using the TOC, and intermediate products were evaluated using UPLC-MS, with their toxicity assessed using the Toxicity Estimation Software Tool (T.E.S.T). A catalyst stability study was condyuted with 4 cycles of dradation reaching maximum removal of 71%. Scavenger studies identified h^+, $\bullet O_2^-$, and $^{\bullet}OH$ as the major reactive species responsible and pH studies highlighted the best pH conditions for CIP degradation to be in the neutral to basic conditions[3].

The CZS exhibited both photocatalytic and piezoelectric properties due to its 1-D structure, while BTO showed relatively good piezoelectric properties because of its non-centrosymmetric nature[4]. The synergy between these two nanostructures was observed through the piezo-photocurrent transient light response studies, indicating enhanced visible light-induced charge carriers. The S-scheme arrangement, together with the piezo-photocatalytic process, allowed the conservation of enough holes and electrons for the generation of oxidants for the CIP degradation using 1.0BTO/CZS, hence its impressive degradation and stability in comparison to its induvial counterparts.

References:
1. Yadav, D., *et al.* (2023) J. Mater. Sci. 58(26), 10576
2. Zhang, J., Wang, C., and Bowen, C. (2014) Nanoscale 6(22) 13314
3. Liu, Y., *et al.* (2025) J. Colloid Interface Sci. 678, 657
4. Liu, Y., *et al.* (2024) Chem. Eng. J. 488, 150768

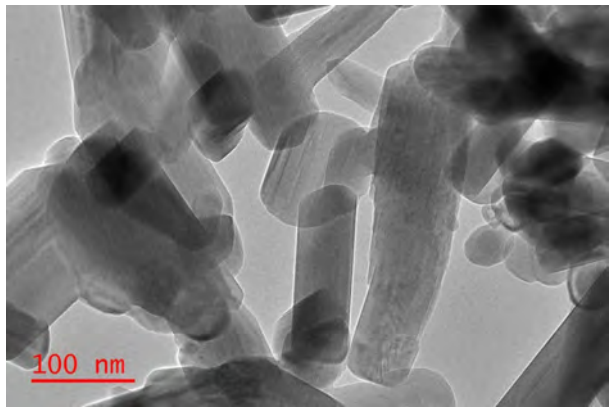

Figure 1. TEM Micrograph of BTO

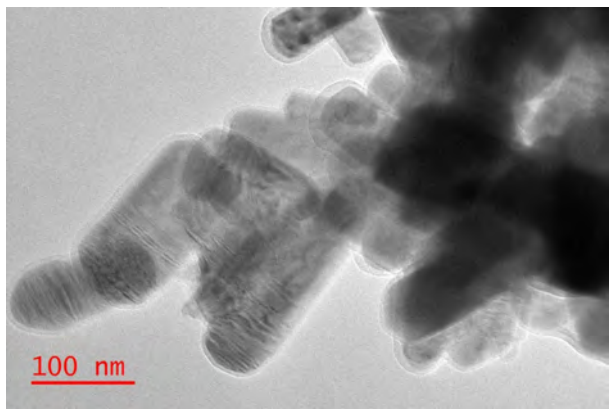

Figure 2. TEM Micrograph of CZS

Corresponding author: nmabuba@uj.ac.za

ESTABLISHING THE CO-EXISTENCE OF METAL OXIDES IN NANOSTRUCTURED COBALT OXIDE-BASED GAS SENSORS.

R. Makole, H.C. Swart and D.E. Motaung

Physics Department, University of the Free State

The application of various semiconductor metal oxides (SMOs) as potential gas sensor materials has received a lot of interest in the past and continues to do so, mainly due to their distinct properties. The simplified production of gas sensor material with nano-size structures, catalytic activity, tunable resistance, and the oxide state of SMOs are among some of the properties that make them attractive for gas sensing[1, 2].

Tricobalt tetraoxide (Co_3O_4) is one of the SMOs that has been widely reported to exhibit excellent sensitivity to numerous volatile organic compounds[3]. However, factors such as sensor instability and poor signal reproduction are still persistent challenges. The incorporation of two or more SMOs to form one sensor material has been reported to be one of the effective ways of improving sensor sensitivity and stability[4].
This work presents a facile method of fabricating higly sensitive and stable gas sensor materials comprising of Co_3O_4 and other n-type SMOs; Co_3O_4-In_2O_3, Co_3O_4-CeO_2, Co_3O_4-SnO_2, and Co_3O_4-ZrO_2. The co-existence of the SMOs were established by the X-ray powder diffraction (XRPD) and further corroborated by the high-resolution transmission electron microscopy (HR-TEM). The selected area electron diffraction (SAED) patterns shown in Fig. 1 shows the presence of cobalt oxide, denoted by the "Co" indexed pattern and indium oxide denoted by "In" indexed pattern, which establishes the formation of a p-n heterostructure of Co_3O_4-In_2O_3. The high-angle annular dark-field scanning transmission electron microscopy (STEM-HAADF) analysis also confirmed the formation of heterostructure or the incorporation of numerous n-type SMOs on the Co_3O_4 surface. From the TEM overview image analysis, shown in Figure 2, nanorod morphology of the Co_3O_4-In_2O_3 heterostructure was witnessed. In addition, the surface morphology micrographs of the synthesized samples showed a mixture of thick Co_3O_4 nanorods covered with nanoparticles, and thin nanorods.

For application, the Co_3O_4-n-type SMO sensors were tested for reducing gases (benzene, toluene, ethylbenzene, xylene (BTEX), acetone), and oxidizing gas (NO_2). The Co_3O_4-In_2O_3 heterostructure demonstrated a remarkable sensitivity, selectivity, and response of 36.6 towards 100 ppm xylene, as well as a low limit of detection of 200 ppb at an optimal operational temperature of 150 ˚C. The improvement in the sensing performance was due to the facilitated adsorption of oxygen on the surface, which led to an increase in the oxidation effect of xylene vapors by Co_3O_4. Furthermore, the performance was related to the high surface area, mesoporous behavior, and large pore volume that provided multiple strong redox reactions sites, as well as the synergistic combination of Co_3O_4 and In_2O_3 in the nanoscale p-n heterojunction.

References:
1. Oprea, A. *et al*. (2018), Gas Sensors Based on Conducting Metal Oxides: Basic Understanding, Technology and Applications. Elsevier Inc.
2. Korotcenkov, G. (2007) Mater. Sci. Eng. B Solid-State Mater. Adv. Technol.139(1), 1.
3. Cao, J. *et al*. (2020) Sens. Act., B Chem., 315, 128120.
4. Joon, J.W. *et al*.(2014) Sens. Act., B Chem., 202, 263.

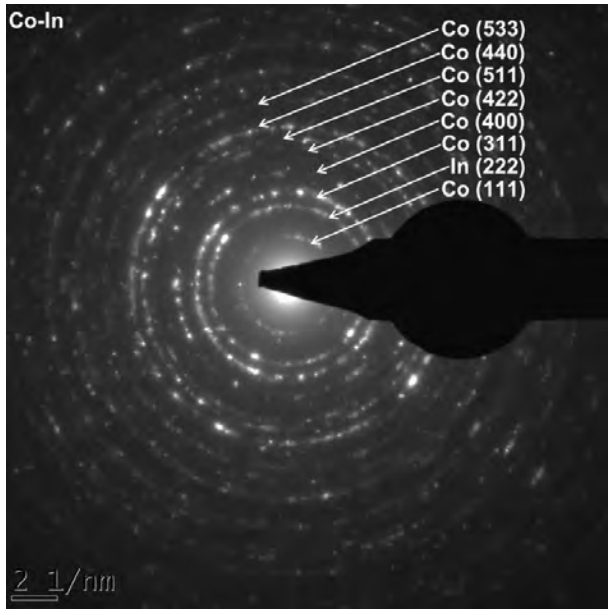

Figure 1. SAED pattern of the Co_3O_4-In_2O_3 heterostructures.

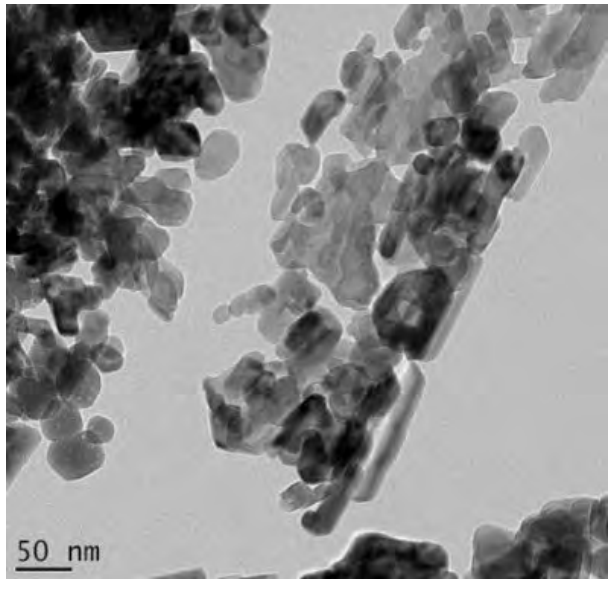

Figure 2. TEM overview image of the p-n Co_3O_4-In_2O_3 heterostructures.

Corresponding author: Makole.R@ufs.ac.za

IMPACT OF USING CAPPING LIGANDS ON THE EMULSION-LARP SYNTHESIS OF CESIUM LEAD BROMIDE NANOCRYSTALS

G.B. Nair, S. Tamboli and H.C. Swart

Department of Physics, University of the Free State, P. O. Box 339, Bloemfontein, 9300, South Africa

Understanding the growth dynamics of $CsPbX_3$ (X = Cl, Br, or I) perovskite nanoparticles is important for tailoring the shape and dimensions of the nanocrystals (NCs) essentially suited to optimize the optical properties, enhancing the stability and improving the performance of perovskite-based devices. Although the hot-injection method was the foremost technique to be employed for the synthesis of perovskite nanocrystals, their inability to scale-up the synthesis paved the way for other novel synthesis techniques such as ligand-assisted reprecipitation (LARP), emulsion-LARP, reverse microemulsion, sonication, low-temperature strategy, polar-solvent controlled ionization, and solvothermal methods[1].

The emulsion-LARP method offers the advantage of a facile synthesis along with the feasibility of scaling-up the process. Moreover, it has better control over the morphology and dimensions of the NCs than the conventional LARP method[2]. However, there is a need to identify the role of the capping ligands in controlling the growth dynamics of the NCs and their subsequent impact on the optical properties of the NCs. In this study, $CsPbBr_3$ NCs were prepared by the emulsion-LARP method, which is described elsewhere[2]. Four different cases were studied to identify the role of ligands on the NCs. In the first case, the NCs were prepared with the addition of oleic acid (OA) and oleylamine (OLA). In the second case, only OA was added to the precursor solution, whereas in the third case, only OLA was added for the preparation of the $CsPbBr_3$ nanoparticles. In the fourth case, both OA and OLA were avoided during the synthesis.

In the first two cases, the NCs crystallized into a pure orthorhombic phase. However, the third and fourth cases resulted in the formation of mixed phases with a dominant orthorhombic phase of $CsPbBr_3$.This suggests that the presence of OA is vital for achieving a pure orthorhombic phase of $CsPbBr_3$, while OLA is not critical for the formation of a pure perovskite phase.

The presence of OA and OLA also decided the morphology and dimensions of the particles formed during the synthesis, as shown in Figure 1. The best results were observed when both OA and OLA were introduced during the synthesis. In this case, nanoplatelets of $CsPBBr_3$ NCs were formed whose dimensions were less than 20 nm. However, the perovskites formed with larger ellipsoidal shapes when OA was solely added during the synthesis. When only OLA was used, the nanoparticles were found to form clusters of several multi-shaped particles. In the absence of both OA and OLA, $CsPbBr_3$ formed bulk spheres and were no longer in their nano-form. As shown in Figure 2(a), the NCs prepared using both OA and OLA showed a d-spacing value of 2.9 Å, which corresponds to the x-ray diffraction from the (2 0 2) plane of orthorhombic $CsPbBr_3$ NCs. The major reflections observed in the X-ray diffraction pattern can be correlated with the planes indexed on the SAED pattern, shown in Figure 2 (b). From the optical and photoluminescence characterizations, the NCs prepared with both OA and OLA were found to show the optimized properties and they exhibited far better absorption and emission properties than the other three samples.

The results suggest that both OA and OLA are essential for obtaining high-quality $CsPbBr_3$ NCs with a pure orthorhombic phase for achieving desirable optical properties and optimized performance in optoelectronic devices.

References:
1. Shamsi, J., *et al*. (2019) Chem. Rev. 119(5), 3296–3348.
2. Nair, G.B., *et al*. (2022) J. Alloys Compd. 928, 167249.

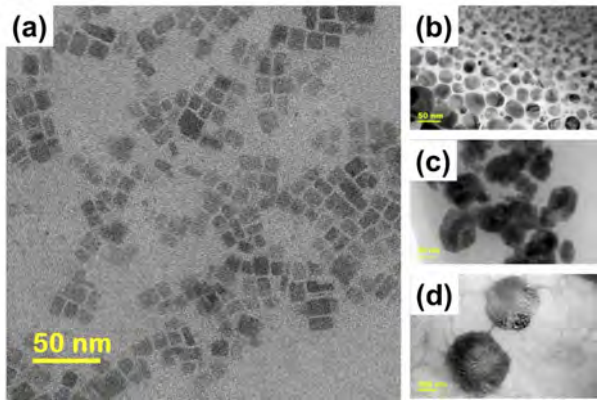

Figure 1. HR-TEM images of $CsPbBr_3$ nanoparticles prepared by emulsion-LARP method: (a) with both OA and OLA, (b) with only OA, (c) with only OLA, and (d) without OA and OLA.

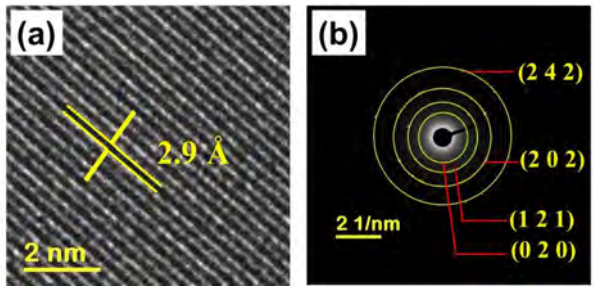

Figure 2. (a) Determination of the d-spacing from the HR-TEM image of $CsPbBr_3$ nanocrystals prepared using OA and OLA. (b) Corresponding SAED pattern and the indexation of the diffraction rings

Corresponding author: nair.gb@ufs.ac.za

COMPETITIVE ADSORPTION OF CADMIUM AND MERCURY FROM WATER BY AgNP-NATURAL RUBBER/POLYVINYL ALCOHOL NANOFIBRE COMPOSITE

L.B Osei, S. Fosu and S.A. Ndur

Environmental and Safety Engingeering Department, University of Mines and Technology, Tarkwa, Ghana

Silver nanoparticles (AgNP) play an important role in wastewater treatment[1]. In single-component adsorption studies, heavy metals such as cadmium (Cd^{2+}) and mercury (Hg) have been successfully removed from water by AgNP in electrospun natural rubber/polyvinyl alcohol nanofibre composites (AgNP-PVA/NRL)[2,3]. Though these AgNP-PVA/NRL efficiently removed Cd^{2+} and Hg in single-component adsorption studies, the level of interference of one metal on the other has not been assessed. Hence, in this study, the efficiency of AgNP-PVA/NRL in removing Cd^{2+} and Hg in a competitive adsorption study was investigated.

The AgNP in electrospun AgNP-PVA/NRL were synthesised utilising silver nitrate ($AgNO_3$) concentrations of 0.01 M and 0.015 M, named 0.01 M AgNP (Fig. 1) and 0.015 M AgNP, respectively[2]. SEM, EDX, TEM and XRD techniques were employed to observe and confirm the presence of AgNP in the nanofibre composite. Other AgNP-PVA/NRL were produced and named Mix 1 (via concurrent electrospinning of 0.01 M AgNP and 0.015 M AgNP) and Mix 2 (via sequential electrospinning of 0.01 M AgNP and 0.015 M AgNP). Mix 3 consisted of separate sheets of 0.01 M AgNP and 0.015 M AgNP applied in the same aqueous solution for adsorption. The nanofibre composites 0.01 M AgNP, 0.015 M AgNP, Mix 1, Mix 2 and Mix 3 were placed in Cd-Hg solutions for the competitive adsorption studies.

The AgNP-PVA/NRL nanofibre composites adsorbed maximum Hg from the Cd-Hg solution in the order: 0.015 M AgNP < 0.01 M AgNP < Mix 2 < Mix 1 < Mix 3. On the other hand, maximum Cd^{2+} removed was in the order: 0.01 M AgNP < Mix 2 < Mix 1 < Mix 3 < 0.015 M AgNP. Per cent removal of Hg by 0.01 M AgNP in the adsorption study reduced by ~20% (from 5.6637 mg/g to 4.3719 mg/g, representing about 89% to 69%) and ~26% (from 11.8747 mg/g to 8.2398 mg, representing ~ 93% to 68%) for Cd^{2+} as compared to the single-component adsorption study. Contrarily, the removal efficiency of 0.015 M AgNP reduced by ~25% (that is, 3.7758 mg/g to 2.7279 mg/g, representing ~ 89% to 64%) for Hg and ~17% (that is, 7.9588 mg/g to 6.2779 mg/g, representing ~ 93% to 77%) for Cd^{2+} adsorption as compared to the single component adsorption study.

Similar to single-component adsorption studies, 0.01 M AgNP adsorbed a higher percentage of Hg than Cd^{2+}, whilst 0.015 M adsorbed a higher percentage of Cd^{2+} than Hg[2,3]. A relatively higher removal efficiency of Hg by 0.01 M AgNP may be attributed to the larger AgNPs formed on the surface of the nanofibre composite. On the other hand, the relatively higher removal efficiency of Cd^{2+} by 0.015 M AgNP may be attributed to Cd^{2+}'s smaller density and atomic radius (calculated), enabling Cd^{2+} to infiltrate the fibre relatively easily and be adsorbed by AgNP within the fibre. Reduction in removal efficiencies for 0.01M and 0.015 M AgNP was likely due to Hg and Cd^{2+} competing for the same adsorptive sites.

Nanofibres Mix 1 and Mix 2 had similar removal efficiencies for Hg (Mix 1: 79.90%, 2.0338 mg/g; Mix 2: 79.80%, 2.0313 mg/g) and Cd^{2+} (Mix 1: 61.88%, 3.0118 mg/g; Mix 2: 61.52%, 2.6548 mg/g). For both, there was a relatively small increase in Hg adsorption, whilst that of Cd^{2+} decreased. This may be due to the doubled amount of electrospun solution, increasing the number of fibres per area. The increased number of fibres masked others and possibly affected other fibres. Hence, Hg was adsorbed better due to adsorption occurring mainly on the surface, whilst Cd^{2+} adsorption mostly occurred within the fibres. This showed that the mode of synthesis did not significantly affect the removal efficiencies for Cd^{2+} and Hg.

Therefore, this work has shown that AgNP-PVA/NRL nanofibre composites can efficiently adsorb Hg and Cd^{2+} in a competitive adsorption system but with reduced efficiencies.

References:
1. Al-Qahtani, K.M. (2017) Egypt. J. Aquat. Res. 43(4), 269-74
2. Osei, L.B., Fosu, S. and Ndur, S.A. (2023) Int. J. Environ. Sci. Technol. 21(4), 4223-38
3. Osei, L.B., Fosu, S. and Ndur, S.A. (2023) Ghana Min. J. 23(1), 11-21

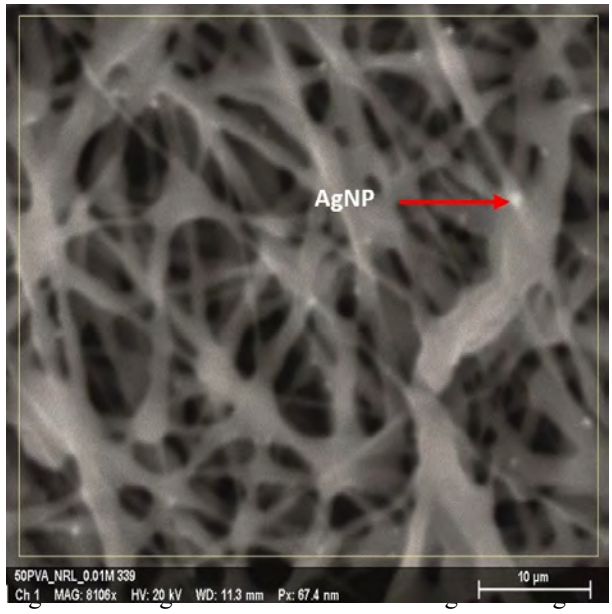

PVA/NRL nanofibre composite

Corresponding author: lbosei@umat.edu.gh

ENCAPSULATION OF Eu-Si QDs IN ZEOLITIC IMIDAZOLE FRAMEWORK-8 (ZIF-8) FOR PHOTOLUMINESCENCE TUNING

S.J. Panchu, S.E. Punchu, M M Duvenhage and H C Swart

University of the Free State, Bloemfontein, South Africa

Among the emerging optoelectronic devices, colloidal quantum dots (QDs) have significant potential for both absorption and emission of light. The QDs are semiconductor nanocrystals with sizes between 2 and 10 nm. The unique tunability and size-dependence of their electronic properties have raised considerable interest in them in the past two decades, making them useful for biological, analytical, medical and engineering applications[1–4]. Solid-state thin films are not widely used due to their unfavourable charge and energy transfer mechanisms[5]. In this work silicon quantum dots (Si QDs) encapsulated with various concentrations of europium (Eu) in ZIF-8 (EZIF-8) have been developed. Selecting suitable nano-units that can act as building blocks for constructing metal organic frameworks (MOFs) and in addition serve as ideal carriers for fluorescent materials to maintain their intrinsic fluorescent properties has become a crucial challenge.

In this study, Si QDs with size of 1-10 nm (Figure 1 (b) and (c)) embedded in ZIF-8 (SiQDs@ZIF-8) nanoparticles with different particle sizes were prepared, and SiQDs@ZIF-8 based MOFs were successfully fabricated via room temperature chemical synthesis under stirring condition for 24h using zinc nitrate and 2-methylimidazole as an organic linker with Si QDs. The europium nitrate was added during the process for the formation of Eu-ZIF-8 and SiQDs@Eu-ZIF-8 (Eu=0.25, 0.5 and 0.75mM). The morphological changes were analyzed by a JSM-7800F analytical field emission scanning microscope (SEM), JEOL F200 high resolution transmission electron microscope (HRTEM)), and confocal fluorescence microscopy (CFM) techniques. Optical properties have been analysed by photoluminescence (PL) spectroscopy.

The SiQDs@xEZIF-8 maintain the internal spacing of the Si-QDs in the ZIF-8 network and improve energy absorption. The Si QDs embedded in the ZIF-8 polyhedrons could effectively prevent the aggregation-caused quenching (ACQ) effect, resulting in enhanced fluorescence stability even in the solid form, which demonstrates that ZIF-8 could serve as ideal carriers for Si QDs. The PL spectra (Figure 1 (a)) indicate that the PL emission was enhanced via Eu-ZIF-8 through inhibition of inter-QD energy transfer, which prevents large accumulation of Si-QDs. The control over the Si-QDs within the ZIF-8 network paves the way for multidimensional QD structures with tailored electronic couplings and dielectric matrices[6]. In comparison with the ZIF-8 undoped pristine morphology (Figure 2 (a)), there have been observed morphological changes in Eu-ZIF-8 (Figure 2 (c)). The size of the blocks is reduced compared to pristine ZIF-8. The morphology of SiQDs@ZIF-8 and SiQDs@EuZIF-8 (Figure 2 (b) and (d)) shows further size reduction.

This study presents a novel process of encapsulating silicon quantum dots inside a metal organic framework with spatial distribution and engineering the mesoscale compounds with improved emission properties in the solid state. The Si QDs are caged in sodalite-type ZIF-8. It is interesting to note that Si QDs were formed inside the pore structure due to the confinement effect of the coordination space.

References:
1. Gao, L. X., et al. (2023) ACS Appl. Nano Mater., 6, 15054.
2. Yu, H., et al. (2023) ACS Appl Nano Mater., 6, 228.
3. Bruchez, M., et al. (1998). Science, 281, 2013.
4. Wang, Q., et al. (2023) Heliyon, 9, e16081.
5. Kumar, G., et al (2024) Nanoscale Adv.,6, 782.
6. Kumagai, et al. (2021) Chem. Mater. 33, 1607.

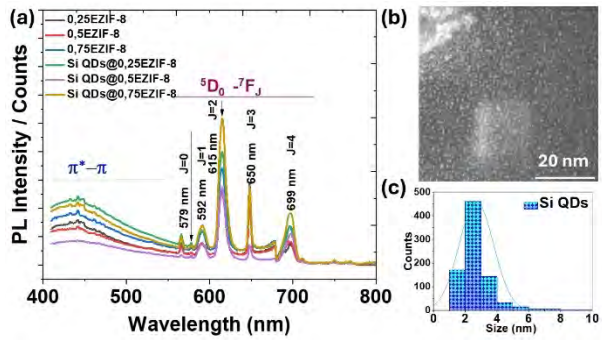

Figure 1. (a) PL spectra of Eu-ZIF-8 and SiQDs@Eu-ZIF-8 (Eu=0.25, 0.5 and 0.75mM), (b) HRTEM bright field images of Si QDs and (c) size distribution of Si QDs.

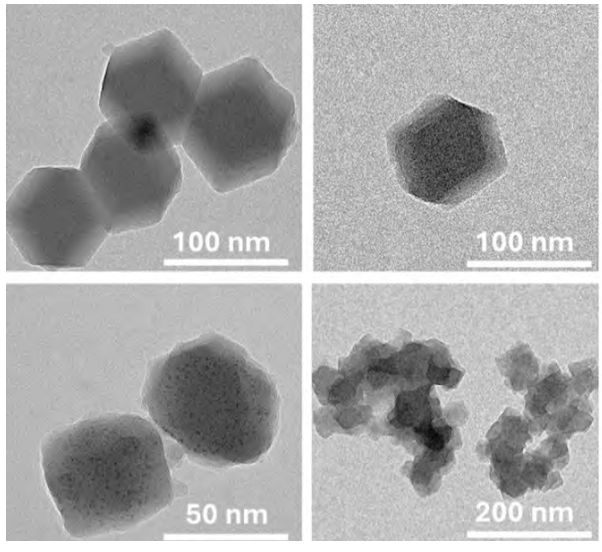

Figure 2. HR-TEM images of (a) pristine ZIF-8, (b) SiQDs@ZIF-8, (c) Eu-ZIF-8, and (d) SiQDs@Eu-ZIF-8 polyhedrons.

Corresponding author: SwartHC@ufs.ac.za

SURFACE MODIFICATION AND CATHODOLUMINESCENCE DEGRADATION OF Y_2O_3:Dy^{3+}, Sm^{3+} THIN FILM

S. Nagarasanakote Jayaramu, E. Coetsee and H.C. Swart

Department of Physics, University of the Free State, Bloemfontein

Cathodoluminescence (CL) degradation measurements of Y_2O_3:Dy^{3+}, Sm^{3+} films were conducted to evaluate their potential application in low-voltage field emission displays. In this study, the CL degradation of Y_2O_3:Dy^{3+}, Sm^{3+} films, deposited using the pulsed laser deposition (PLD), was investigated for potential applications in low-voltage field emission displays and lighting. Auger electron spectroscopy (AES) and X-ray photoelectron spectroscopy (XPS) were employed to monitor surface modifications resulting from surface reactions during prolonged electron beam exposure. The stability of Y_2O_3:Dy^{3+}, Sm^{3+} film under extended electron bombardment was also examined.

The Dy (0.6 mol.%) and Sm (0.6 mol.%) co-doped yttrium oxide nanophosphor was synthesized using the solution combustion method in an air atmosphere. The resulting powder was then annealed at 900 °C for 2 hours in the same atmosphere. Approximately 10 grams of the annealed powder was pressed into a 25 mm diameter disk under a pressure of 12 tons using a hydraulic press. The disks were subsequently placed in a PLD chamber and positioned in a target holder, which was rotated at 10 degrees per minute to prevent laser-pinning. The Si (100) substrate was used for deposition of prepared nanophosphor. During the ablation process, the temperature in the PLD chamber was maintained at 500 °C, and a vacuum base pressure of 2.6×10^{-5} Torr was kept. Ablation was performed using a 266 nm Nd laser with the substrate-target distance set at 5 cm. The laser energy, deposition time, and ablated area were fixed at 50 mJ, 15 minutes, and 1.5 mm, respectively.

The X-ray powder diffraction (XPRD) pattern show the as-deposited Y_2O_3:Dy^{3+}, Sm^{3+} film on the Si (100) substrate at a temperature of 500 °C. The maximum diffraction peak intensity is observed at 29.1°, which can be indexed to cubic Y_2O_3 with the Ia-3 space group, according to the standard card (JCPDS No. 88-1040)[1]. The surface modification of the film by electron beam bombardment was studied using field emission scanning electron microscopy (FESEM). It was observed that the density of the nanoparticles decreased (Figure 1). Additionally, it was revealed that a 2 kV, 3 µA electron beam modified a 3.7 µm diameter area of the film, indicating that the electron beam size is approximately 3.7 µm. Three-dimensional atomic force microscopy (AFM) image of the Y_2O_3:Dy^{3+}, Sm^{3+} film reveals a homogeneous distribution of tiny grains with few isolated areas. The incorporation of Dy^{3+} and Sm^{3+} into the C_2 and S_2 symmetry sites of Y^{3+} in the Y_2O_3 lattice was confirmed by XPS and CL spectra. The Y_2O_3:Dy^{3+}, Sm^{3+} nanophosphor was investigated under vacuum conditions to control surface chemical adsorption. The AES and the CL data collection were performed while the nanophosphor was bombarded with a 3 µA electron beam current at an accelerated voltage of 2 kV in a vacuum. The nanophosphor exhibited a strong yellow band with a maximum at 572 nm, attributed to the $^4F_{9/2}\rightarrow{}^6H_{13/2}$ electric dipole transition of Dy^{3+}. Additionally, relatively weak transitions of Dy^{3+} were observed[2], including $^4F_{9/2}\rightarrow{}^6H_{15/2}$, $^4F_{9/2}\rightarrow{}^6H_{11/2}$ and $^4F_{9/2}\rightarrow{}^6H_{9/2}$, $^6H_{11/2}$. Moreover, the $^4G_{5/2}\rightarrow{}^6H_J$ (J: 7/2, 9/2) transitions of Sm^{3+} were observed in the red visible spectrum. The CL intensities of Dy^{3+} and Sm^{3+} decreased with increasing electron dose in vacuum, stabilizing after an electron dose of approximately 300 C/cm² due to the removal of carbon impurities from the surface of the nanophosphor. The reduction of carbon impurities was confirmed by AES and XPS studies and was attributed to electron-stimulated surface chemical processes.

Y_2O_3:Dy^{3+}, Sm^{3+} films were successfully deposited using the PLD technique. The as-deposited films exhibited a cubic Y_2O_3 structure, and Dy^{3+} and Sm^{3+} were incorporated into the C_2 and S_2 symmetry sites of Y^{3+} in the Y_2O_3 lattice. The CL intensities of Dy^{3+} and Sm^{3+} remained stable after an electron dose of approximately 300 C/cm² in vacuum. This stability suggests that this phosphor may be promising for use in field emission displays.

References:
1. Liu, T., Xu, W., Bai, X. and Song, H. (2012) J. Appl. Phys. 111, 064312.
2. Shivaramu, N.J., Coetsee, E. and Swart, H.C. (2019) J. Vac. Sci. Technol. A 37, 061405.

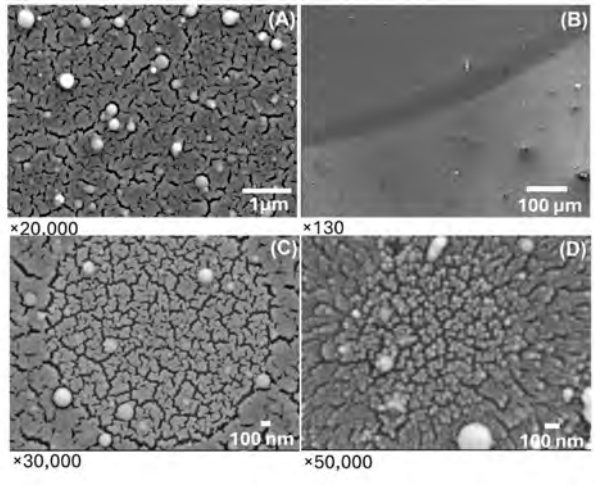

Figure 1. FESEM images of Y_2O_3:Dy^{3+}, Sm^{3+} film: (A) prior and (B-D) post electron beam bombardment.

Corresponding author: CoetseeE@ufs.ac.za

STUDYING RECRYSTALLISATION DYNAMICS OF SWIFT HEAVY ION TRACKS IN YIG

M.M. Badenhorst, E.J. Olivier and J.H. O'Connell

Centre for HRTEM, Physics Department, Nelson Mandela University, Gqeberha

Understanding ion-solid interactions under swift heavy ion (SHI) irradiation conditions and subsequent recrystallisation, especially in amorphisable insulators, has gained theoretical and practical interest. SHIs (E > 1 MeV/amu and mass > 10 amu) induce dense ionisation, resulting in transient melting and the formation of ion tracks within materials. Understanding these interactions will enhance the ability to predict the behaviour of materials exposed to extreme radiation environments, where structural modifications could occur[1].

SHIs induce defect formation on ultra-short timescales (~100 ps), a process currently unobserved through direct experiments. Although Molecular Dynamics (MD) simulations provide insights into defect formation and recrystallisation within the material, these simulations rely on simplified interatomic potentials which limit accuracy[1]. Previous research has focused on SHI-induced damage in various materials such as yttrium iron garnet ($Y_3Fe_5O_{12}$ - YIG) due to its tendency to form continuous amorphous tracks that affect both its structural and magnetic properties[2,3]. However, the in-situ observation of its recrystallisation has not been previously studied using TEM. YIG is used in spintronics as it has relatively low intrinsic damping and excellent electrical insulating properties[4].

In this study, recrystallisation of amorphous ion tracks in single crystal YIG was recorded in-situ at millisecond temporal resolution using a Quantum Detectors MerlinEM high-speed camera mounted on a JEOL ARM200F. In-situ heating was facilitated by a DENS Solutions Wildfire heating holder. Through thermal excitation, the quenched amorphous tracks were recrystallised allowing us to study the dynamics of this process and how local stresses and defect densities affect the recrystallisation rate.

The YIG specimens were irradiated at room temperature with high-energy 167 MeV Xe ions using the IC-100, and U-400 cyclotrons at the FLNR JINR (Dubna, Russia), and the DC-60 cyclotron at the Astana Branch of the Institute of Nuclear Physics (Nur-Sultan, Kazakhstan) to a fluence of 2×10^{11} cm^{-2}. Electron-transparent lamellae were prepared by FIB lift-out using an FEI Helios Nanolab 650 FIB-SEM and mounted onto a Si_3N_4 MEMS chip for in-situ heating experiments.

The HRTEM image in Fig. 1, shows single-crystal YIG irradiated with Xe ions (S_e = 24.89 keV/nm) and circular track morphologies, indicative of cross-sections of amorphous cylindrical ion tracks. The amorphous nature of the tracks was confirmed by the uniform contrast and the absence of diffraction contrast and lattice fringes and is consistent with previous studies[2,5]. Initial results showed anisotropic annealing of tracks resulting in their circular cross sections becoming more elliptical during recrystallisation with the long axes of ellipses near parallel with each other. It is unclear at this point whether this phenomenon is due to bend stresses in the lamella due to thermal expansion. To answer this question, future datasets will include specimen thickness data and the location of mechanical anchor points relative to the field of view.

Using automated ion track identification and measurement tools, changes in track morphology, and spatial distribution will be investigated in order to understand the recrystallisation dynamics during thermal excitation.

References:
1. Lang, M., et al. (2020) Comprehensive Nuclear Materials. Oxford, Elsevier.
2. Janse van Vuuren, A., et al. (2019) Proc. 13th Int. Conf. Interact. Radiat. Solids, 51, 567.
3. O'Connell, J.H., et al. (2018) Proc. 12th Int. Conf. Ion Implantation and Other Applications of Ions and Electrons, 136, 233.
4. Arsad, A.Z., et al. (2023) Appl. Sci. 13(2), 1218.
5. Costantini, J.-M., Desvignes, J. M. and Toulemonde, M. (2000) J. Appl. Phys. 87(9), 4164.

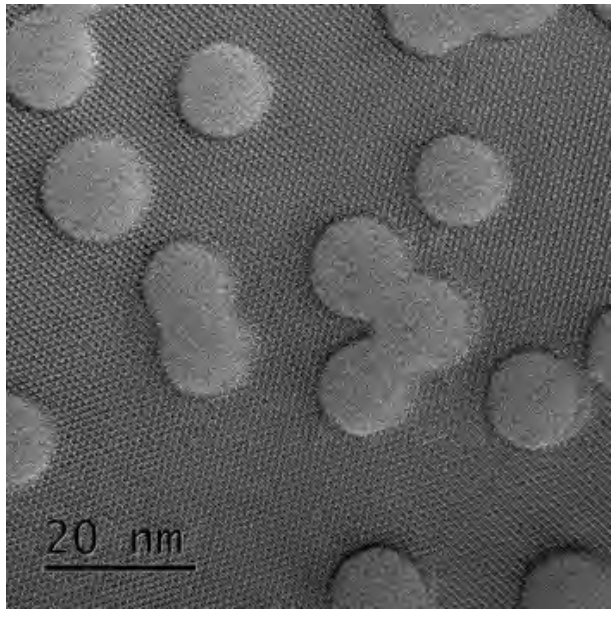

Figure 1. HRTEM image of single-crystal YIG irradiated with high energy Xe ions (S_e = 24.89 keV/nm)

Corresponding author: s223108049@mandela.ac.za

THE MICROSTRUCTURAL RESPONSE OF POLYCRYSTALLINE Si3N4 WITH VARYING AL-IMPURITY CONCENTRATIONS TO SWIFT HEAVY IONS.

A. Janse van Vuuren[1], V.A. Skuratov[2] and A. Ibrayeva[3]

[1]Centre for HRTEM, Department of Physics, Nelson Mandela University, Gqeberha, [2]Flerov Laboratory for Nuclear Reaction, Joint Institute for Nuclear Research, Dubna, Russia, [3]Institute of Nuclear Physics, Nur-Sultan, Kazakhstan

Certain material properties have a significant impact on the degree of damage which is induced by swift heavy ions (SHIs). The thermal conductivity and the threshold stopping power may both be influences by several material properties such as the presence of dopants or defects, irradiation temperature, and the phase of the material. Other parameters such as particle size and matrix effects for embedded nanoparticles and lattice structure/complexity also play a role in the latent disorder in certain materials[1,2].

In this investigation the role of Al impurities on the microstructural response of polycrystalline silicon nitride (p-Si_3N_4) to swift ions is analysed. Samples were irradiated with Xe (220 MeV) and Bi (670-710 MeV) ions to various fluences ranging from non-overlapping to overlapping ion track regimes (10^{10} to 10^{14} ions.cm^{-2}). Si_3N_4 samples with Al impurity concentrations ranging from 0.1 at.% to 3 at. % were investigated.

Structural and compositional analysis was performed using either a JEOL ARM200F or JEOL JEM 2100 TEM both operated at 200 kV. Planar TEM lamellae, where the track core is along the viewing direction, were produced using Focussed Ion Beam techniques in a Thermo Fisher Helios Nanolab 650 FIB-SEM. Samples were extracted from the first 2 µm where the ion stopping power is highest and close to constant.

The composition or impurity concentrations in each of the specimens was confirmed using electron energy loss spectroscopy (EELS). Results show that the manufacturer specified values for Al impurities are in good agreement with results from the EELS data.

At lower ion energies (220 MeV Xe) and stopping power induced ion tracks are discontinuous in nature. The results also suggest that the amount of disorder increases with increasing impurity levels even at the lower end of the ion energies used (Fig. 1). In the case where samples were irradiated with higher energy Bi ions (670 - 710 MeV), and hence higher stopping power, the tracks in the sample with the lowest impurity level are discontinuous in nature whereas the other two with higher impurity levels present continuous amorphous tracks with track diameter increasing with impurity level (Fig. 2). The average ion track diameter in the sample with 1 at.% Al is 2.8 ± 0.3 µm and in the samples with 3 at.% it is 3.6 ± 0.3 µm.

The threshold electronic energy loss (S_{et}) required to induce amorphous tracks was found to decrease with increasing Al fraction from above 33 keV/nm (0.1 at.% Al) to below 22 keV/nm for specimens containing approximately 3 at.% Al. All specimens were partially amorphized at overlapping ion fluences > 10^{13} ions.cm^{-2} (Fig. 3). Therefore, the amorphous fraction increases with increasing Al concentrations at the same ion fluence.

The presence of Al impurities, which often occupy interstitial and/or substitutional sites in Si_3N_4, are likely to lower the thermal conductivity through an increase in phonon scattering.

References:
1. Rogozhkin, S.V, et al. (2021) NIMB 486, 1.
2. Rymzhanov, R.A., et al. (2019) Sci. Rep. 9, 3837.

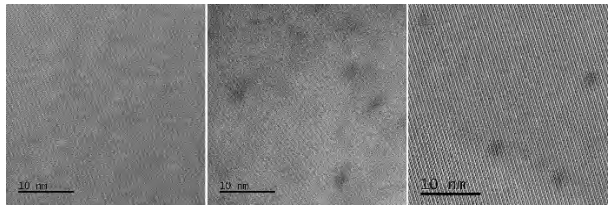

Figure 1. BF STEM micrographs of p-Si_3N_4 irradiated with Xe (Se ≈ 21.9 keV/nm) to non-overlapping track fluence. From left-to-right 0.1 at% Al, 1.0 at% Al and 3.0 at% Al.

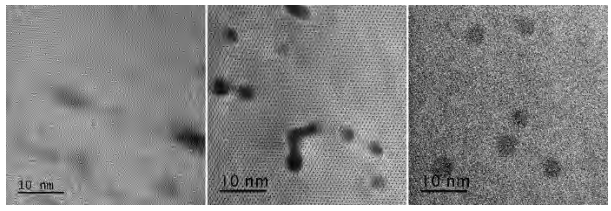

Figure 2. BF STEM micrographs of p-Si_3N_4 irradiated with Bi (Se ≈ 33.6 keV/nm) to non-overlapping track fluence. From left-to-right 0.1 at% Al, 1.0 at% Al and 3.0 at% Al.

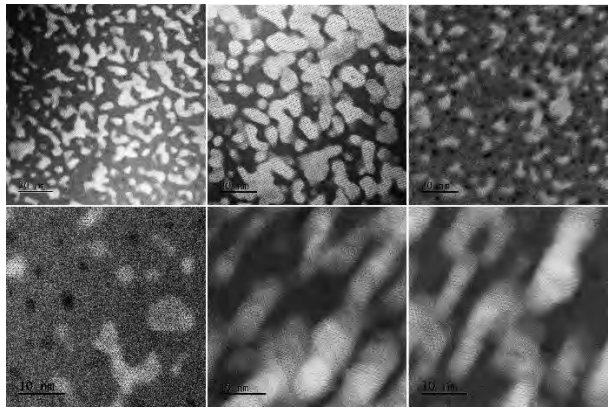

Figure 3. HAADF STEM micrographs of p-Si_3N_4 irradiated with Xe (top row) and Bi (bottom row) to overlapping track fluences. From left-to-right 0.1 at% Al, 1.0 at% Al and 3.0 at% Al.

Corresponding author: arnojvv@gmail.com

TEM ANALYSIS OF THE TETRAGONAL PHASE FRACTION FORMATION IN MONOCLINIC ZIRCONIA AT INTERMEDIATE SHI FLUENCES

M.E. Lee[1], J.H. O'Connell[1] and V. Skuratov[2]

[1]Centre for HRTEM, Nelson Mandela University, Gqeberha, South Africa, [2]FLNR, JINR, Dubna, Russia

A number of authors have reported on SHI irradiation studies for monoclinic (m) zirconia and have shown that the subsequent transformation to the tetragonal (t) phase (m→t) was stabilized at room temperature (RT) after exposure to suitable irradiation fluences[1-3]. This tetragonal transformation has been quantitatively demonstrated using techniques such as Raman spectroscopy and X-ray diffraction (XRD) for SHI irradiation fluences down to 2 x 10^{12} for heavy ions and 5 x 10^{13} cm^{-2} for light ions[4]. The "apparent" fluence threshold for the m→ t transformation is probably due to the detection limit (~ 1-2 vol%) for the Raman and XRD techniques. However, O'Connell *et al* reported on the direct observation of individual tetragonal ion tracks formed in monoclinic zirconia (ZrO_2) as a result of 167 MeV Xe irradiation (fluence 2 x 10^{10} cm^{-2}) at room temperature[5]. In this work we report on the direct observation, by transmission electron microscopy (TEM), of the response by monoclinic zirconia to ion irradiation at intermediate fluences covering both the single track and track overlapping regimes.

Experimentally, sections of single crystalline m-zirconia were irradiated with 150 MeV Xe ions at a fluence in the range 4 × 10^{10} – 1 x 10^{13} cm^{-2} at room temperature. Electron transparent lamellae were prepared by FIB lift out technique using an FEI Helios NanoLab 650 and analysed using a double Cs corrected JEOL ARM200F operated at 200 kV.

To simulate the effect of track overlap, the resultant interaction of tracks for the m-zirconia specimen irradiated from two different opposite directions at 45º to the surface (both at a fluence of 2 x 10^{10} cm^{-2}) are shown in figure 1. It was noted that the tracks from the second dose are more continuous which demonstrates the annealing effect of the second dose on the first dose of ions. The HRTEM cross-sectional images of m-zirconia irradiated at 1 x 10^{13} cm^{-2} perpendicular to the surface are shown in figure 2. The zone axis is along the $[100]_m$. The image reveals highly strained material and that the ion tracks are not visible at exact focus. Three different regions for the section are observed to produce different FFTs with the FFT in Fig 2(b) corresponding to the monoclinic $[100]_m$. However, the FFT for images for figure 2(a) and (c) reveal missing reflections with respect to (b). This result is an indication of a non-homogeneous structural evolution in contrast to the results obtained at low fluences with the formation of tetragonal segments with single ion tracks.

References:
1. Simeone, D *et al,* (2008)Nucl. Instr. and Meth. B 266, 3023.
2. Baldinozzi, G *et al*, (2006) Phys. Rev. B 74, 132107.
3. Benyagoub, A (2003) Nucl. Instr. and Meth. B 245, 225.
4. Schuster, B *et al,* (2009) Nucl. Instr. and Meth. B 267, 964.
5. O'Connell, J.H., Lee, M.E and Skuratov, V.A (2020) Nucl. Instr. and Meth. B 473, 1.

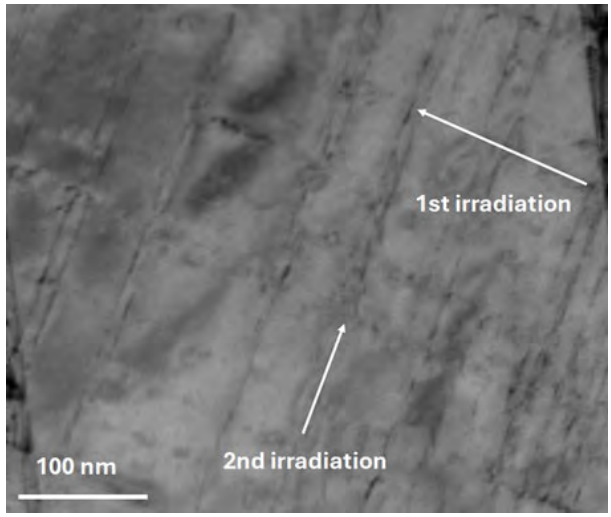

Figure 1. TEM BF image showing interaction of tracks incident in two direction**s.**

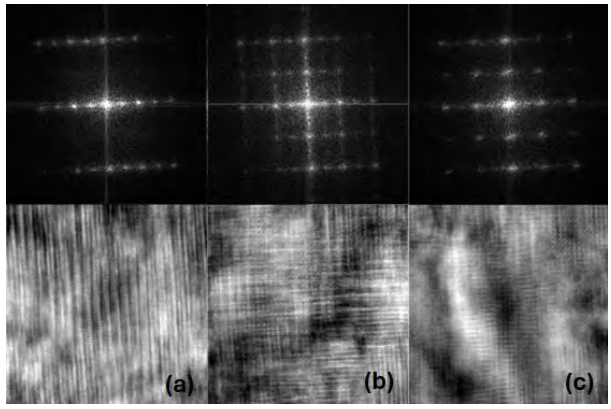

Figure 2. HRTEM image showing highly strained material for three different regions of the section and the corresponding FFTs.

Corresponding author: michael.lee@mandela.ac.za

REAL-TIME OBSERVATION OF MOLECULAR DYNAMICS AND CHEMICAL REACTIONS IN STEM

R.R. Zamani[1], C. Ozsoy-Keskinbora[1], P. Longo[2], E. van Cappellen[2], I. Lazic[1] and S. Lazar[1]

[1]Thermo Fisher Scientific, Eindhoven, The Netherlands, [2]Thermo Fisher Scientific, Hillsboro, USA

In situ transmission electron microscopy (TEM) has opened novel ways to study chemical reactions and molecular dynamics real-time at atomic scale. Nowadays, thanks to MEMS-based technology, we can easily observe samples in a state that is very close to real-application conditions. However, regardless of the technological advances of MEMS-based holders, some reactions are still extremely difficult to observe, either because of the intrinsic beam-sensitive nature of the sample or because we are limited by the non-ideal collection efficiencies of the common analytical techniques, such as energy dispersive X-ray spectroscopy (EDS) or experimental complications of electron energy loss spectroscopy (EELS).

An example of such beam-sensitive samples is zeolite. Zeolites are very versatile compounds with many present and future applications. Their porous structure makes them ideal molecular sieves. Unfortunately, due to beam-sensitivity issue, imaging zeolites requires special care to preserve their native structure. Using integrated differential phase contrast scanning TEM (iDPC-STEM), a method developed by Thermo Fisher Scientific[1], we routinely image beam sensitive materials with up to orders of magnitude lower electron doses compared to conventional STEM techniques such as high-angle annular dark-field (HAADT). This method, coupled with newly developed single-electron-sensitive detectors such as Panther STEM, can provide precise information on small molecules; and by using advanced in situ gas/liquid/heating holders, the whole reactions can be recorded with high frame speeds. Among many advantages of iDPC-STEM, we point out that it has the potential of providing ultimate spatial resolution under low-dose conditions. We show the capabilities of this technique through an in situ gas experiment on zeolite ZSM-5. As shown in the figure, we clearly observe the molecular dynamics of interactions between small molecules and zeolite ZSM-5[2,3].

When applying stimuli to samples, TEM/STEM imaging can be performed relatively easily. However, spectroscopy faces more technical difficulties, e.g. complication of EELS experiment setup, or the sensitivity of EDS detectors, hindering the tracking of compositional changes during reactions. The second part of the talk will highlight the advantages of recent technological developments with EELS and EDS. As an example, we show in situ STEM-EDS chemical mapping of Au-Ag core-shell nanorods throughout a heating experiment and observe the chemical reactions in real time.

Moreover, we will talk about a newly developed Electron Dose Control (EDC) package for accurate dose and dose-rate management, which allows the user to know, choose, monitor, document and reproduce the exact amount of electron at will. This provides the possibility of highly accurate quantitative analysis. Using such technologies make a dramatic impact on the way such materials behave in real-world applications such as catalysis and renewable energies.

References:
1. Lazic I. et al (2016) Ultramic. 160, 265.
2. Shen B. et al (2022) Nature 607, 703.
3. Xiong H. et al (2022) Science 376, 491

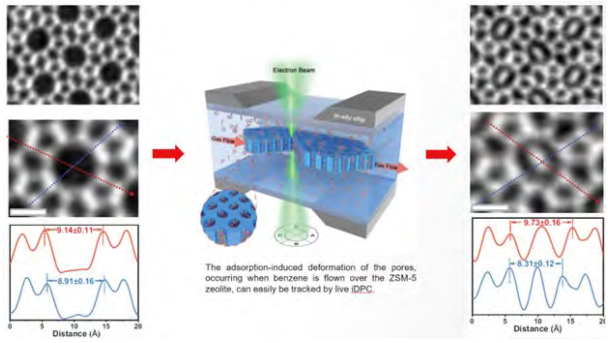

Figure 1. In situ study of zeolite ZSM-5 before (left) and after (right) exposure to benzene gas.

Corresponding author: reza.zamani@thermofisher.com

3D RGO HYBRID EVAPORATOR FOR EFFICIENT SOLAR DESALINATION

W.J. Lawrence, F.A. Bezza, S.M. Tichapondwa and E.M.N. Chirwa

Water Utilisation and Environmental Engineering Division, Department of Chemical Engineering, University of Pretoria, Pretoria

Photothermal materials are the most essential elements in the solar-driven interfacial desalination process and are crucial for converting solar energy to heat, thus generating vapour. Carbon-based materials are extremely popular photothermal materials as they exhibit broadband absorbance capacity and exceptional chemical stability[1]. The combination of reduced graphene oxide (rGO) with black titanium dioxide (black TiO_2) has been reported to enhance photocatalytic activity[2]. The aim of this study is to investigate the application of a 3D black TiO_2/rGO composite evaporator for solar steam generation.

Graphene oxide (GO) was prepared using Tours' method[3]. Black TiO_2 was prepared using $NaBH_4$ reduction of commercial grade TiO_2. To fabricate the 3D black TiO_2/rGO evaporator, hydrothermal reduction of a GO suspension containing the black TiO_2 particles was carried out using a Teflon-lined autoclave placed in an oven at 170 °C for 17 hours, cooled to room temperature and freeze-dried for 72 hours. For the solar steam generation/desalination test, the solar evaporator was placed on a cellulose sponge with very low thermal conductivity, high hydrophilicity, and highly porous structure to ensure thermal insulation and efficient water transferability and placed in an enclosed transparent glass cover using vacuum seal grease to prevent convective heat loss. Natural sunlight was simulated using a xenon-arc lamp-based solar simulator. The 3D hybrid material was characterised by powder X-ray diffraction (PXRD) using a Bruker D2 Phaser using (CuKα radiation, λ = 1.54184 nm), transmission electron microscopy JEOL JEM 2100F TEM, Brunauer-Emmett-Teller (BET) using a NOVA Touch LX2 system (N_2 isotherm), scanning electron microscopy Zeiss Ultra Plus FEG SEM coupled with an Oxford instruments detector and Aztec 3.0 SP1 software energy dispersive X-ray spectrometer (EDX).

Fig. 1a shows the distribution of spherically shaped black TiO_2 particles on the rGO surface revealing a heterogeneous structure with large agglomerates of black TiO_2 particles occurring on a vast majority of the composite. Fig. 1b displays the highly porous, fluffy, and wrinkled morphology of the evaporator, illustrating the large surface area which is favourable for increased water and heat absorption potential. The obtained BET surface area of 22.1 m^2/g further indicates the effective fabrication using hydrothermal reduction. Fig. 2a shows the PXRD patterns of the as-prepared composite and its components. The sharp peaks demonstrated the good crystallinity of the sample. The X-ray diffractograms of the sample indicate the presence of both the anatase and rutile phases of TiO_2. The TEM image (Fig. 2b) shows the anchoring of black TiO_2 particles onto the rGO nanosheets.

The 3D hybrid evaporator showed a high surface temperature increase from 20.2 to 46 °C within 90 minutes of starting the interfacial desalination test. The photothermal conversion efficiency was determined to be 82.38 % under 1 sun illumination and an evaporation rate of 1.19 $kg/m^2 \cdot h$. The high solar-to-thermal conversion efficiency is obtained by maximising the solar absorbance while reducing the thermal radiation and conduction loss. The highly porous structure with a large surface area and the synergistic photocatalytic activity of the black TiO_2 and the rGO promoted the high photothermal conversion efficiency and steam generation potential demonstrated by the evaporator.

In conclusion, the 3D black TiO_2/rGO evaporator has enhanced surface area, hydrophobicity, and good photothermal conversion efficiency. The junction between black TiO_2 and rGO displayed a significant degree of disorder owing to the strong interaction between black TiO_2 and rGO sheets. The 3D hybrid evaporator shows promising avenues for large-scale application of interfacial water evaporation/desalination.

References:
1. Li, Z., at al. (2019) RRL Solar. 3(3), 4.
2. Shafiee, A., et al. (2022) Applied Surface Science. 575, 151718.
3. Habte, A.T. and Ayele, D.W. (2019) Adv. Mat. Sci. Eng. 2019, 5058163.

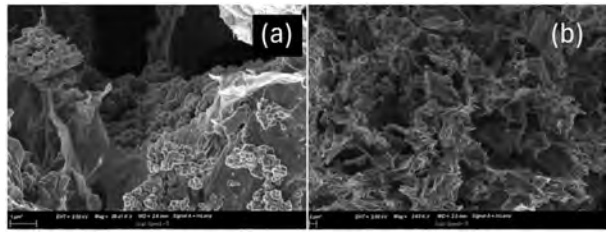

Figure 1. SEM images of 3D black TiO_2/rGO composite.

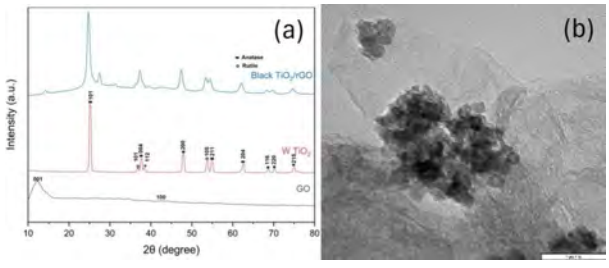

Figure 2. PXRD patterns (a) and TEM image (b) of the 3D black TiO_2/rGO composite.

Corresponding author: u22961896@tuks.co.za

ASSESSMENT OF CREEP CAVITATION IN SERVICE-EXPOSED 12%Cr TMF STEEL

G. Marx[1], N.W. Mfuma[1] and J.E. Westraadt[2]

[1]Centre for HRTEM, Nelson Mandela University, Gqeberha, [2]Centre for Electron Microscopy and Analysis, The Ohio State University, Ohio, USA

Despite the increasing pressure to move to competitive cleaner and renewable technologies, ageing fossil fuel-based technologies are still dominating the electrical power generating industry. In addition, partial component replacement by welding on the service-exposed components remains the favourable interim plan until newer technologies can come online. Tempered martensite ferritic (TMF) steels with 9-12% Cr are mainly used in the steam pipes, turbines and boilers. It is well-known that creep cavities form in TMF steels during service[1]. The main failure mechanism of TMF steels during service exposure is the formation and growth of microcracks from closely spaced cavitating grain boundary interfaces[2]. This failure mechanism is called Type IV cracking in the case of weldments[3]. Thus, the cavitation state of the steel strongly determines the remaining life of the TMF steel. Metallographic replication of component or weldment surface remains the favourable method by power plants to determine the cavitation state[4]. This entails manually counting of cavities from acetate films using light microscopy (LM). This study compares the possible approaches to assess the creep cavitation state of service-exposed TMF steels using electron and light microscopy.

The material used for this study was service-exposed (555°C; 17.0 MPa; 130 kh) X20CrMoV11-1 (12% Cr) stainless steel pipework. Surface replicas were prepared from the pipework and the cavities analysed using the standard method[5]. The bulk specimens were mounted in a Phenolic resin and polished to a colloidal surface finish for LM and scanning electron microscopy (SEM) analysis. Light micrographs covering 296 x 296 µm^2 areas (16 in total) were acquired from the surface of the polished bulk specimens using an Olympus DSX510 Digital Microscope (total sampling area of 1.4 mm^2). Backscattered electron (BSE) and secondary electron (SE) - SEM images were acquired using a JEOL JSM 7001F FEG-SEM. The cavities were segmented and quantified from the images using MIPAR™ image analysis software[6]. Inclusions usually have diameters larger than 3 µm while the spatial resolution of LM is ~1 µm. Therefore, only features with equivalent circle diameters (ECD) between 1 and 3 µm were quantitatively analysed as cavities.

A mean cavity density of 820 ± 160 voids/mm^2 was measured from the LM results, while the surface replication measured 300 – 800 voids/mm^2. This is what is expected of a long-term service-exposed X20 steel[4]. It was also possible to measure the mean ECD as 1.51 ± 0.03 µm and the mean nearest neighbour distance as 18.62 ± 1.85 µm, respectively. Care must be taken to interpret the mean ECD value since some etching may have occurred during polishing. Fig. 1(a) and (b) compare the SE and BSE images of the same area. Cavities were measured as black features and Fig. 1(c) shows the extracted cavities from the SE image. The BSE image details for the cavities are limited due to imaging artefacts compared to SE imaging as shown by the red arrow in Fig 1(a) and (b). Since the grains are visible from the SE image it was possible to identify small closely spaced cavities along grain boundaries with ECD as small as 0.04 µm as shown in Fig. 1 (d). As previously mentioned, with continued creep exposure, the closely spaced boundary cavities play a significant role in the formation and growth of microcracks, ultimately leading to material failure.

It can be concluded that (1) similar creep cavity densities (ECD > 1 µm) are measured from polished bulk specimens as compared to surface replicas, and (2) the determined creep cavitation state of a TMF steel has been shown to be more accurate using SE imaging since local measurements are also included for cavities with ECD < 1 µm. Future work will include applying the post-processing approach developed during this study to surface replicas for automated detection and quantification of voids using machine learning.

References:
1. Aghajani, A. et al. (2009) Acta Mater 57(17), 5093.
2. Eggeler, G. et al. (1989) Acta Metall 37(1), 49.
3. Cerjak, H. and Mayr, P. (2008) Creep-resistant steels. England, Woodhead Publishing Ltd.
4. Van Zyl, F.H. et al. (2005) Proc. ECCC Creep Conf., 12.
5. Eskom Standard, Reference 240-75109745.
6. Sosa, J.M. et al. (2014) Integr. Mater. Manuf. Innov. 3(1),10.

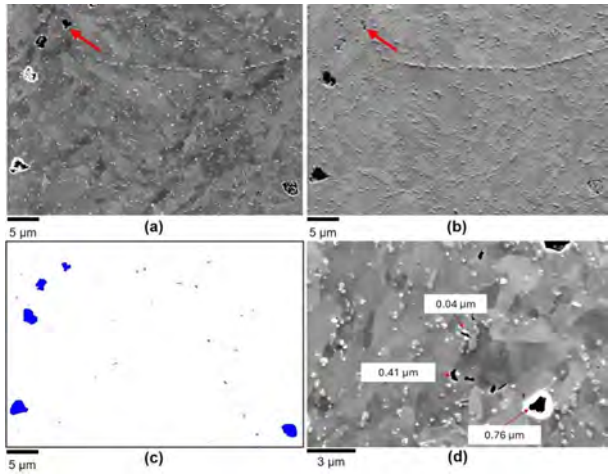

Figure 1. (a) SE image, (b) BSE image of the X20 steel polished bulk specimen, (c) isolated cavities with > 1 µm ECD (blue) and < 1 µm ECD (red) cavities of the same area, (d) higher magnification SE image with measured ECD values of some of the cavities.

Corresponding author: Geneveve.Marx@mandela.ac.za

IDENTIFICATION OF COPPER AND COBALT-BEARING MINERALS IN COPPER SLAG

T.Z. Papo[1], M.M. Ramakokovhu[1] and J. Mulwanda[1,2]

[1]Institute for Nano-Engineering Research, Department of Chemical, Metallurgical and Materials Engineering, Tshwane University of Technology, Pretoria, South Africa, [2]School of Mines and Mineral Sciences, Copperbelt University, Kitwe, Zambia

Copper slag, a by-product of copper smelting, contains not only copper but also other valuable metals like cobalt[2].The smelting process produces slag, whose complicated chemical makeup causes major environmental problems such soil erosion, water pollution, and ecosystem disruption[3]. Slags undergo phase and chemical changes during pyrometallurgical processing, which results in diverse mineralogical patterns. Comprehending the mineralogy of the slag is crucial, as it offers valuable information about its composition and possibility for recovering metal[1].

This study focuses on detecting and characterizing copper and cobalt-containing minerals within the slag using analytical techniques such as X-ray Fluorescence (XRF), Scanning Electron Microscopy-Energy Dispersive X-ray Spectroscopy (SEM-EDS), and X-ray Diffraction (XRD). These methods help identify the composition, structure, and mineral phases present in the slag, offering insights into potential metal recovery, environmental impacts, and the slag's applicability in various industries. Tyler series employed to determine the Particle Size Distribution (PSD) of the obtained copper slag.

The XRD analysis identified copper ferrite ($CuFeO_2$) and cobalt ferrite ($CoFe_2O_4$) as the main Cu and Co-bearing minerals, along with impurities like hematite (Fe_2O_3), magnetite (Fe_3O_4), silica (SiO_2), and iron silicide (FeSi). The complexity surface morphology is shown on Figure 1, with various patterns and irregularities that indicate different material phases. The strong peaks for hematite and magnetite suggest these are major components of the slag shown in Figure 2 from SEM/EDS on spectrum 59, while the smaller peaks for cobalt ferrite and copper ferrite indicate they are present in smaller quantities. XRF analysis determined the wt% of CuO and Co_2O_3 in the slag to be 1.38% and 1.40% respectively. PSD shown that the 50% passing rate or d_{50}, was attained at a particle size of about 125 µm. Nonetheless, 200 µm was found to be the particle size that corresponds to the 80% passing rate, or d_{80}. The material may be fairly coarse, as indicated by the d_{80}.

These findings suggest that the slag contains recoverable copper and cobalt, making it a potential resource for recycling in industries. This can help reduce waste and support sustainable practices, while also prompting further research on environmental impacts which is in alignment with Responsible Consumption and Production (Sustainable Development Goal 12), the insights gained from copper slag production can inform the development of sustainable mining and processing methods.

References:
1. Crundwell, F., Du Preez, N. & Knights, B. (2020) Mineral Engineering, 156, 106450.
2. Dzinomwa, G., Mapani, B., Nghipulile, T.& Maweja, K. (2023) Materials, 16(18), 6126.
3. Gabasiane, T., Danha, G., Mamvura, T.& Mashifana, T. (2021) Heliyon, 7(4), e06757

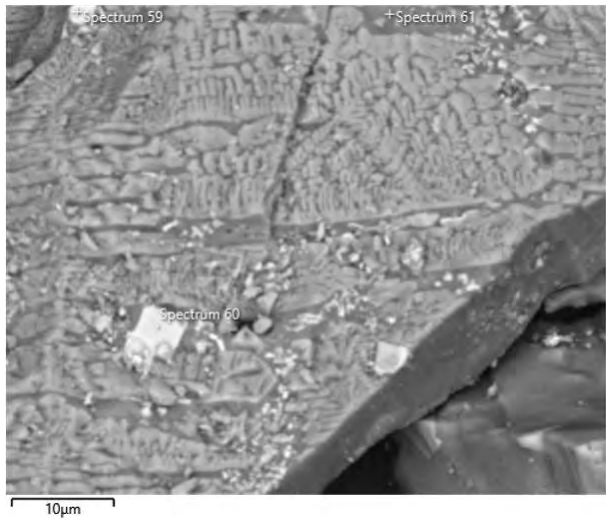

Figure 1. SEM microstructure of the as-received copper slag from magnifications 10µm.

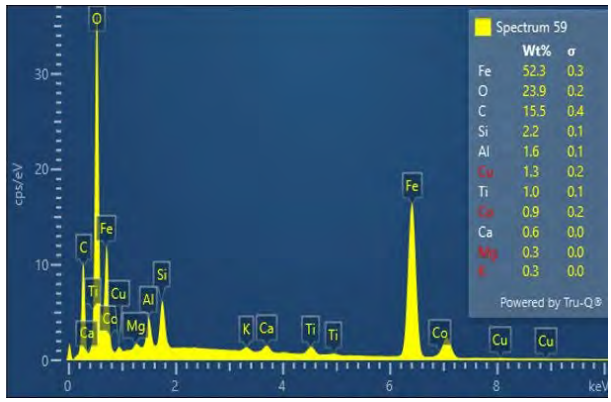

Figure 2. Energy Dispersive X-ray Spectroscopy of the as-received copper slag.

Corresponding author: zuzilethabiso@gmail.com

COBALT-BASED PEROVSKITE OXIDE CATALYSTS FOR THE PREFERENTIAL OXIDATION OF CARBON MONOXIDE FOR HYDROGEN FUEL CELLS

N. Ndila and P.J. Kooyman

Catalysis Institute, University of Cape Town, Cape Town

Proton exchange membrane fuel cells (PEMFCs) are one of the leading sustainable energy sources and play a vital role in the energy transition process[1]. Currently, 95% of H_2 production is via steam reforming, however, this H_2 must be purified to reduce the CO concentration before its utilization in PEMFCs[1]. CO deactivates the Pt catalyst of fuel cells[2]. Preferential oxidation of carbon monoxide (CO-PROX) is one of the most effective methods for H_2 purification for fuel cells[2]. Cobalt-based catalysts are highly active for CO-PROX[2,3]. However, studies have shown that during the time on stream, Co_3O_4 catalysts deactivate via the reduction of Co_3O_4 to metallic Co at temperatures above 175°C[2,3]. Metallic Co is active for CO methanation which consumes the desired H_2 [2,3]. To address the deactivation of cobalt-based catalysts, this study investigates the stabilization of Co^{3+}/Co^{2+} cations in a perovskite oxide matrix ($LaCoO_3$) to overcome overreduction to metallic cobalt.

Additionally, we investigate the effect of partially substituting La^{3+} with Sr^{2+} ($La_{1-x}Sr_xCoO_{3-\delta}$) or Ca^{2+} ($La_{1-x}Ca_xCoO_{3-\delta}$) where (x = 0, 0.1, 0.15, 0.2, 0.3) on the activity, selectivity, and phase stability of the catalysts during CO-PROX. The catalysts were characterized by XRD, EDS, BET, and ICP-OES. The redox properties of the catalysts were investigated via TPR/TPO cycles. The correlation of the catalyst structure with catalytic performance was investigated via in-situ XRD.

XRD patterns showed no diffraction peaks for impurities related to Sr and Ca phases. Rietveld refinement calculations showed that the unit cell volume increased with increasing Sr^{2+} content because Sr^{2+} has a bigger ionic radius than La^{3+}. Conversely, it decreased with increasing Ca^{2+} content because of its smaller radius. This shows the successful incorporation of Ca^{2+} and Sr^{2+} in $LaCoO_3$. Elemental mapping showed that we have a homogeneous distribution of the elements in the catalyst which shows the successful synthesis of our catalyst as shown in figure 1 and 2. The catalytic performance evaluations showed that the catalytic performance improves with the incorporation of Ca and Sr. $LaCoO_3$ achieved a maximum CO conversion of 58% at 300°C, $La_{0.85}Sr_{0.15}CoO_3$ achieved 99% at 250°C, and $La_{0.85}Ca_{0.15}CoO_3$ achieved 90% at 270°C. Additionally, there was no CH_4 formation for these catalysts which shows that they more stable compared to conversional Co_3O_4 catalysts. The partial substitution of La^{3+} with Sr^{2+} or Ca^{2+} leads to lattice distortions and the formation of oxygen vacancies to preserve charge neutrality[4]. This improves the lattice oxygen activity and mobility, thus improving catalytic performance.

These catalysts can potentially replace conventional cobalt-based catalysts as they exhibit improved catalytic activity and stability.

References:
1. Germscheidt, R et al. (2021) Adv. Energy Sustainability Res, 2, 1
2. Holladay, J.D *et al.,* (2009) Catal. Today, 139, 244
3. Lukashuk, L. *et al.* (2016) J. of Catalysis, 344, 1
4. Choi, S et al. (2013) *ASC Catalysis*, 3, 2716

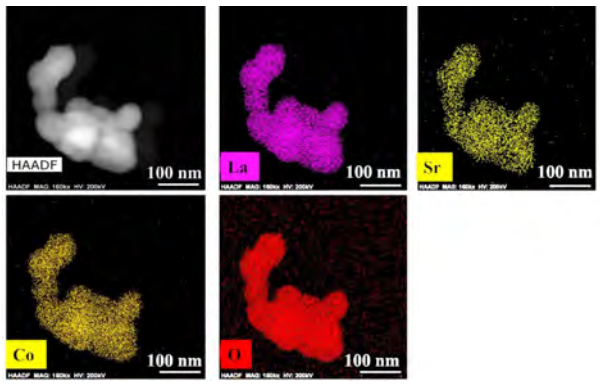

Figure 1. High-angle annular dark field image of $La_{0.85}Sr_{0.15}CoO_3$ and elemetal maps of La, Sr, Co, and O.

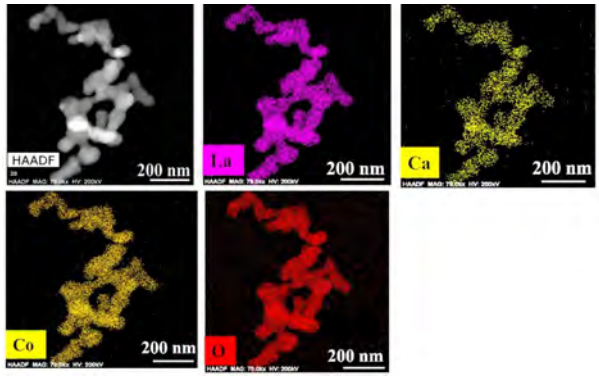

Figure 2. High-angle annular dark field image of $La_{0.85}Ca_{0.15}CoO_3$ and elemetal maps of La, Ca, Co, and O.

Corresponding author: ndlnol010@myuct.ac.za

RECOVERY OF IRON FROM ROAST-LEACH TITANOMAGNETITE FERROVANADIUM RESIDUE

M. Nevondo, L. Koech, M.M. Ramakokovhu, B.M. Sesane and B. Msiza

Tshwane University of Technology, Pretoria West, Pretoria

The vanadiferous titaniferous magnetite (titanomagnetite) mineral deposits are mainly found in the Bushveld Complex of South Africa. The mineral deposits are mined by utilizing opencast mining techniques. Titanomagnetite resources contain valuable elements such as iron, vanadium, and titanium with extremely high potential value. The exploitation of titanomagnetite has thus received much attention. The processing of titanomagnetite into ferrovanadium results in the production of high quantities of waste slag stockpiles, which contain titanium (rutile) and iron. The waste slag stockpiles are highly magnetic and render the stockpiles unusable. Vanadium extraction tailings are hazardous solid waste generated from the vanadium extraction process, which uses vanadium-bearing converter slag as raw materials.

The residue was sampled and subjected to various characterization techniques, including XRD, SEM, ICP-OES, and XRF, to analyze phase transformation, morphology, and chemical composition. According to XRF analysis, iron and titanium-bearing minerals present in the ore, that is, Fe_2O_3 and TiO_2, constituted 78.45% and 12.61%, respectively. SiO_2 (2.73%), Al_2O_3 (2.35%), and Na_2O (1.80%) were the major impurities reported. The ICP-OES following aqua-regia digestion had the highest concentrations of Fe, Ti, and V recorded at 75 µm particle size: 63,789 mg/l, 5,339 mg/l, and 63.74 mg/l, respectively. XRD patterns exhibited the presence of $FeTiO_3$ (ilmenite) and VO_2 in the as-received samples confirming the XRF and ICP-OES analysis. SEM morphology indicated dominant presence of ilmenite in light grey colour, while VO_2 appeared darker.

Mineralogical analysis showed that the minerals that need to be extracted, i.e., iron and titanium, were in higher quantities than gangue components, rendering them more amenable for extraction. The study also evaluated the behavior of the roast-leach ferrovanadium residue under leaching with HCl. The optimum leaching conditions were achieved at a temperature of 80°C, an acid concentration of 10.2 M, a 4-hour leaching period, a particle size of 75 µm, an agitation rate maintained at 420 rpm, and a pulp density of 1:20. Leaching results illustrated that the dissolution rate increased with higher acid concentrations, elevated temperatures, and prolonged leaching times.

The XRD patterns of the leach residue revealed decreasing peak intensities of ilmenite, rutile, and hematite, indicating iron and titanium leaching. SEM morphology of the leach residue indicated disoriented and rough morphology to showing glassy phase obtained from the fluxes of the residue during roasting and the crystallographic structure were broken down during leaching of the roast-leach ferrovanadium residue.

References:
1. Rodriguez, M.H, Rosales G.D, Pinna, E.G, et al (2020) Metals 10, 497
2. Ramakokovhu, M.M., Olubambi, P.A., Mbaya, R.K.K., et al. (2020) 10, 1022
3. Gwatinetsa, D., (2014) Distribution of iron-titanium oxides in the vanadiferous main magnetite seam of the upper zone: Northern limb, Bushveld complex. MSc Thesis, Rhodes University

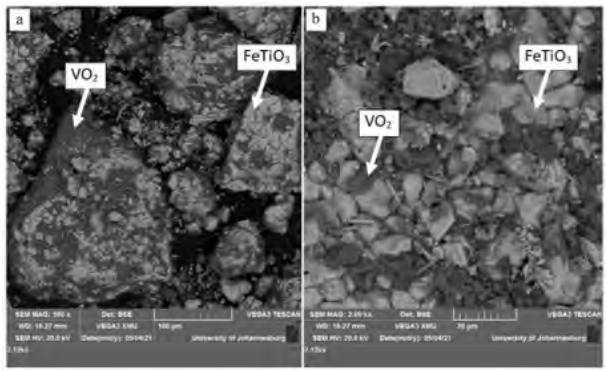

Figure 1. SEM micrographs of as-received roast-leach ferrovanadium residue under different magnifications (a) 500x and (b) 2000x.

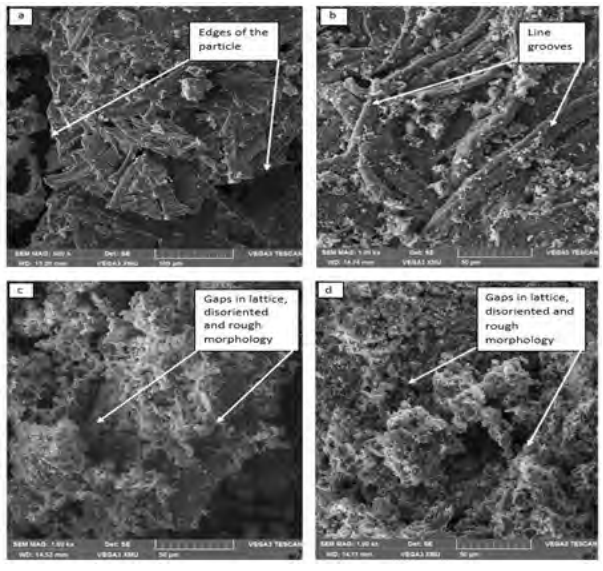

Figure 2. SEM electron micrographs of leach residue after leaching at different time intervals (a) 1 hour (b) 2 hours (c) 3 hours and (d) 4 hours.

Corresponding author: mbavhanevondo@gmail.com

CONTRAST OPTIMIZATION AIDED BY MACHINE LEARNING APPLIED TO VIRTUAL 4D-STEM IMAGES

D.G. Stroppa[1] and R. dos Reis[2]

[1]DECTRIS, Switzerland, [2]Department of Materials Science and Engineering, Northwestern University, USA

Scanning Transmission Electron Microscopy (STEM) has revolutionized imaging due to its high spatial resolution and easy interpretation due to varied contrast mechanisms, such as atomic number (Z) contrast at high-angle scattering and phase contrast from the bright-field disk. The enhanced flexibility in terms of scattering range detection in comparison with STEM is one of the reasons that led to the increased interest in 4D-STEM[1]. Supported by the recent evolution of pixelated detectors, 4D-STEM currently allows for the recording of the complete electron scattering range at speeds commensurate with traditional STEM experiments[2]. With the possibility of flexible reconstruction of virtual STEM images with arbitrary detector shapes, contrast optimization for sample regions with different scattering cross-sections is envisioned. This study delves into the optimization of contrast in virtual 4D-STEM images, employing both user-guided and machine-learning (ML) optimization approaches.

Reference samples from semiconductor devices and supported catalysts were measured with fast 4D-STEM under experimental conditions mirroring standard STEM imaging practices, with 1024×1024 scan positions and 10 us dwell time. The resultant datasets comprised 10^6 diffraction patterns with 96×96 pixels each, presenting a great challenge for manual contrast optimization due to the vast data volumes and nuanced contrast differences within the areas of the specimens. Figure 1 shows manual contrast optimization applied to virtual 4D-STEM images, serving as a foundational comparison point for our machine learning (ML)-aided methodology. The left panel reveals a virtual Bright Field (BF) STEM image, with an inset in the upper left corner illustrating a typical example of electron scattering and the application of a virtual mask overlay, highlighting the initial manual approach to contrast enhancement. The center panel demonstrates a virtual STEM image that has been collected utilizing an optimized annular mask, reflecting the outcomes of manual contrast optimization efforts. In the right panel, a line profile from these virtual images is presented, with indications of contrast levels, offering a quantitative perspective on the enhancements achieved through manual methods.

In this study, we also develop an innovative computational framework designed to automate the enhancement of contrast in similar regions within 4D-STEM data. Our methodology integrates the advanced deep learning architecture, ResNet101[3], for feature extraction, followed by Principal Component Analysis (PCA) for dimensionality reduction, and the application of hierarchical clustering techniques (Figure 2). The utilization of ResNet101, distinguished for its deep residual learning capabilities, is strategically chosen to adeptly capture the nuanced, hierarchical features inherent in 4D-STEM datasets, which are pivotal for identifying similarities across various regions. The initial phase of our analysis involves processing the 4D-STEM diffraction patterns through the ResNet101 model, which has been pre-trained on extensive image datasets.

This integrated approach—merging deep learning-based feature extraction, PCA, and hierarchical clustering—presents a robust strategy for automatically enhancing the contrast of similar regions within 4D-STEM data. By doing so, it significantly advances the automation of contrast enhancement, ensuring more efficient, accurate, and objective analysis of material structures. This methodology helps to streamline the process of identifying and enhancing similar regions within complex materials.

References:
1. C. Ophus, Microsc. Microanal. (2019) 563, 25.
2. M. Wu *et al.*, J. Phys. Mater. (2023) 6, 045008.
3. He, K., Zhang, X., Ren, S., & Sun, J. (2015). Deep Residual Learning for Image Recognition. CoRR

This work made use of the EPIC facility of Northwestern University's NUANCE Center, which has received support from the SHyNE Resource (NSF ECCS-2025633), the IIN, and Northwestern's MRSEC program (NSF DMR-2308691). This research was supported in part through the computational resources and staff contributions provided for the Quest high-performance computing facility at Northwestern University which is jointly supported by the Office of the Provost, the Office for Research, and Northwestern University Information Technology.

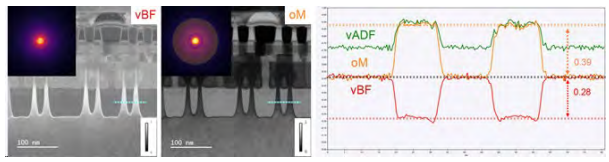

Figure 1. (left) Virtual BF STEM image, inset (upper left) with scattering example and virtual mask overlay. (center) Virtual STEM image collected with an optimized annular mask. (right) Line profile from virtual images with the relative contrast level calculated from normalized intensities.

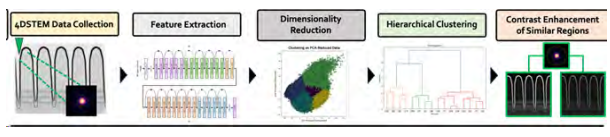

Figure 2. Workflow applied for the ML-based contrast optimization.

Corresponding author: daniel.stroppa@dectris.com

MEASURING GEOMETRICALLY NECESSARY DISLOCATION DENSITY IN THE SEM USING EBSD: TRUE OR FALSE?

R.D. Knutsen

Electron Microscope Unit and Centre for Materials Engineering, University of Cape Town

The study of EBSD in the SEM quickly developed into an advanced quantitative metallography tool towards the end of the last century and is now commonplace in microscopy laboratories. The determination of local crystal orientations in a sample many times larger than TEM foils enabled relatively accurate measurement of sub-grain and grain size, and benefited research focused on studying recovery, recrystallisation and microtexture. Nowadays, the improvements in angular and spatial resolution have broadened the characterisation capabilities of the EBSD technique and includes dislocation analysis which has mostly been restricted to TEM studies in the past. However, it remains an indirect technique unlike the direct visualisation of dislocations in the TEM, and hence interpretation of the EBSD data can be highly subjective. The present work explores some of the measurement and analysis parameters that need to be carefully considered when performing dislocation analysis of deformed polycrystalline metals.

It is important at the outset to consider the definition of geometrically necessary dislocations (GNDs) and to distinguish them from statistically stored dislocations (SSDs). Polycrystalline metals and alloys are plastically non-homogeneous. Gradients of deformation form in the microstructure and dislocations are stored to accommodate the deformation gradients. These are referred to as GNDs to distinguish them from the SSDs which accumulate and are responsible for normal 3-stage hardening[1]. As a result, the arrangement of GNDs gives rise to lattice curvature which can be measured using EBSD. The approximate density of the GNDs can be determined by calculating the weighted Burgers vector (WBV) using a sliding loop approach where, for every pixel in the EBSD map, a Burgers circuit is created and the WBV is calculated for that point[2]. Since the WBV is the sum of the density of intersections of dislocations with the EBSD map multiplied by the relevant Burgers vector, the GND density can be calculated by dividing the WBV value by the expected Burgers vector. In an ideal case where the angular measurements are precise, the WBV value would be an accurate indication of GND density, at least in as much as it is a 'weighted' value due to the 2-D nature of the EBSD dataset. But even a dislocation-free crystal could return WBV values if the inherent angular noise is not considered.

Figs. 1 and 2 represent an EBSD dataset acquired from an austenitic stainless steel that was deformed by cold extrusion. The map data was acquired with a Mira 3 SEM using the Oxford Aztec acquisition system at a beam step equal to 0.05µm. The index hit rate was 99.6%. Both figures illustrate heat maps of the WBV value distribution in the range 0-0.3µm/µm^2 for a 3×3 integral loop size. Fig.1 indicates the distribution for unfiltered data whereas Fig.2 is the same plot after the data is refined by applying a 1-pass Kuwahara filter[3]. Fig.2 defines a cellular structure associated with the arrangement of GNDs whilst Fig.1 shows some resemblance to Fig.2 but also includes random distribution of WBV values. The presentation in Fig.1 is misleading because the orientation noise associated with a highly dislocated microstructure can mask the true arrangement of GNDs. However, orientation averaging provided by the Kuwahara filter has minimised the noise to emphasise the GND arrangement which affords better interpretation of strain hardening behaviour. Aside from orientation averaging, other factors which influence the GND image include integral loop and beam step size, angular noise and pattern solution hit rate. Although the golden rule is to ensure that comparisons between maps are performed using the same analysis approach in each case, the EBSD dislocation analysis technique should focus on GND arrangements and not on GND density. Furthermore, analysis of the Burgers vector directions can add to the characterisation of the dislocation walls.

References
1. Ashby, M.F. (1970) Phil. Mag. 21, 399.
2. Wheeler, J. *et al* (2009) J. Microsc. 233, 482.
3. Humphreys, F.J. *et al* (2001) J. Microsc. 201, 50.

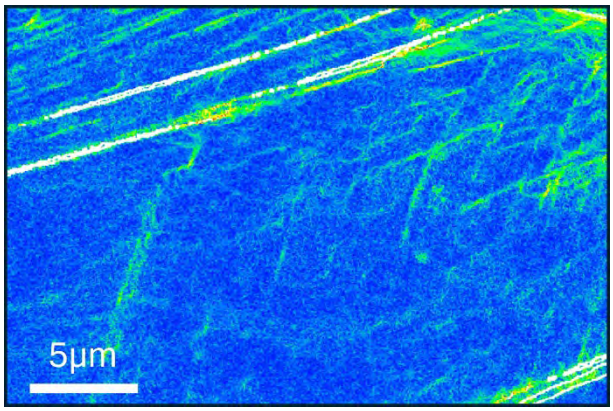

Figure 1. WBV distribution without data filtering.

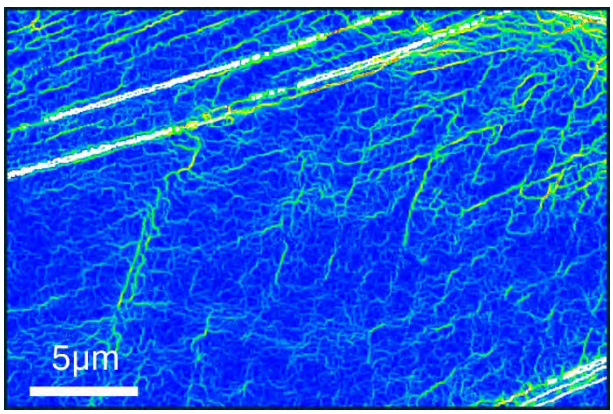

Figure 2. WBV distribution after applying a 1-pass Kuwahara filter.

Corresponding author: *Robert.Knutsen@uct.ac.za*

INVESTIGATING EFFECTS OF INTER-PASS TIME DURING HOT FINISH ROLLING ON THE TEXTURE EVOLUTION OF AA3104 CBS

N.A Chaole

Centre for Materials Engineering, Department of Mechanical Engineering, University of Cape Town, South Africa

When an aluminium strip is hot rolled the metal strip may experience varying inter-pass times along its length, leading to inhomogeneous microstructure evolution along the strip length. During the inter-pass time immediately after the high-temperature deformation event, the material experiences restoration where recovery and recrystallisation may occur to varying degrees thus affecting the evolution of the microstructure and the texture development. There is variability in the inter-pass times experienced by each point along the strip length between deformation events which results in inhomogeneous texture and corresponding material property anisotropy. This texture is associated with uneven earing formation during the beverage can manufacturing process[1-2]. Therefore, controlling the hot finish rolling process to achieve a balanced texture in the rolled strip is crucial. This study interrogates the microstructure and texture development associated with inter-pass time variability during simulated hot finish rolling of AA3104 CBS.

Multi-pass, high-temperature plane strain compression (PSC) tests were conducted on a Gleeble 3800 to simulate hot finish rolling, with varying inter-pass times between deformation events. Two scenarios were examined. In "Position A," a long inter-pass time t1 between passes P1 and P2, followed by a shorter inter-pass time t2 before P3. In "Position B," t1 is shorter and t2 is longer. $_1$ between passes P1 and P2, followed by a shorter inter-pass time t_2 before P3. In "Position B," t_1 is shorter and t_2 is longer. Note that the actual times are proprietary and are therefore not revealed here. A summary of the simulated process parameters is shown in Table 1. After the three-pass deformation, samples underwent recrystallization annealing (1 hour at 365°C) and were analyzed using SEM and EBSD in a Tescan Mira3. EBSD maps were used to evaluate grain size, grain boundary statistics, and crystallographic texture in both positions.

Fig.1 shows the EBSD inverse pole figure (IPF) maps and the corresponding Orientation Distribution Functions at for Position A [Fig. 1(a) and (b) respectively], and Position B [Fig1 (c) and (d) respectively]. The IPF maps indicate a fully recrystallized structure for both Positions A and B, but grain size variability is evident. The recrystallized grains in Fig. 1(a) are typically smaller than those in (c) and exhibit a bimodal distribution. There are larger recrystallized grains and many, small, recrystallized grains in clusters. While Position B exhibits a more uniform grain size distribution. This difference in grain size can be attributed to the extent of restoration through recovery that would have occurred in the inter-pass times and the resulting strain accumulation incurred after P3. This would be a sufficient difference in driving force for recrystallisation, with increased accumulation in the vicinity of intermetallic particles (IMPs), indicating particle-stimulated nucleation (PSN) and the bimodal grain distribution. EBSD texture analysis through the ODF sections in Fig 1. (b) and (c) for Position A and B respectively, indicate the presence of Cube texture in Position A, with a long-short inter-pass time combination and the dominance of the Goss texture component in Position B, with the short-long inter-pass time combination. Results also indicate Position A shows a higher intensity of Random texture, typically associated with PSN, when compared to Position B.

From the results obtained, the samples experience significant softening during the prolonged inter-pass times, reducing strain accumulation and thereby decreasing the driving force for recrystallization. As a result, there is a difference in the texture development. The interrogation of these results is still underway and further analyses are to be followed to quantify grain size distributions, grain boundary statistics, and the evolution of texture.

References:
1. Doherty, R. D. (1997) Prog. in Mat. Sci.42 (1–4), 39
2. Engler,O., Lochte, L., and Karhausen, K.F. (2005). *MSf.* 495, 555

Table 1. Processing parameters used for Gleeble PSC

	DEFORMATION P1	INTER-PASS 1	DEFORMATION P2	INTER-PASS 2	DEFORMATION P3
	Temp (°C)	Approx. Time	Temp (°C)	Approx. Time	Temp (°C)
Position A: Long - Short $P1 + t_1^A + P2 + t_2^A + P3$	380	Long (minutes)	330	Short (minutes)	300
Position B: Short - Long $P1 + t_1^B + P2 + t_2^B + P3$	380	Short (seconds)	330	Long (minutes)	300

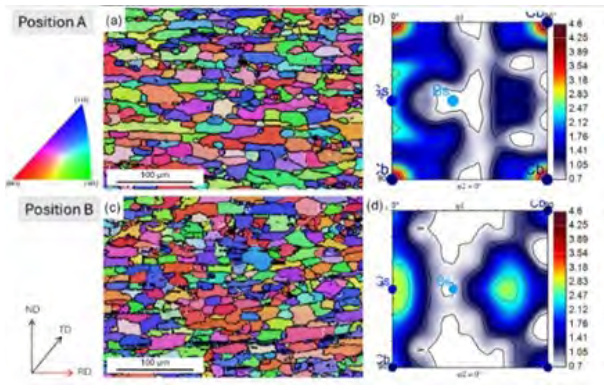

Figure 1. EBSD IPF maps and corresponding ODF for Position A (a) and (b) and Position B (c) and (d) after 3-pass deformation followed by a recrystallisation anneal

Corresponding author: chlnko001@myuct.ac.za

MORPHOLOGICAL AND PHASE STABILITY OF Cr-SiC COMPOSITES FOR HIGH-TEMPERATURE APPLICATIONS

C.E. Maepa[1], U. Dockrat[1], T.B. Mashabela[1], T.B Kadi[1], M.N. Mirzayev[2,3,4] and T.T. Thabethe[1]

[1]Department of Physics, University of Pretoria, [2]Institute of Radiation Problems, Azerbaijan National Academy of Sciences, Baku, [3]Scientific-Research Institute Geotecnological Problems of Oil, Gas and Chemistry, Azerbaijan State Oil and Industry University, Baku, [4] Western Caspian University, Baku

The interaction between chromium (Cr) and silicon carbide (SiC) through vacuum annealing reveals critical insights into material behavior at elevated temperatures. This is particularly important for nuclear applications where enhanced cladding materials are essential to improve fuel integrity, reduce oxidation, and ensure safety under extreme operational conditions[1]. Surface morphology and crystallography play critical roles in determining the functional properties of materials, such as diffusion resistance, thermal conductivity, and mechanical robustness, making their precise control essential for applications in high-stress and high-temperature environments[2]. Chromium-silicon carbide (Cr-SiC) composites have emerged as promising candidates for fuel cladding in nuclear reactors, demonstrating exceptional resistance to high temperatures, thermal stability, and the ability to form protective oxide layers[1].

In this study, ~250 nm Cr films were deposited on 6H-SiC substrates via e-beam deposition and annealed at 700°C, 800°C, and 900°C. Morphological changes were analyzed using AFM, supported by SEM, XRD, and EDX for structural and compositional insights.

The findings reveal that Cr deposition at room temperature produces a uniform layer, preserving the SiC structure. Annealing induces significant morphological transformations, including grain coarsening and surface roughening, which intensify with temperature. At 700 °C, crystallization occurs with modest grain growth and minimal oxide formation, as shown in Fig. 1 At 800 °C and 900 °C, pronounced grain agglomeration, carbide formation (Cr_3C_2, $Cr_{23}C_6$), and localized Cr-rich zones dominate, disrupting the SiC lattice, supported by XRD analysis in Fig. 2. Notably, Cr_3Si remains stable across all conditions, highlighting its resilience in the Cr-SiC system. These morphological changes align with a crystal growth model, where smaller grains dissolve and redeposit onto larger ones, driven by energy minimization[3]. The larger grains observed at higher temperatures further support this growth mechanism and are influenced by the oxide layer. Similar behavior has been reported in systems undergoing thermal treatment with oxide presence. These findings underscore the potential of Cr-SiC composites for high-temperature applications, provided morphological and structural stability are carefully managed. Under vacuum annealing, Cr thin films on SiC undergo morphological and crystallographic changes, enhancing our understanding of these materials for high-temperature applications. AFM indicated temperature-dependent surface changes from uniform granular morphology as-deposited to grain coarsening and roughening at high temperatures. The XRD confirm that surface geometry impacts phase stability, with Cr3Si remaining stable during annealing. Carbides and Cr-rich zones at 800 and 900 °C indicate structural integrity problems.

References:
1. Chu, S. and Majumdar, A. (2012) Nature 488, 294.
2. Wojteczko, K., *et al.* (2020) Compos. Theory Pract. 20, 17.
3. Thabethe, T.T. *et al.* (2018) Open Innov. Conf. 34-39

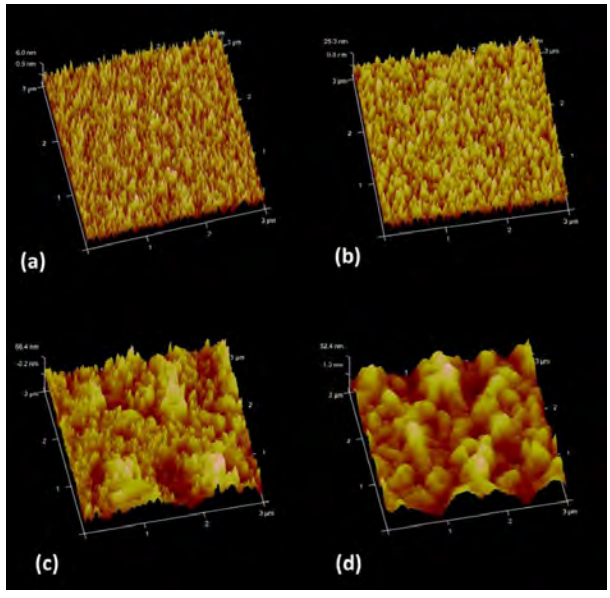

Figure 1. AFM images of Cr-SiC samples (a) before and after annealing at (b) 700°C, (c) 800°C and (d) 900°C for 2h.

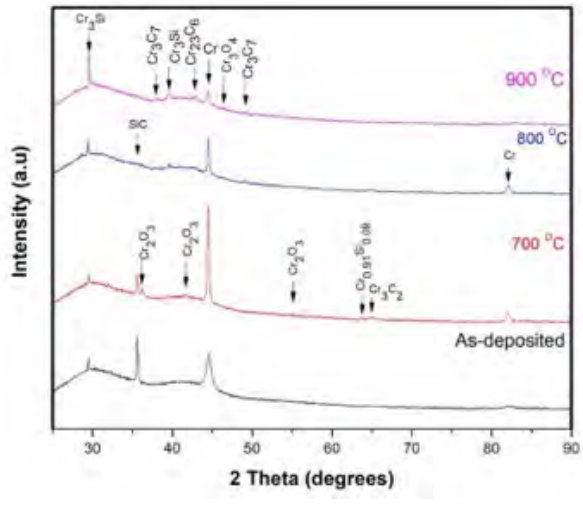

Figure 2. XRD Pattern of the Cr deposited on SiC, before and after annealing at 700°C - 900°C.

Corresponding author: charity.maepa@up.ac.za

PLASMONIC EFFECT OF GOLD NANOPARTICLES ON $NaYF_4$:Er,Yb UP-CONVERTING PHOSPHOR

T.M. Abdalkreem, H.C. Swart and R.E. Kroon

Department of Physics, University of the Free State, Bloemfontein, South Africa

Up-conversion phosphors absorb two or more low energy photons and emit one photon of higher energy than those absorbed[1]. This allows the emission of visible luminescence after excitation with an infrared laser. These phosphors have applications in biomedicine, temperature sensors and solid-state lasers[2]. Although some literature has reported the role of gold nanoparticle (Au NP) plasmonics in modifying up-converting phosphors, there is still no comprehensive methodology to assess a wide range of parameters, such as size or concentration of metal NPs and phosphor particles rapidly and efficiently, prompting a need for further experimentation that explores various parameters that can enhance the properties of up-conversion phosphors. In this study, the effect of different sizes of the Au NPs on $NaYF_4$:Er,Yb up-converting nanophosphor were investigated by making separate solutions of up-converting phosphor and Au NPs and then extracting the powder after solution mixing.

Up-converting $NaYF_4$:Er,Yb nanophosphor was prepared in solution using a high-temperature co-precipitation method using a Schleck line apparatus. The concentrations of dopants were chosen to be 2 mol% Er and 20 mol% Yb as these values had been reported in the literature to be the optimal concentrations[3]. Au NPs of different sizes were prepared separately using the reduction method. Mixing these solutions allows one to easily and rapidly evaluate the plasmonic effect of the size of Au NPs relative to the size of the nanophosphor particles on the performance of the up-converting phosphor, in contrast to other reported approaches where Au NPs are grown during (and as part of) the synthesis of the up-converting phosphor[4]. The structure of $NaYF_4$:Er,Yb with and without Au NPs was examined using X-ray powder diffraction (XRPD) for the extracted powder. The size and morphology of $NaYF_4$:Er,Yb with and without Au NPs were examined using a JEOL JEM-F200 high resolution transmission electron microscope (HRTEM), while elemental mapping in the TEM was carried out to confirm the constituent elements of the composite ($NaYF_4$:Er,Yb and Au NPs). Up-conversion emission for samples with and without Au NPs were recorded under 980 nm infrared laser excitation at room temperature using an Edinburgh Instruments FLS980 fluorescence spectrophotometer.

Fig. 1 shows a TEM micrograph of the $NaYF_4$:Er,Yb phosphor nanoparticles. It confirmed the spherical shape of these individual mono-disperse particles, while the inset in figure 1 illustrates the size distribution of the particles obtained by employing ImageJ software to measure the size of 50 particles. XRPD confirmed the crystallinity of the particles, and all the observed peaks were matched to the reference data for NaYF4 (JCPDS No 28-1192) and diffraction peaks from Au NPs were observed at the expected angles. Up-conversion emissions of samples with and without Au NPs gave the same form of emission spectra, with peaks located in the green and red wavelength regions, which are attributed to the f-f transitions of the Er^{3+} ions. In these trials, although the methodology of mixing solutions allowed one to vary the size of the Au NPs accurately, and independently, only a decrease in the up-conversion emission was measured compared to the sample without Au NPs.

In conclusion, we were able to evaluate the plasmonic effect of different sizes of Au NPs on up-conversion emission of $NaYF_4$:Er,Yb rapidly using a novel solution mixing technique. Although the emission intensity was not plasmonically enhanced during these trials, other conditions such as concentrations of Au NPs and annealing will be tested using this methodology.

References:
1. Rai, V.K. (2022) Upconverion Nanoparticles: From Fundamental to Applications. London, John Wiley & Sons.
2. Li, X., Zhang, F. and Zhao, D. (2015) Chem. Soc. Rev. 44(6), 1346.
3. Andresen, E. et al. (2023) Sci. Reports 13(1), 2288.
4. Park, W., Lu, D. and Ahn, S. (2015) Chem. Soc. Rev. 44(10), 2940.

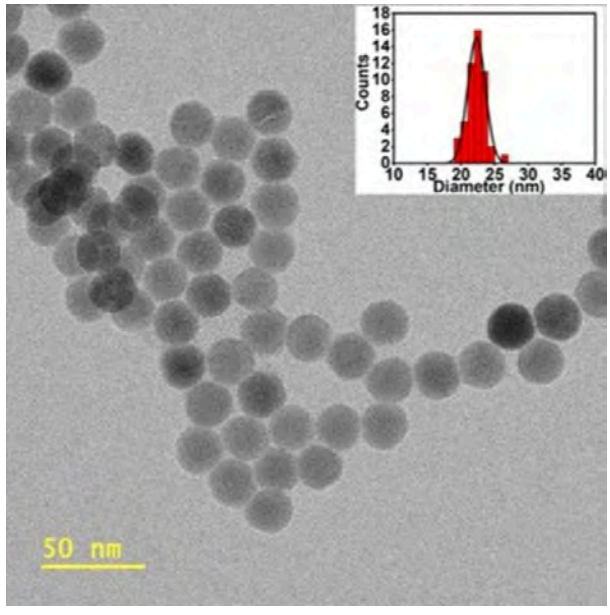

Figure 1. TEM micrographs of $NaYF_4$:Er,Yb up-converting nanophosphor particles. The inset is a histogram of the size distribution.

Corresponding author: talalph24@gmail.com

SYNERGISTIC ENHANCEMENT OF CO_2-EPOXIDE CYCLOADDITION: A STABLE $Ti_3C_2T_X$@ML-ZIF 9 (MXENE @ MOF) COMPOSITE CATALYST

Y.W. Abraha[1], D.E. Motaung[1], E.H.G. Langner[2] and H.C. Swart[1]

[1]Department of Physics, University of the Free State, Bloemfontein, [2]Department of Chemistry, University of the Free State, Bloemfontein

The integration of Metal-Organic Frameworks (MOFs) and MXenes into composite materials offers significant advantages for catalytic applications due to the unique and complementary properties of each component. MOFs are widely recognized for their high surface areas, tuneable porosity, and exceptional chemical versatility, making them ideal for gas capture and catalytic processes. Their porous structures allow for the efficient adsorption of gas molecules such as CO_2, while their modifiable chemical functionalities provide a platform for designing highly specific catalytic sites. MXenes, on the other hand, are two-dimensional materials known for their excellent electrical conductivity, high mechanical strength, and hydrophilic surface properties. MXenes also possess a rich surface chemistry, which can be tailored for catalysis, offering enhanced stability and electron transfer during catalytic reactions. Together, these features make the MOF-MXene composite an ideal candidate for advanced catalytic systems, particularly for applications in carbon capture and utilization (CCU) [1].

In this study, we present a novel composite catalyst comprising $Ti_3C_2T_x$ MXene integrated with a mixed-linker Zeolitic Imidazolate Framework (ML-ZIF-9), built with a cobalt metal center and a combination of 2-nitroimidazole and 2-methylimidazole linkers. The catalyst was designed to enhance the performance of CO_2-epoxide cycloaddition reactions, a process that converts CO_2 into valuable cyclic carbonates. These carbonates serve as building blocks for a variety of industrial applications, including polymers, pharmaceuticals, and fine chemicals.

The SEM images (Fig. 1, a) show that ML-ZIF-9 forms a spherical/rhombic dodecahedron-like morphology with an average particle size of 57 nm, which is typical for ZIFs with a sodalite topology. The hybrid materials (Fig. 1 b-d) show sheets of the $Ti_3C_2T_x$ MXene decorated with the ML-ZIF-9 nanoparticles, forming a hierarchical structure. The morphology of the ZIF in the hybrid material is similar to that observed in the SEM images of the MOF alone, reinforcing the structural stability of the ZIF morphology in the composite.

The ML-ZIF-9 alone exhibited a remarkable CO_2 uptake capacity of 99 cm^3g^{-1} and thermal stability up to 238°C. Upon incorporation of 10 wt% $Ti_3C_2T_x$ MXene, the composite demonstrated a significant enhancement in both thermal stability (up to 269°C) and catalytic activity, with a 15% increase in the cycloaddition reaction's turnover frequency (TOF), reaching 839 h^{-1}. The optimized composite (M9-T10) maintained excellent reusability, showing no significant loss in activity after five catalytic cycles (Fig. 2).

The integration of MXenes with MOFs in this composite addresses several limitations of standalone materials, including the degradation of MOF structures under catalytic conditions and the restacking issues observed in MXenes. This synergistic effect enhances the overall stability and activity of the catalyst, making it a promising candidate for industrial-scale CO_2 utilization processes.

In summary, $Ti_3C_2T_x$@ML-ZIF-9 offers a robust and efficient catalytic system for CCU applications, particularly in the production of cyclic carbonates from CO_2 and epoxides, providing a pathway for sustainable CO_2 conversion.

References:
1 Saini, H., Srinivasan, N., Šedajová, V., Majumder, M., Dubal, D.P., Otyepka, M., Zbořil, R., Kurra, N., Fischer, R.A. and Jayaramulu, K. (2021) ACS Nano. 15, 18742-18776.

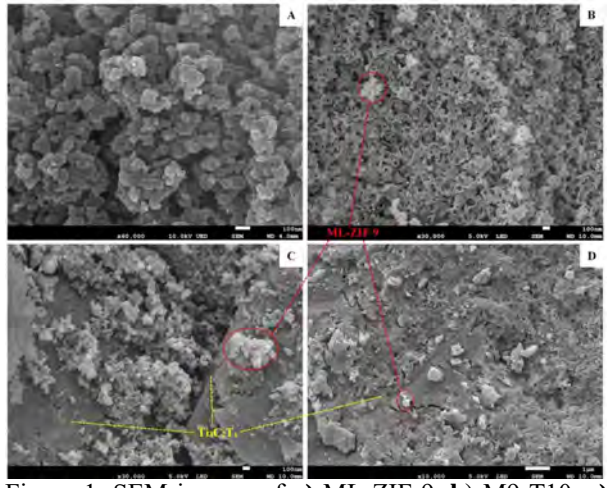

Figure 1. SEM images of **a)** ML-ZIF 9, **b**) M9-T10, **c)** M9-T20 and **d)** M9-T30.

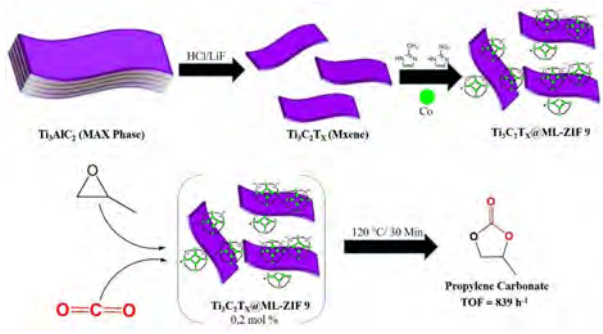

Figure 2. Synthesis and catalytic CCU application of $Ti_3C_2T_x$@ML-ZIF-9 composite.

Corresponding author: Abraha.Y@ufs.ac.za

MICROWAVE-SYNTHESIZED Zn_2SnO_4 NANOSTRUCTURES: EXPLORING THE EFFECT OF ANNEALING ON MORPHOLOGICAL AND STRUCTURAL PROPERTIES

G.M. Choeu[1], H.C. Swart[1] and K. Shingange[2]

[1]Department of Physics, University of the Free State, Bloemfontein, [2]Nanotechnology Innovation Centre (NIC), Advanced Materials Division, Mintek, Randburg

With the rapid growth in human population, the high emission level of waste products in air remains one of the most pressing issues faced by South Africans and all other nations around the globe. Consequently, this has urgently led to high demand of sensors that are reliable (for early detection of toxic, flammable, and explosive gases) affordable, and can operated at lower temperatures to reduce amount of power consumption. Over the past decades, semiconductor metal oxide (SMO)-based gas sensors are greatly investigated [1], among other sensors, because of their undeniable potential in gas sensing. However, there is still inadequate knowledge in development and testing of pure SMO-based gas sensors for accurate detection of specific gases. As a result, this work is invested in understanding the fabrication of pure stable zinc orthostannate (Zn_2SnO_4) sensing material and relate its properties such as surface morphology to sensing performance. Zn_2SnO_4 is a versatile material that has high electron mobility, excellent electrical conductivity, good thermal stability, and chemical stability in acids/bases as well as in organic solvents [2]. These properties make Zn_2SnO_4 suitable for a range of applications, including use in dye-sensitized solar cells, gas sensors, and photocatalysis [3, 4]. This current study presents the development of Zn_2SnO_4 nanostructures for their potential application in gas detection as a sensitive and selective sensing materials. The semiconductive Zn_2SnO_4 nanostructures were successfully synthesized by microwave-assisted hydrothermal synthesis approach at 150°C. Zinc nitrate hexahydrate [$Zn(NO_3)_2.6H_2O$] and tin tetrachloride pentahydrate [$SnCl_4.5H_2O$] as Zn^{2+} and Sn^{4+} precursors. The deionized water was used as a solvent and sodium hydroxide (NaOH) as a mineralizer to obtain pH value of 9. The purpose of this study was to investigate the effect of varying the annealing temperature (T_a, 600;700; and 800 °C) on the morphological properties and in-depth crystal structure of Zn_2SnO_4 nanostructures.

The surface morphology analysis was successfully carried out using the scanning electron microscopy (SEM) technique in which both lower magnified and enlarged micrographs were captured to reveal all the surface details. The micrographs depict the presence of nanoparticles with sizes that were increasing as the annealing temperature was rising. Notably, particles produced at 700 °C have slightly reduced in size, when compared to those produced at an annealing temperature of 600 °C. It has also been observed that nanoparticles produced after annealing at 800 °C consist of various sizes and have agglomerated such that they formed a sheet-like structure (Fig.1a). Energy-dispersive X-ray spectroscopy (EDS) was used to confirm the elemental composition of the synthesized Zn_2SnO_4 nanostructures. All samples revealed the presence of the three desired elements namely: zinc (Zn), tin (Sn) and oxygen (O) with equal ratios of atomic percentages as expected.

References:
1. Dey, A. (2018) Materials Science & Engineering B. 229, 206.
2. Tharsika, T., et al. (2015) *J Alloys Compd*. 618, 455–462.
3. Zhang, M., *et al*. (2020) Nano Energy. 71.
4. Yang, J., *et al*. (2017) Sens Actuators B Chem. 239, 857–864.

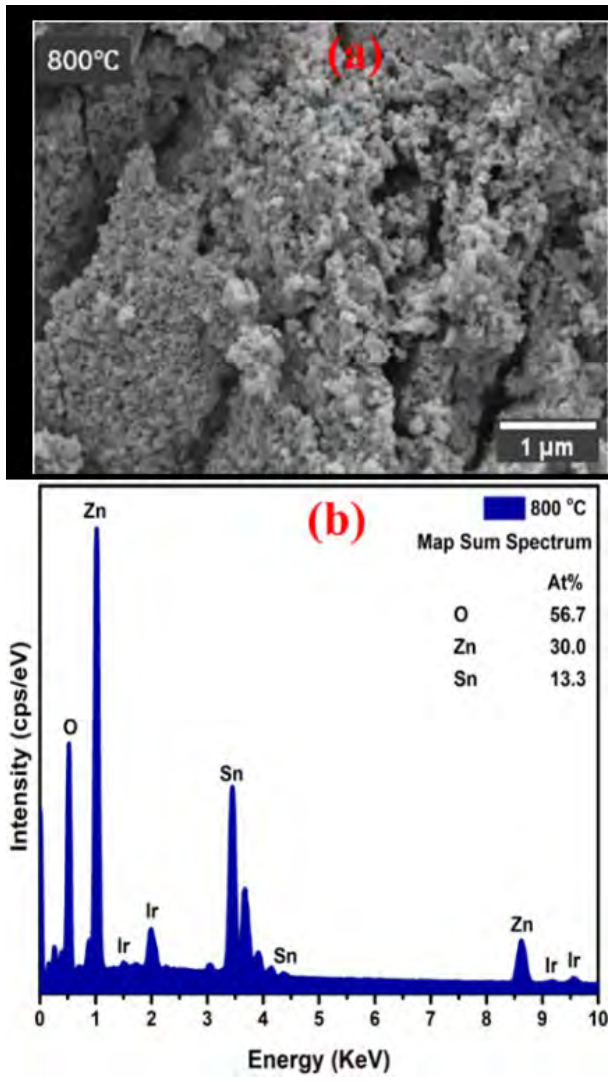

Figure 1. (a) SEM micrograph, and (b) EDS spectrum of Zn_2SnO_4 produced after annealing at 800 °.

Corresponding author: swartHC@ufs.ac.za

TEM AND XRD INVESTIGATION INTO THE STABILITY OF STRONTIUM-DOPED CSPBI3 PREPARED UNDER ATMOSPHERIC CONDITIONS.

M.M. Duvenhage[1], M.Y.A. Yagoub[1], E. Lee[1], H.C. Swart[1] and E. Coetsee[1]

[1]Physics Department, University of the Free State, Bloemfontein

Recently, there has been growing interest in iodide-rich inorganic lead halide perovskites for optoelectronic applications, largely because of their superior thermal stability compared to hybrid lead halide perovskites that contain organic ammonium cations [1]. Among these, cesium lead iodide ($CsPbI_3$) is particularly notable for its advantageous band gap of approximately 1.72 eV [2]. $CsPbI_3$ has crystalizes in three different forms: cubic (α phase), tetragonal (β phase) and orthorhombic (δ phase). When exposed to ambient conditions, α-$CsPbI_3$ undergoes an immediate phase transition to its orthorhombic polymorph (δ-CsPbI3). The α phase is the most desired phase as it shows the highest absorption [3]. However, the halide metal perovskites exhibit sensitivity to water, light and temperature and may be unstable, which is a main obstacle for practical applications [4]. Therefore, it is of vital importance to assess and improve the stability of the α-$CsPbI_3$. Metal-ion doping is one of the strategies employed for enhancing the α-$CsPbI_3$ stability and it has been proven to be an effective approach.

The metal-ion doping technique introduces different ions to modify the crystal structure of the perovskites through variation of the cation ionic radii in order to improve the stability of the perovskite materials. An example of such metal-ions is Sr^{2+} ion (118 pm), which has very close ionic radius to the Pb^{2+} (119 pm) but has more stable structure with better octahedral factor (μ), and Goldschmidt tolerance factor (t) [5].

In this study we have synthesized $CsPbI_3$:Sr^{2+} quantum dots using the ligand-assisted re-precipitation method. The structural and size analyses were made using X-ray diffraction (XRD) and high-resolution transmission electron microscopy (TEM). TEM confirmed the quantum dot nature of the as prepared samples with sized ranging from 3 -10 nm for the as prepared samples (see figure 1). The SAED pattern also confirms the crystallinity of the material as well as the nanosized particles. Over the span of the eight weeks, the particles start agglomerating and forming rod like structures. They are transforming from quantum dots into bulk particles. quantum dots into bulk particles. Simultaneously, the XRD results are showing a α phase for the as prepared samples that are transforming into the δ orthorhombic phase over time.

References:
1. Jin, H., Zeng, YJ., Steele, J.A. *et al.* (2024) NPG Asia Mater. 16, 24.
2. Xu, S., Libanori, A., Luo, G. and Chen, J. (2021) iScience, 24(3), 1.
3. Zhu, H., Hao, C., Li, X., Qi, Y. *et al*, (2023) J. Phys. Chem. C, 127, 18727.
4. Gong, X., Li, M., Shi, X., Ma, H., Wang, Z. and L. Liao, (2015) Adv. Funct. Mater. 25, 6671.
5. Wei, Y., Cheng, Z.and Lin, J. (2019), Chem. Soc. Rev. 48, 310.

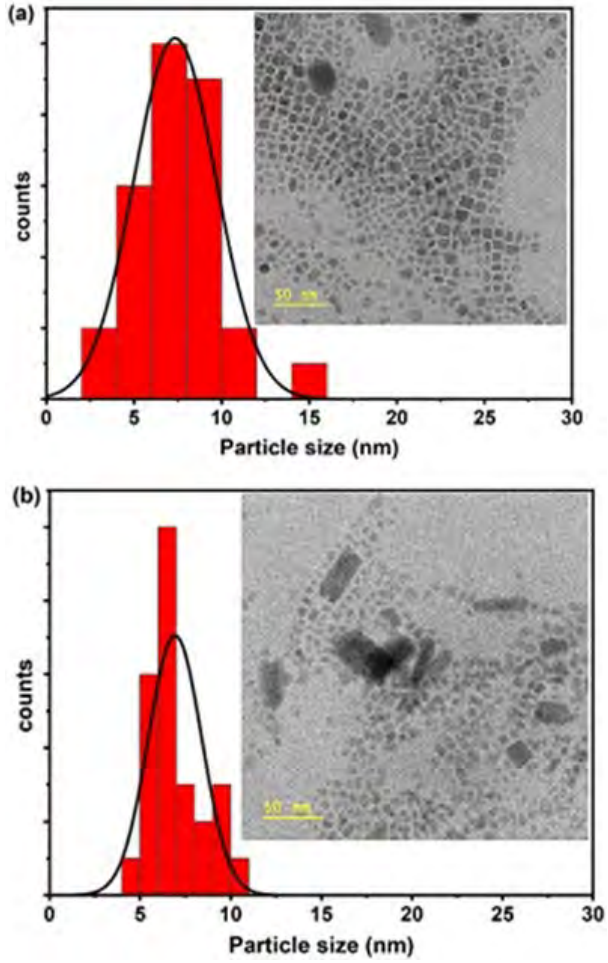

Figure 1. Size distribution histograms and the corresponding TEM images of quantum dots of (a) 0 % Sr and (b) 3 mol% Sr.

Corresponding author: duvenhagem@ufs.ac.za

PHASE TRANSFORMATION FROM α-Bi_2O_3 TO β-Bi_2O_3 FOR ENHANCED PHOTOCATALYTIC DEGRADATION OF RHODAMINE B

J. Divya, N.J. Shivaramu. and H.C. Swart

[1]Department of Physics, University of the Free State, Bloemfontein

A promising photocatalyst, the p-type semiconductor bismuth oxide (Bi_2O_3) is characterised by its simple composition, low toxicity, low cost, abundant polymorphism, relatively wide bandgap (2.2–2.9 eV), and visible-light activity[1]. Based on the literature[1,2], the tetragonal (β-Bi_2O_3) form demonstrated superfluous photocatalytic activity compared to monoclinic (α-Bi_2O_3). This can be attributed to its lower band gap (2.5 eV), activity in the visible light range, low recombination rate of photocarriers (e^- and h^+), larger surface area is due to smaller particle size[1]. In this study, we present the impact of ball milling and the time of ball milling on the crystal structure of α-Bi_2O_3, resulting in a phase change from α-Bi_2O_3 to β-Bi_2O_3. This study aimed to examine the structural, optical, and photocatalytic properties of Rhodamine B (RhB) degradation using UV-vis and a solar simulator for both α- and β-Bi_2O_3. The superior photocatalytic performance of β-Bi_2O_3 might be ascribed to its narrow band gap of 2.5 eV and large surface area in comparison to α-Bi_2O_3.

The Bi_2O_3 needles were prepared using the co-precipitation method, following the procedure outlined in our previous work[3]. The prepared Bi_2O_3 powders were then ball-milled for different durations.

Powder X-ray diffraction confirmed the structural conversion of α-Bi_2O_3 to β-Bi_2O_3 induced by high-energy vibrational ball milling. This conversion involves a phase transition and the formation of nanoparticles, with no observed amorphization. As the duration of ball milling approaches 120 minutes, the size of the crystallites decreases from 144 nm to 59 nm. This reduction is accompanied by a transformation in the morphology from needle-shaped α-Bi_2O_3 to a petal-like metastable β-Bi_2O_3 structure, as verified by field emission scanning electron microscopy (FE-SEM), as shown in Figure 1. A lattice fringe spacing of 0.314 nm, obtained from the high-resolution transmission electron microscopy (HR-TEM) image, closely matches the (201) planes of β-Bi_2O_3. The polycrystalline nature of the material is indicated by the selected-area electron diffraction (SAED) pattern, which reveals prominent (201) and (101) planes that strongly correspond to β-Bi_2O_3. A wide emission band with low intensity is observed in α-Bi_2O_3 within the wavelength range of 390 to 520 nm. In contrast, the β-Bi_2O_3 catalyst displays an intense wide band with a centre at 650 nm. The primary cause of the high-energy band (390-550 nm) is the recombination of photocarriers within the host material or the intra-ionic transitions of Bi^{3+}. The prominent band seen at 650 nm is attributed to the presence of oxygen vacancies[4]. Furthermore, the existence of oxygen vacancies has been verified by XPS and EPR investigations in this work and in previous publications[3,4]. The photocatalytic activity of α- and β-Bi_2O_3 was tested by decomposing RhB under UV-vis light and simulated sunlight (400-1100 nm). A decrease in RhB absorbance at 554 nm, due to breakdown of bathochromic bonds, indicated dye decolorization. Under UV-vis light and simulated sun light, peaks shifted from 554 nm to 503 nm, confirming N-de-ethylation process. The β-Bi_2O_3 exhibited high photocatalytic efficiency for RhB, achieving 97% degradation in about 75 minutes under UV-vis light. In contrast, α-Bi_2O_3 achieved only 55% degradation after 85 minutes. Under simulated sunlight, β-Bi_2O_3 showed superior performance with over 91% decolorization of RhB in 150 minutes, compared to 30% for α-Bi_2O_3. The difference in efficiency is attributed to variations in band gaps, BET surface area, and oxygen vacancies.

Compared to α-Bi_2O_3, metastable β-Bi_2O_3 exhibits significantly enhanced photocatalytic degradation of RhB under both UV-vis and simulated sunlight. The study's findings indicate that the semiconductor's surface area, band gap, and oxygen vacancies all play significant roles in the photocatalytic degradation of RhB.

References:
1. Kou, J., *et al.* (2017) Chem. Rev. 117, 1445.
2. Kanagaraj, T., *et al.* (2022) Environ. Res. 205, 112439.
3. Divya, J., *et al.* (2020) Appl. Surf. Sci. 520, 146294.
4. Yang, S., *et al.* (2022) J. Mater. Chem. C. 10, 8364.

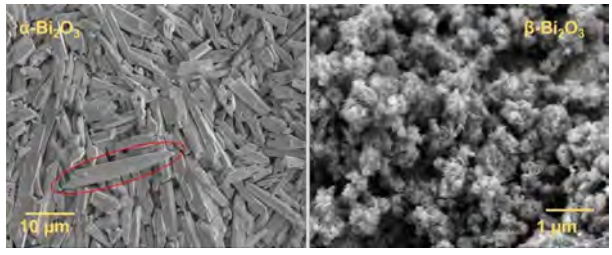

Figure 1. FE-SEM images of α- and β-Bi2O3 powders.$_2O_3$ powders.

Corresponding author: swarthc@ufs.ac.za

THICKNESS DETERMINATION OF $Al_xGa_{1-x}As$ EPILAYERS BY INFRARED SPECTROSCOPY AND SEM

J.A.A. Engelbrecht[1], M.E. Lee[1], J.R. Botha[2], S. Ngongo[1] and E.G. Minnaar[2]

[1]Centre for HRTEM, Nelson Mandela University, Gqeberha, [2]Physics department, Nelson Mandela University, Gqeberha

$Al_xGa_{1-x}As$ alloys are used for the fabrication of various opto-electric devices such as high-speed, high-frequency microwave devices[1], high electron mobility transistors[2] and quantum well infrared photodetectors[3]. The optical properties of these devices will be a function of various parameters such as the aluminium (Al) molar fraction (x) for the ternary intermetallic as well as the layer thickness. In this work a simple technique is described to determine the thickness of the $Al_xGa_{1-x}As$ epilayers by the application of Fourier Transform Infrared (FTIR) reflectance spectroscopy. The data from these spectra were used in obtaining the required optical parameters to solve the theoretical equations for the epilayer thickness as well as the Al molar fraction x. The calculated optical values were compared to the experimental values obtained by scanning electron microscopy (SEM).

$Al_xGa_{1-x}As$ epilayers with various Al mole fractions x were grown using organo-metallic vapour phase epitaxial (MOVPE) deposition on semi-insulating or silicon-doped GaAs substrates. A Bruker 80V FTIR/Raman spectrometer, fitted with a Pike 10Spec specular reflection attachment for near-normal incidence, was used to obtain reflectance spectra in the wavelength range 0.5 – 50 nm. FIB cross sections, produced in an FEI Helios 650 FIBSEM, were used to determine the experimental layer thickness.

The layer thickness is a function of wavelength (λ) and refractive index (n) and was calculated from the equation proposed by Reismann[4]. The data required to solve this equation was obtained from the FTIR reflectance spectrum (Fig.1) combined with two formulas from theoretical optical models proposed by Afromowitz[5] and Adachi[6]. The point of inflection for the reflectance spectrum was used to determine the value of the band gap energy E_g which was used to calculate the Al molar fraction x using the equations by Afromowitz[5]. The refractive index, which is a function of wavelength and molar fraction, was calculated from the two theoretical equations[5,6]. The epilayer thickness was calculated from the Reisman equation[8] applying the FTIR thickness fringes corresponding to the two wavelengths (λ_1 and λ_2) shown in figure 1 combined with the calculated values of the refractive index n(x,λ).

The experimental values for the $Al_xGa_{1-x}As$ layer thickness were determined by the measurement of the FIBSEM cross sections as shown in figure 2. The calculated and experimental values for the layer thickness are summarized in Table 1 and show that they are in good agreement.

References:
1. Adachi, S. (1992) Physical properties of III-V semi-conductor compounds, New York, John Wiley and Sons.
2. Lanka, T.R. and Panda, A.K. (2009) Int. J. Recent trends in Eng. 1, 186.
3. Billaha, A. and Das, M.K. (2017) Opto-Electronic Review 24,186.
4. Reizman, F. (1965) J. Appl. Phys. 36. 3804.
5. Afromowitz, M.A. (1974) Solid State Comm. 15, 59.
6. Adachi, S. (1985) J. Appl. Phys. 58, R1

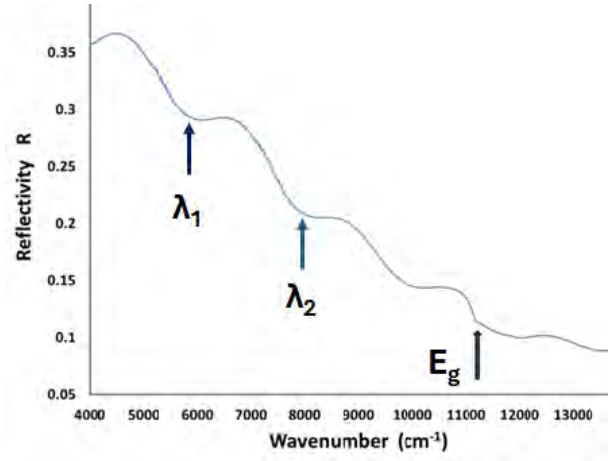

Figure 1. FTIR reflectance spectrum showing thickness fringes and point of inflection

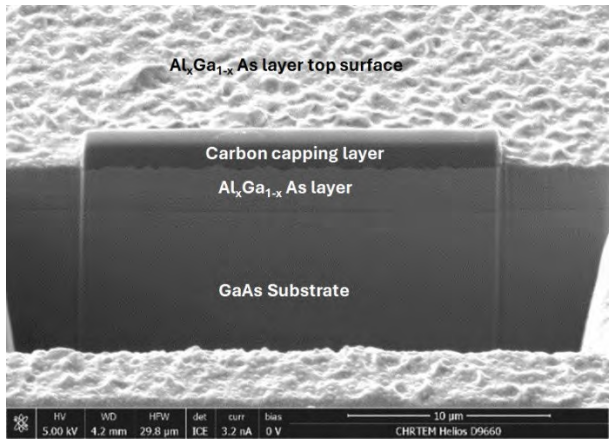

Figure 2. FIBSEM cross section showing the layer thickness

Table 1. Comparison of theoretical and measured for the $Al_xGa_{1-x}As$ layer thicknesses

E_g (eV)	x	Layer Thickness (µm)		
		Afromowitz	Adachi	Exp
1.70	0.22	2.63	2.62	2.68
1.81	0.31	1.06	1.06	1.08
1.90	0.38	1.08	1.07	1.11
2.14	0.93	0.66	0.66	0.70

Corresponding author: michael.lee@mandela.ac.za

THE SURFACE PROPERTIES OF PULSED LASER-DEPOSITED $Y_2O_3:Ho^{3+}$, Yb^{3+} THIN FILMS

V. Makumbane[1], M.Y.A. Yagoub[1], R.E. Kroon[1] and H.C. Swart[1]

[1]Department of Physics, University of the Free State, Bloemfontein

The demand for renewable energy sources such as solar energy has increased recently. However, according to the National Renewable Energy Laboratory solar cell efficiency chart, silicon solar cells have an efficiency of ~25%, indicating that the majority of the energy of solar light fails to generate electricity[1,2]. However, the application of upconversion (UC) transparent films on solar cells has been proposed as an efficient way to improve the solar cell's efficiency. The UC films can be applied at the back of a solar cell to convert the low-energy photons that are unabsorbed by solar cells into high-energy photons, thereby boosting the solar cell performance[3]. Considering UC films are coated at the back of the solar cells, the thickness of the film is essentially important, hence, in this work, the thickness effect on the surface properties of the $Y_2O_3:Ho^{3+}$, Yb^{3+} films were studied as possible upconverting layers for solar cell applications.

The preparation process of the $Y_{2-x-y}O_3:Ho_{x=0.005}$, $Yb_{y=0.05}$ powder is reported by Makumbane *et al.*[4]. 8 g powder was compressed for 30 minutes, and annealed for 8 hours at 1100 °C, to prepare the PLD target. Soda-lime glass substrates were cleaned using acetone, ethanol, and distilled water for 15 minutes, and dried using N_2 gas. The target and substrate were then placed inside the PLD chamber system, where the chamber was pumped down to a base pressure of $1.5x10^{-5}$ Torr and back-filled with an O_2 gas pressure of 50 mTorr. The target-to-substrate distance was kept constant at 4 cm, while the substrate temperature was kept at 350 °C. The laser pulses were varied from 10000-60000 at 39 mJ/pulse laser energy. The surface and elemental composition properties of the prepared films were investigated using a JEOL JSM-7800F scanning electron microscopy (SEM) equipped with an energy-dispersive X-ray spectrometer (EDS).

The surface morphology of the prepared film exhibited agglomerated, uniform particles, see Fig. 1(a). The particle agglomeration occurred during the deposition process, where bigger particles were formed when the produced particles started merging. The surface SEM image was further used to estimate the average particle size of the prepared film (inset), which was found to be 128 nm. Fig. 1(b) depicts the cross-sectional SEM view used to determine the thickness of the film, which was found to be 972 nm. Moreover, all the expected elements (Y, O, Yb, and Ho) in the film were observed through EDS analysis as shown in Fig. 1(c). The results suggested that the transparent films are good candidates for solar cell applications.

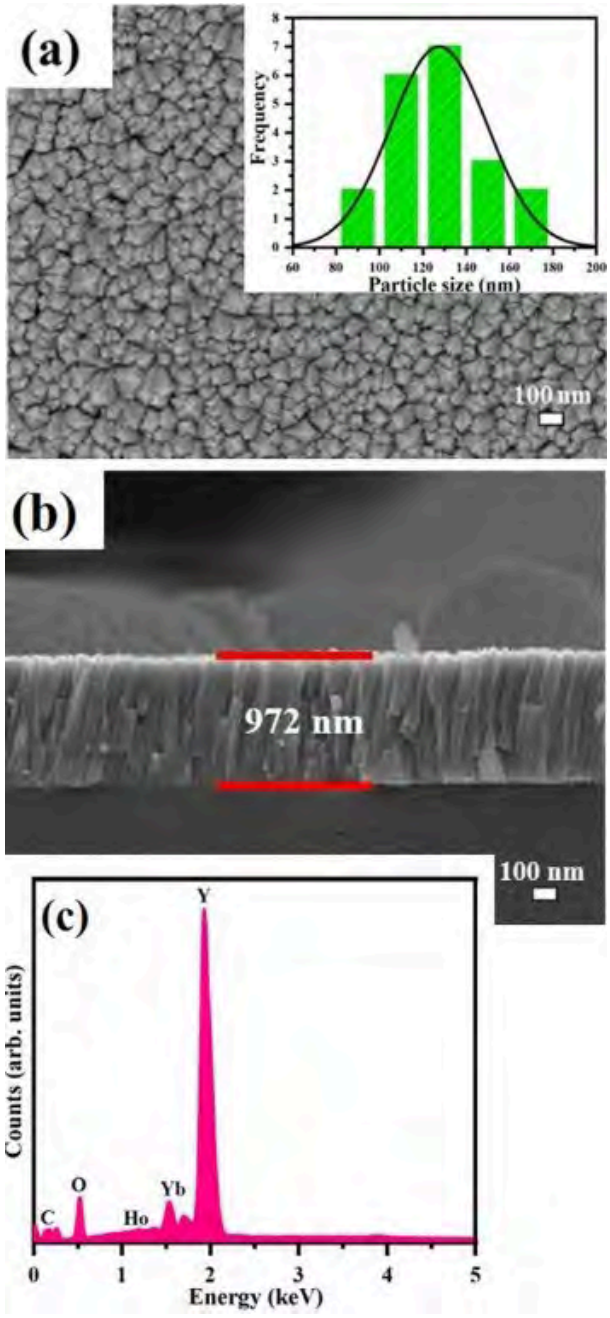

Figure 1. (a) Surface morphology and the corresponding particle distribution (inset), (b) cross-sectional SEM image, and (c) EDS spectrum of the 60000 laser pulse film.

Corresponding author: SwartHC@ufs.ac.za

References:
1. Strumpel *et al*. (2007) Sol. Energy Mater. Sol. Cells. 91, 238.
2. Bouajaj *et al*. (2016) Opt Mater. 52, 62.
3. Sark *et al*. (2013) Nanoscale Research Letters. 8, 81.
4. Makumbane *et al*. (2023) Crystals. 13, 1288.

THE MORPHOLOGY AND TEMPERATURE-DEPENDENT LUMINESCENCE OF $Ca_4(PO_4)_2O$ CO-DOPED Ce^{3+} AND Eu^{2+} PHOSPHORS

K.B. Morebodi[1], S.N. Ogugua[1] and H.C. Swart[1]

[1]Department of Physics, University of the Free State, Bloemfontein

Phosphor materials have been widely studied in both the science and industries for applications in biomedical imaging, solar cells, fingerprint detection, white light emitting diodes, temperature sensing[1], etc. In the field of luminescence, phosphor thermometry makes use of temperature sensitive powders, known as thermographic phosphors. These powders consist of a host material that is doped with a known percentage of rare earth ions that act as the activators[2]. The traditional contact temperature monitoring devices such as thermocouple and liquid-filled thermometers have slow response time and low temperature resolution[3]. The incorporation of thermographic dual emitting centres such as Ce^{3+} and Eu^{2+} in certain host materials are being studied across the globe[4]. However, limited studies are focused on phosphate-based phosphors that investigate morphology and use luminescent intensity ratio (LIR) technique, which has the capabilities of improving the response time, temperature resolution and stability of the optical thermometer.

In this study $Ca_4(PO_4)_2O$: xCe^{3+} and $Ca_4(PO_4)_2O$: 3% Ce^{3+}, yEu^{2+} phosphors were prepared using the solid-state method. The chemical compounds were calcium carbonate ($CaCO_3$), Di-ammonium hydrogen orthophosphate $(NH_4)_2HPO_4$, Cerium Oxide (CeO_2), and Europium oxide (Eu_2O_3). The effects of the doping and co-doping concentrations on the morphology and photoluminescence of the material were discussed. The LIR technique was used to study the thermographic ability of the obtained phosphor. A Joel JSM-7800F field emission scanning electron microscope (FE-SEM) coupled with energy dispersive X-ray spectroscopy (EDS) was used to analyse the morphology and chemical composition.

The micrograph in Fig 1 (a) show agglomerated chunks of irregular shaped materials. Fig.1 (b) shows an EDS spectrum with the presence of Calcium (Ca), Carbon (C), Phosphorous (P), Oxygen (O), Cerium (Ce), Europium (Eu) and Iridium (Ir). The presence of all these elements in Fig. 1 (b) eludes that they were successfully incorporated into the material. The C that is found may be due to the slight remainder of the carbonate from the precursor, that was not fully removed as a byproduct during synthesis. The Ir was used to coat the powder to prevent charging. The quantum yield (QY) of $Ca_4(PO_4)_2O$: 3% Ce^{3+} was 43%, while the QY of the co-doped $Ca_4(PO_4)_2O$: 3% Ce^{3+}, y Eu^{2+} (where y = 0.1, 0.3, 0.5 and 0.7 %) phosphors were 24, 13, 12 and 10 % respectively.

The lifetime decay, absolute temperature sensitivity and repeatability studies indicated that $Ca_4(PO_4)_2O$: 3% Ce^{3+}, 0.7 % Eu^{2+} is a promising candidate for a non-contact optical temperature sensor.

References:
1. Nair, G.B., Swart, H.C. and Dhoble, S.J. (2020) Progress in Material Science 109, 100622.
2. Ogugua, S.N., *et al*. (2024) Dalton Trans 53(10), 4551.
3. Li, C., *et al*. (2020) J. Alloys and Compd. 838, 155675.
4. Zhao, J., Sun, X. and Wang, Z. (2018) Chem. Phys. Lett. 691, 68.

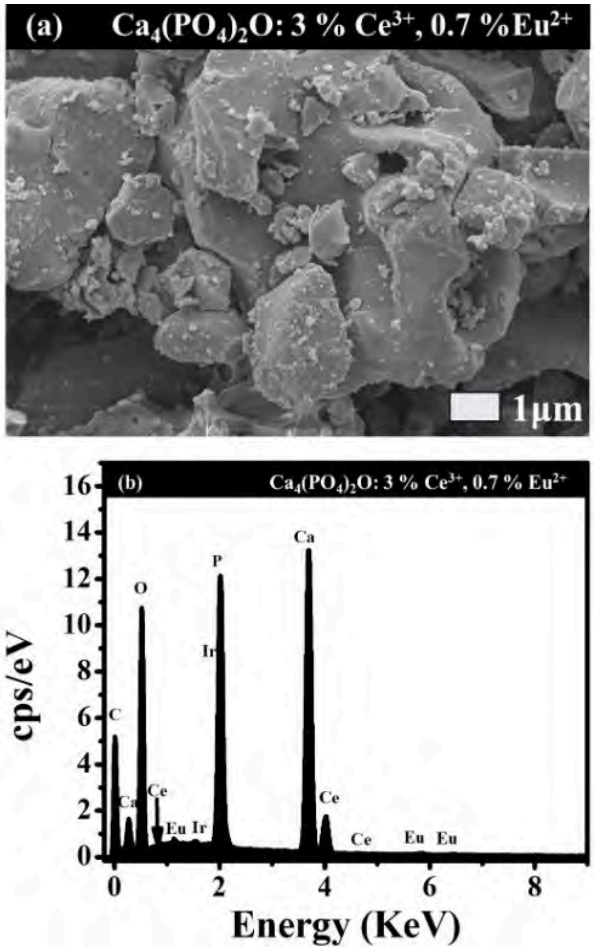

Figure 1. Figure 1. (a) FE-SEM micrograph and (b) EDS spectrum of $Ca_4(PO_4)_2O$: 3% Ce^{3+}, 0.7 % Eu^{2+} phosphor

Corresponding author: SwartHC@ufs.ac.za

CHARACTERISATION OF TiZrN IRRADIATED WITH HELIUM AND SWIFT HEAVY IONS

L.Z. Mrwetyana[1], A. Janse van Vuuren [1] and S. Ngongo[1]

[1]Centre for HRTEM, Department of Physics, Nelson Mandela University, Gqeberha

Ternary transition metal nitride (TMN) thin films are widely used as protective coatings in nuclear applications due to their excellent properties such as high hardness, good wear and corrosion resistance. TiZrN is one of the ceramics considered as a candidate inert matrix fuel host for Gen IV reactors [1]. TiZrN will be subject to irradiation by alpha particles and fission fragments. Nanostructured coatings are suggested to have greater tolerance to irradiation because of increased volume of grain boundaries, which serve as effective sinks for radiation-induced defects [2].

In this study, the microstructure of TiZrN implanted with low energy helium ions and irradiated with SHI xenon ions to simulate radiation damage resulting from alpha particles and fission fragment bombardment.

Nanocrystalline TiZrN layers (~1µm thickness) were synthesised via vacuum arc-vapour deposition. These layers were first irradiated with 30keV helium (He) ions at a fluence of 5 $\times 10^{16} cm^{-2}$ and subsequently irradiated with 167MeV xenon (Xe) ions to a fluence of 8.03 $\times 10^{13} cm^{-2}$. All samples were annealed at 600 °C for 1 hour in an argon atmosphere. Transmission electron microscopy (TEM) lamellae were produced using a Helios NanoLab focused ion beam (FIB). The lamellae were investigated using a JEOL 2100 LaB_6 TEM operated at 200 keV.

Fig. 1 is a TEM bright field (BF) image of as-deposited nanocrystalline TiZrN layer synthesised via vacuum arc-vapour deposition method. In Fig. 2, the layer implanted with He shows helium-induced bubbles near the surface (red arrows). There was no mitigation of helium induced radiation damage after Xe irradiation (white arrows). This effect is likely due to diffusion and agglomeration of He in the near surface. The microstructure of TiZrN layer reveals no effects from SHI irradiation, indicating either very high radiation tolerance or possible rapid recrystallisation of the material. No recovery of induced radiation damage is observed after annealing in any of the samples.

Helium ion irradiation of ceramic materials induce defects such as helium bubbles as observed by TEM. Swift heavy ion (SHI) irradiation is known to form latent ion tracks in certain susceptible materials and has previously been found to mitigate He induced radiation damage [2]. Earlier reports reveal that the microstructure of nanocrystalline ceramic layers is unaffected by SHI irradiation [2]. However, there is no suppression of helium-induced radiation damage from SHI irradiation. Literature suggests that this may be likely due to the high helium fluence. [2].

References:
1. Uglov V.V. *et al*., (2015) *Nucl. Inst. Meth. Phys. Res. B* 354, 269.
2. Janse van Vuuren A. *et al*., (2014) *Nucl. Inst. Meth. Phys. Res. B* 326, 19.

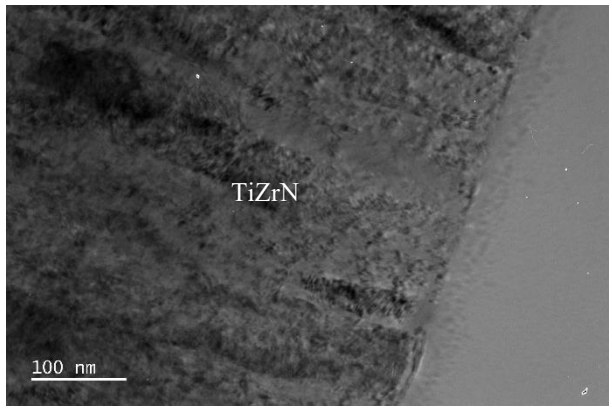

Figure 1. TEM BF micrograph of as-deposited TiZrN.

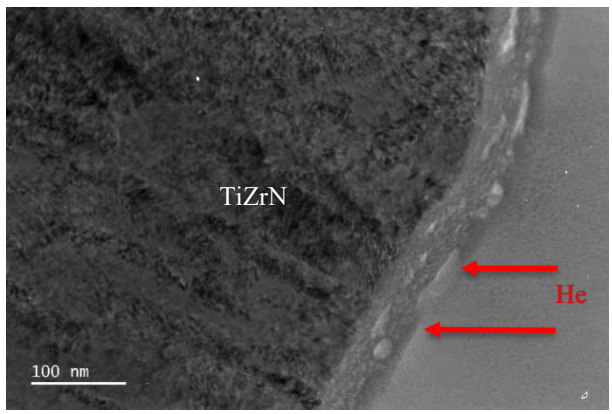

Figure 2. TEM BF micrograph of 30 keV He as-implanted to a fluence of 5 $\times 10^{16}$ cm^{-2}.

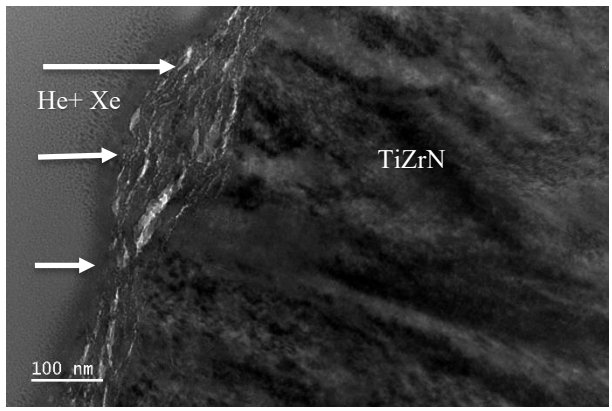

Figure 3. TEM BF micrograph of He implanted and subsequent 1670MeV Xe ion irradiation to a fluence of 8.03 $\times 10^{13}$ cm^{-2}.

Corresponding author: s21347824@mandela.ac.za

EFFECT OF ANNEALING TEMPERATURE ON BARIUM ZIRCONATE ($BaZrO_3$) PEROVSKITES NANOPARTICLES PREPARED BY SOL-GEL METHOD

Q. Nkomo[1], K.G. Tshabalala[1], H.C. Swart[2] and S.J. motloung[1]

[1]Department of Physics, University of the Free State, Qwa Qwa Campus, Phuthaditjhaba, [2] Department of Physics, University of the Free State, Bloemfontein

The large quality of human life across the globe depends on a large degree of energy, and this is threatened by insufficient fossil fuels that are required to generate energy. Over past few decades, South Africa has been challenged with tremendously high-power cuts, thus, affecting the economic growth of the country. However, this can be avoided by using renewable energy resources (that are environmentally friendly, cost-effective, and highly efficient) as an alternative way to revolutionize the future. Among different types of luminescent materials, perovskite-based oxides have been greatly investigated due to their amazing optical properties, superconductor, and their fundamental contribution of the phase transitions for applications in lighting and displays. However, the luminescence performance of pure perovskite-based oxides is scarcely reported, hence, this work is invested in comprehending the synthesis of pure barium zirconate ($BaZrO_3$) material and relate its properties such as surface morphology to luminescence performance.

$BaZrO_3$ is a fascinating luminescent material due to its prominent properties that it acquires such as high dielectric constant, low thermal expansion, chemical stability, high melting point (~3000 K) and wide band gap (~3.8–5.0 eV)[1]. The semiconductive $BaZrO_3$ nanostructures were successfully synthesized by a cheap and environmental friendly sol-gel synthesis method at 80ºC. Barium nitrate [Ba $(NO_3)_2$] and zirconium (IV) acetate hydroxide [$Zr_3C_{12}H_{36}O_{12}$] as Ba^{2+} and Zr^{4+} precursors. The deionized water was used as a solvent and citric acid ($C_6H_8O_7$) as a chelating agent to bind cations. The purpose of this study was to investigate the effect of varying the annealing temperature (T_a, 600;800; 1000 and 1200 ^{O}C) on the morphological properties and in-depth crystal structure of $BaZrO_3$ nanostructures.

The surface morphology analysis was successfully performed using the scanning electron microscopy (SEM) technique of $BaZrO_3$ nanoparticles annealed at 1000 and 1200℃. At both annealing temperatures the features revealed the presence of spherical-like nanoparticles with voids in between them. The temperature dependent-particle size effect was also depicted in which the agglomeration has increased with an increase in annealing temperature. Thus, giving rise to formation of bigger nanoparticles. The energy-dispersive X-ray spectroscopy (EDS) analysis confirmed the presence of all desired elements in all samples, and which are barium (Ba), zirconium (Zr), and oxygen (O).

References:
1. Orak, I., et al. (2022) Sensors and Actuators A: Physical. 337. 113413.

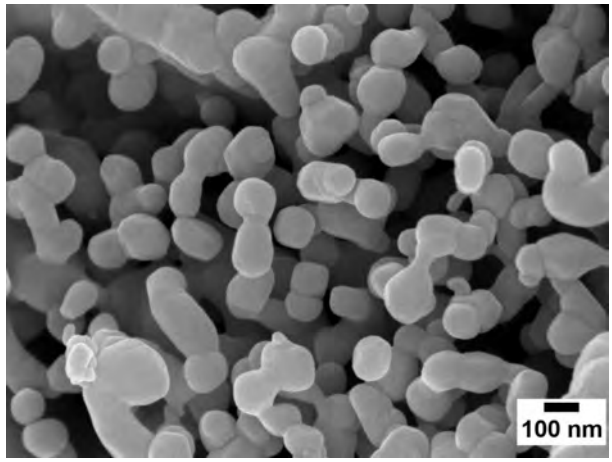

Figure 1. SEM image of $BaZrO_3$ produced after annealing at 1000 °C produced after annealing at 1000 ˚C

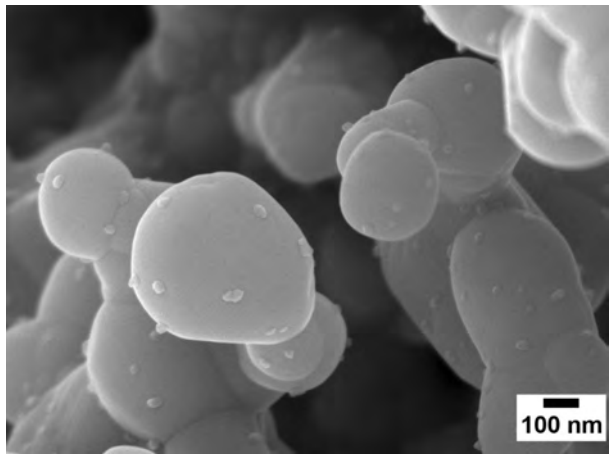

Figure 2. SEM image of $BaZrO_3$ produced after annealing at 1200 ˚C

Corresponding author: 2015185297@ufs4life.ac.za

STRUCTURAL CORRELATION TOWARDS HIGH-SENSITIVE SENSOR BASED ON In_2O_3-Co_3O_4 INTEGRATED WITH N-TYPE-SMOs FOR ACETONE DETECTION

K.L. Morulane[1], Z.P. Tshabalala[1], H.C. Swart[1] and D.E. Motaung[1]

[1]Department of Physics, University of the Free State, Bloemfontein

Detection and monitoring of volatile gases are vital for the safety of human health, and the domestic and industrial environment. Metal oxide semiconductors for gas sensing are compounds comprised of metal and oxygen molecules within their structures revealing high surface reactivity, electrical, optical, and thermal characteristics[1]. They can interact with volatile organic compounds (VOCs) such as acetone, and ethanol, hence they are utilised in medical and diagnostic fields as diabetes biomarkers for the detection of acetone in human breath.

Diabetic patients have acetone concentrations of more than 1.8 ppm, whereas people with no diabetes have a concentration of 0.3 ppm to 0.9 ppm[2]. Due to increased morbidity and mortality rates of metabolic disease (i.e., diabetes), portable n-p-n SMO-based acetone sensor measurements are considered to detect and monitor low acetone concentrations. To attain high sensitivity, good selectivity, high stability, low limit of detection, rapid response, and recovery times, surface modification of np In_2O_3-Co_3O_4 incorporated with potential n-type SMOs such as CeO_2, SnO_2, ZnO, and ZrO_2 was obtained to improve the sensing performance of the sensor.

The fabricated In-Co-Ce, In-Co-Sn, In-Co-Zn, and In-Co-Zr nanostructures were prepared using hydrothermal method. Four separate beakers were filled with enough chloride salt precursors in 100 ml of distilled water, followed by an equivalent amount of sodium carbonate as a reducing agent. The solutions were stirred using magnetic stirrers for 30 minutes at the speed of 800 rpm. The uniform solution was obtained and then transferred to autoclave reactors, which were then heated in the oven at 160°C for 4 hours and 30 minutes. To eliminate impurities, the obtained solutions were centrifuged and washed numerous times with 80 ml and 20 ml of distilled water and ethanol, respectively. The final products were dried at 80°C for 12 hours and calcined at 450°C for 4 hours.

Morphological properties of prepared samples were examined using JEOL, JSM-7800F scanning electron microscopy (SEM). Fig. 1(a-d) illustrates the high-magnification micrographs of various arrangements of developed nanostructures. All obtained morphologies reveal complex nanostructures that are non-uniform due to different chemical compositions. These composites of various shapes enhance the active sites, allowing interaction between the sensing surface and analyte gas molecules. The corresponding EDS spectra of prepared samples were conducted to verify the existence of In, Co, Ce, Sn, Zn, Zr, and O elements. The observed Na originates from the reducing agent used when preparing samples. Additionally, Ir was detected which originates from the sputtering coating process.

The prepared sensors were tested toward various VOCs, such as acetone, benzene, ethanol, and methanol. The In-Co-Zn-based sensor exhibited a remarkable response of 1.58 compared to other sensors towards 2.3 ppm acetone at 150°C as an optimized operational temperature due to high surface reactivity. This improved response is assigned to the surface defects that manifested as oxygen vacancies in the In-Co-Zn nanostructure. Moreover, the In-Co-Zn sensor exhibited an average response of 3.77 in humid conditions compared to a 1.58 response in dry air. This behaviour might be due to OH^- and H^+ groups comprised in H_2O acting as catalysts. Moreover, the sensor demonstrated a good long-term stability towards 2.3 ppm acetone for 30 days.

References:

1. Zhang, J., Qin, D., and Xie, C. (2017), Royal Society of Chemistry, 19, 6313-6329.
2. Sharma, B., Sharma, A., and Myung, J., (2021), Sensors and Actuators B: Chemical, 349, 130733.

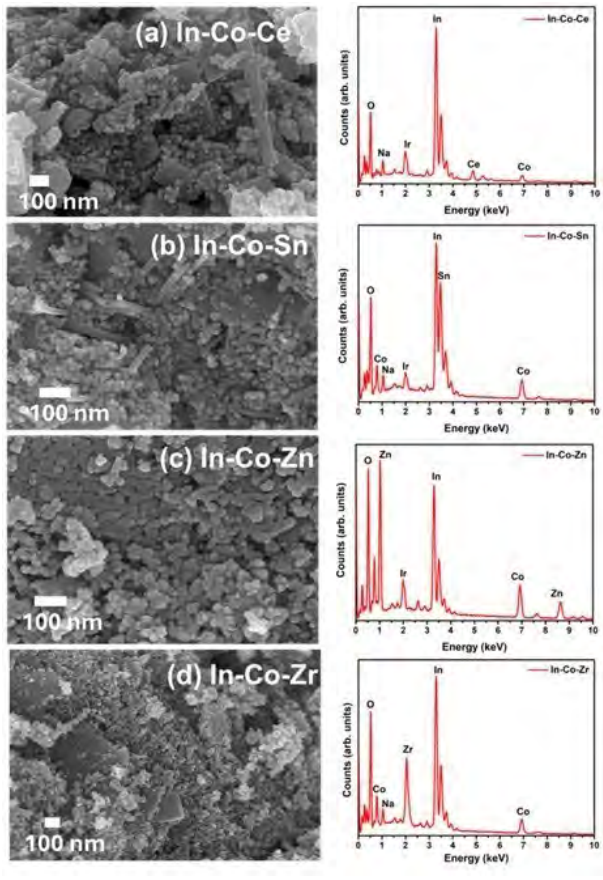

Figure 1. SEM images and corresponding EDS spectra of (a) In-Co-Ce, (b) In-Co-Sn, (c) In-Co-Zn, and (d) In-Co-Zr nanostructures.

Corresponding author: katlegolloyd54@gmail.com

INFLUENCE OF SYNTHESIS METHOD ON MICROSTRUCTURE AND LUMINESCENCE OF $La_2Zr_2O_7$:Bi,Tb PYROCHLORE PHOSPHORS

B.V. Naveen Kumar[1] and R.E. Kroon[1]

[1]Department of Physics, University of the Free State, Bloemfontein

Pyrochlore materials, particularly lanthanum zirconate ($La_2Zr_2O_7$), exhibit unique luminescent properties when doped with elements such as Bi^{3+} and Tb^{3+}. These dopants enhance emission intensity through energy transfer mechanisms and crystal field modifications, making $La_2Zr_2O_7$ an attractive candidate for various applications[1]. In this study, we employed four distinct synthesis techniques namely combustion, co-precipitation, microwave hydrothermal, and polyol methods to fabricate $La_2Zr_2O_7$:Bi,Tb phosphor. Advanced microscopy techniques, such as field emission scanning electron microscopy (FE-SEM) equipped with energy dispersive X-ray spectroscopy (EDS) was utilized to evaluate the morphological characteristics of the synthesized phosphors. These techniques provided detailed insights into grain morphology, particle size distribution and elemental compositions all of which significantly impact the optical properties of the materials. The optical properties were further characterized using photoluminescence spectroscopy to assess the influence of synthesis methods on emission efficiency and spectral tuning.

The FE-SEM images and EDS data were acquired using a JSM-7800F JEOL field emission scanning electron microscope with a magnification of 30,000 times for all the samples. The particle size distribution was analyzed with ImageJ, an open-source software. The morphological characteristics of $La_2Zr_2O_7$:Bi,Tb samples were thoroughly examined using field emission scanning electron microscopy, as shown in Figure 1. The FE-SEM images revealed distinct differences in particle morphology based on the synthesis method employed. The samples synthesized via the combustion method (Fig. 1(a)) exhibited non-uniform agglomerated granules with a larger particle size. In contrast, the samples prepared by the co-precipitation and microwave hydrothermal methods (Fig. 1(b & c)) displayed irregular polygon-like morphology with smaller size, whereas the polyol method produced samples with uneven spherical particles of moderate size (Fig. 1(d)) compared to the other techniques. The combustion synthesis was found to yield larger particles due to the exothermic nature of the process, which releases a significant volume of gases during the reaction, influencing the final powder characteristics[2]. The particle size distribution was quantitatively assessed confirming that combustion-synthesized samples had the largest particle size compared to other samples. Further, EDS was also employed to verify the elemental composition of the pure, doped, and co-doped samples across the different synthesis methods. The EDS spectra confirmed the presence of La, Zr, O, Bi, and Tb in appropriate proportions, consistent with the intended doping levels. However, an interesting result was observed in the co-doped samples synthesized using the co-precipitation and microwave hydrothermal methods, where a minor amount of Si contamination was detected. This contamination likely resulted from the etching of glassware by the ammonia alkali solution, which serves as a precipitating agent in these processes[3].

The photoluminescence emission spectra of $La_2Zr_2O_7$:Bi,Tb phosphors demonstrated that upon excitation at 310 nm, a broad emission peak between 435 nm and 500 nm was observed due to electronic transition from $^3P_1 \rightarrow {}^1S_0$ of Bi^{3+} ions, along with a characteristic Tb^{3+} emission at 542 nm ($^5D_4 \rightarrow {}^7F_5$). This indicates an effective energy transfer between Bi^{3+} and Tb^{3+} ions in the co-doped samples. While the emission profiles across all samples were similar, the sample synthesized via microwave hydrothermal method exhibited the maximum relative photoluminescence emission intensity. This enhanced luminescence is attributed to superior crystallinity and reduced defect density, which are crucial for strong luminescence[4]. However, despite its superior luminescence, the microwave hydrothermal method introduced unintentional Si contamination. Therefore, the combustion method emerges as the next best suitable synthesis technique for fabricating $La_2Zr_2O_7$:Bi,Tb phosphors.

References:
1. A.P. Anantharaman, H.P. Dasari (2021), Ceram. Int. 47 (4), 4367.
2. R. Ianoş, S. Borcănescu, R. Lazău (2014), Chem. Eng. J, 240, 260.
3. H. Kaigawa, K.Y. Koji Yamamoto, Y.S. Yasuhiro Shigematsu (1994), Jpn. J Appl. Phys. 33, 4080.
4. Liang P. (2019), RSC Adv. 9 (2), 891.

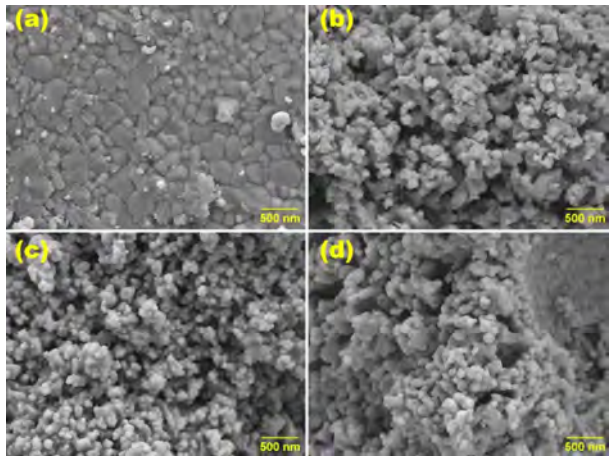

Figure 1. FE-SEM images of the $La_2Zr_2O_7$:Bi,Tb samples prepared by (a) combustion method, (b) co-precipitation method, (c) microwave hydrothermal method and (d) polyol method.

Corresponding author: Basina.VNK@ufs.ac.za

ZEOLITE-ENCAPSULATED SINGLE Pt ATOMS FOR HYDROCRACKING

T. Ntlebi[1] and P.J. Kooyman[1]

[1]The Catalysis Institute, Department of Chemical Engineering, University of Cape Town

Single-atom catalysts represent a promising approach for maximizing catalytic efficiency due to their unique ability to provide a uniform dispersion[1]. Platinum (Pt) supported on MFI zeolites has emerged as a highly effective catalyst for hydrocracking Fischer-Tropsch wax, primarily due to its high catalytic activity in these reactions[2]. It is hypothesized that the presence of well-dispersed single Pt atoms within the MFI zeolite framework can substantially enhance catalytic activity in hydrocracking processes.

Traditionally, the incorporation of Pt into zeolites is achieved through methods such as impregnation or ion exchange. However, these methods often lead to a non-uniform distribution of metal atoms, resulting in suboptimal catalytic performance due to agglomeration of metal atoms and poor dispersion. Such non-homogeneous distribution also leads to the inefficient utilization of noble metals, which is particularly concerning given the high cost of metals like platinum. An alternative method of metal incorporation is being explored to address these limitations. One promising approach involves the in-situ incorporation of metal ions during the zeolite synthesis process. This technique allows for directly integrating metal precursors into the zeolite matrix, leading to a more uniform distribution of metal atoms and potentially enhancing catalytic performance.

A notable example of this approach is demonstrated by Wang et al.[4] who successfully trapped palladium (Pd) clusters within nanosized silicate-1 MFI zeolite using $[Pd(NH_2CH_2CH_2NH_2)_2]Cl_2$ as a precursor and tetrapropylammonium as a template under hydrothermal conditions. These catalysts exhibited remarkable activity and high efficiency in hydrogen (H_2) generation. Building on this concept, the current study aims to synthesize single platinum atoms supported on MFI zeolite and evaluate their catalytic performance in hydrocracking processes.

The synthesis of the platinum complex, $[Pt(EtNH)_4]I_2$, will involve the addition of potassium tetrachloroplatinate (K_2PtCl_4) to an excess ethylamine solution, followed by characterization using ^{13}C and ^{1}H nuclear magnetic resonance (NMR) spectroscopy, as well as Fourier-transform infrared (FTIR) spectroscopy. Once synthesized, the platinum complex will be incorporated into the MFI synthesis gel and subjected to crystallization under controlled conditions to form single Pt atoms within the MFI zeolite framework. The resulting zeolite will be characterized using X-ray diffraction (XRD), nitrogen adsorption, and transmission electron microscopy (TEM). Finally, the catalytic performance of the prepared Pt-MFI zeolite will be tested in hydrocracking processes, with a focus on evaluating its efficiency and activity.

References:
1. Yang, X.-F, et al., (2013) Acc Chem Res. 46, 1740.
2. Weitkamp, J. (2012) ChemCatChem. 4, 292.
3. Iglesia, E; Wu, Z and Minkee, C. J (2010) Am Chem Soc. 132, 9129.
4. Wang, N et al. (2016) Chem Soc. 138, 7484.

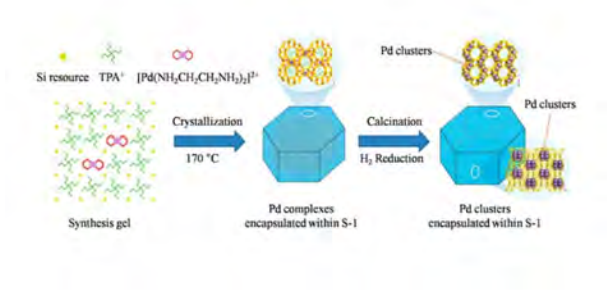

Figure 1. Confinement Synthesis of Pd Clusters within Nanosized Silicalite-1 Zeolite[4]

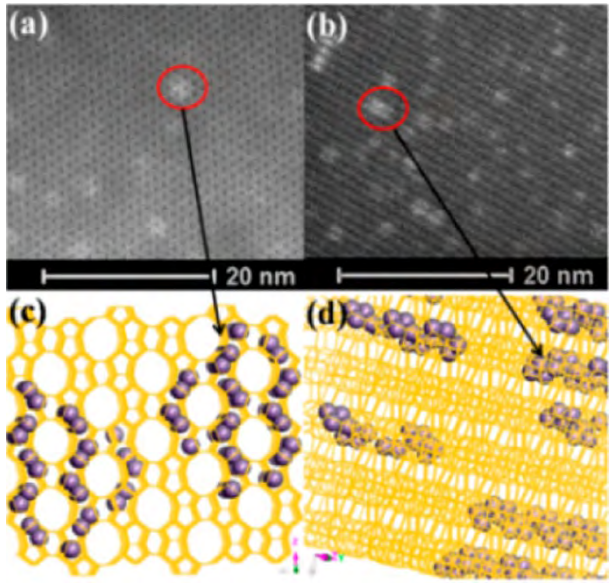

Figure 2. High-resolution STEM images (a,b) of the Pd/S-1-K sample and corresponding schematic crystallographic projections (c,d) of MFI viewed from different orientations.[4]

Corresponding author: patricia.kooyman@uct.ac.za

CHARACTERISATION OF Ti-6Ta-1.5Zr-0.2Ru-5Cu PRINTED BY LASER POWDER BED FUSION

N.S. Phala[1,2], C. Polese[2,3], J. Ciftci[4], T. Choma[4] and L.A. Cornish[1,2]

[1]School of Chemical and Metallurgical Engineering, University of the Witwatersrand, [2]DSI-NRF Centre of Excellence in Strong Materials, hosted by the University of the Witwatersrand, [3]School of Mechanical, Industrial and Aeronautical Engineering, University of the Witwatersrand, Johannesburg, [4]Warsaw University of Technology, Warsaw

Titanium alloys are used in biomedical applications for their strength, corrosion resistance, and biocompatibility[1]. Additive manufacturing, particularly laser powder bed fusion (LPBF), enables the production of complex, customised implants[2]. This study evaluated the effectiveness of 3D printing the Ti-6Ta-1.5Zr-0.2Ru-5Cu (mass%) alloy, which had been designed[3] and ultrasonically atomised[4], and printed as single tracks to determine the optimal conditions[5].

Ti-6Ta-1.5Zr-0.2Ru-5Cu (mass%) squares (10 x 10 x 1.2 mm) were manufactured using an AconityMIDI system. Manufacturing parameters were: 157.5 W laser power, 600 mm/s scanning speed, 0.15 mm beam diameter, 0.03 mm layer thickness, 0.05 mm hatching, and 0.2625 J/mm linear energy density, with 5 mm stripes and 0.1 mm overlap under argon flow. Remelting of the previous solidified layer was done with 280 W laser power, 3000 mm/s speed, and 0.08 mm beam diameter. Both LPBF and bulk composition (arc-melted bars prior to atomisation) samples were prepared by standard metallography, polished with colloidal silica, and characterised by SEM (Zeiss Sigma Field Emission Scanning Electron Microscope (FEG-SEM500)).

Fig. 1. shows the bulk sample with (αTi) needles in a eutectoid-like mixture of (αTi) and (βTi). Fig. 2. shows an LPBF square, with (αTi) along the (βTi) grain boundaries and as small precipitates in the matrix. The bulk sample had (αTi) needles as the primary phase, whereas the LPBF squares had primary (βTi), with (αTi) precipitated along the grain boundaries and as coarse Widmanstätten needles. Both samples had darker contrasts in the (αTi) phase, which were partially detached (αTi). However, Thermo-Calc[3] identified the phases as primary (βTi) with three phases at low temperatures: mainly (αTi) with small amounts of (βTi) and Ti_2Cu, although the latter was not identified here.

The LPBF sample had the targeted Zr composition, with lower Ti and Cu, and higher Ta and Ru. Conversely, the bulk sample had the targeted Ta composition, with lower Ti and Zr, and higher Ru and Cu, Table 1. The driving force for the difference in microstructure of the bulk and LPBF is the cooling rate, irrespective of the ~3 mass% difference in Ta and Cu, as shown in Table 1. LPBF had much higher cooling rates resulting in smaller grains, while the bulk had slower cooling rates and larger grains.

References:
1. Leyens, C. and Peters, M. (2003) Titanium and Titanium Alloys: Fundamentals and Applications. Cologne, WILEY-VCH Verlag GmbH & Co. KGaA, Weinheim.
2. Ni, J., et al. (2019) Mater Today Bio, 3, 1-18.
3. Spotose, L. (2023) MSc, University of the Witwatersrand
4. Phala, N.S. et al. (2023) MATEC Web of Conferences. 388, 08003
5. Phala, N.S. et al. (2024) MATEC Web of Conferences (submitted)

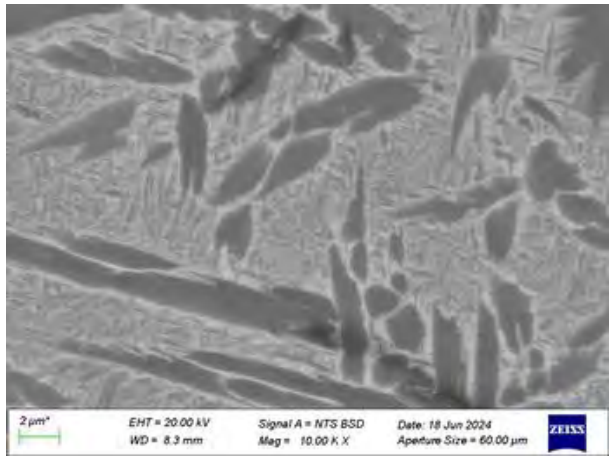

Figure 1. SEM-BSE image of Ti-6Ta-1.5Zr-0.2Ru-5Cu (mass%) bulk sample: (αTi) needles (dark) and (aTi) + (βTi) matrix (light and dark).

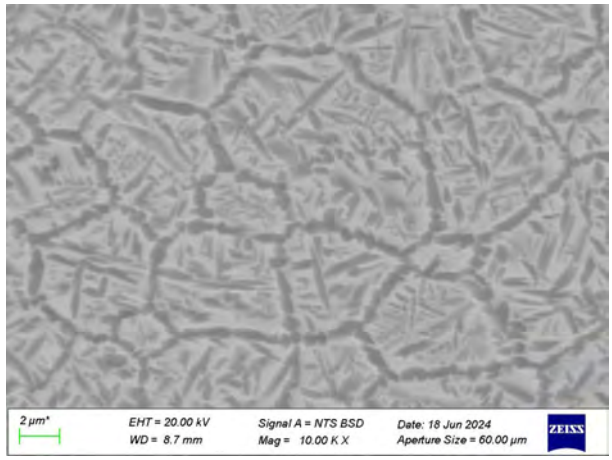

Figure 2. SEM-BSE image of Ti-6Ta-1.5Zr-0.2Ru-5Cu (mass%) LPBF square: (βTi) (light) and (αTi) (dark).

Table 1. EDX results of a bulk sample and LPBF squares of Ti-6Ta-1.5Zr-0.2Ru-5Cu (mass%).

Alloy	Ti	Ta	Zr	Ru	Cu
Bulk: Areal	84.4±0.4	6.4±0.2	1.4±0.2	0.4±0.2	7.4±0.3
LPBF: Areal	84.5±0.7	8.9±0.5	1.5±0.1	0.3±0.1	4.8±0.2

Corresponding author: 820850@students.wits.ac.za

EVOLUTION OF MICROSTRUCTURE AND UPCONVERSION LUMINESCENCE OF Tm,Yb-DOPED YF_3 DURING ANNEALING TO FORM Y_2O_3

P.J. Radebe[1] and R.E. Kroon[1]

[1]Department of Physics, University of the Free State, Bloemfontein

Up conversion involves the conversion of multiple low-energy photons into a single higher-energy photon[1]. Upconverting phosphors have applications in security printing, forensics, biomedical research and temperature sensing. Achieving efficient up conversion luminescence requires a suitable host material with low phonon energy[2] as well as stability. One such host material is YF_3. During annealing in air, it can oxidise and form Y_2O_3. In this study, the evolution of the microstructure and the up-conversion luminescence were evaluated as a function of annealing temperature.

YF_3 doped with Tm^{3+} (0.5 mol%) and Yb^{3+} (10 mol%) was prepared using the co-precipitation method with the aim to give blue up conversion emission when excited with an infrared laser at 980 nm. XRD analysis was carried out using a Bruker D8 Advance diffractometer with Cu Kα X-rays. Scanning electron microscopy was performed using a JEOL JSM-7800F Field Emission SEM (5 kV, 10 mm working distance) using the secondary electron detector. The up-conversion emission spectra of the obtained phases were measured by exciting them with a 980 nm infrared laser which is strongly absorbed by the Yb^{3+} ions. Energy transfer up conversion then occurs if the energy from multiple Yb^{3+} ions is transferred to Tm^{3+} ions and is combined to excite the Tm^{3+} ion to highly excited states from which blue photons can emitted during relaxation to the ground state.

Fig. 1 shows the powders annealed at (a) 500 °C, (b) 950 °C and (c) 1300 °C. The phase was identified as (a) orthorhombic YF_3, (b) rhombohedral YOF and (c) cubic Y_2O_3 using XRD. The YF_3 showed a non-uniform morphology with slightly irregular spherical shapes that appeared to be connected forming longitudinal structures with rough surfaces. The sample annealed to 950 °C evolved from YF_3 to YOF as a result of thermal decomposition and oxidation as well as growth, and the surfaces of particles were smoother. The morphology displays particles diffusing into one another during a self-assembly process controlled by the incorporation of oxygen into the crystal, causing the fluoride phase to transform into an oxyfluoride phase. Annealing at a higher temperature of 1300 °C allowed sufficient oxygen atoms to completely displace fluorine in the host, which resulted in the formation and growth of larger coalesced Y_2O_3 particles. The luminescence spectra showed distinct peaks in the blue region characteristic of Tm^{3+} ions, influenced by the crystalline phase. The findings showed that the YOF host material gave the highest up-conversion emission light intensity compared to the other host materials. This may be as a result of the mixture of oxygen and fluorine ions in this host more strongly perturbating the shielded 4f electrons of the Tm^{3+} ions which increases the transitions which are generally forbidden by the selection rules of quantum mechanics.

The evolution of YF_3 to Y_2O_3 can therefore be controlled by adjusting the annealing temperature. The phase transformation significantly affects the up-conversion properties, with YOF showing the highest emission intensity due to the combined influence of oxygen and fluorine ions on Tm^{3+} transitions.

References:
1. Sun, L.D., Dong, H., Zhang, P.Z. and Yan, C.H. (2015) Ann. Rev. Phys. Chem.66, 619.
2. Van Dijk, J.M.F. and Schuurmans, M.F.H. (1983) J. Chem. Phys. 78(9), 5317.

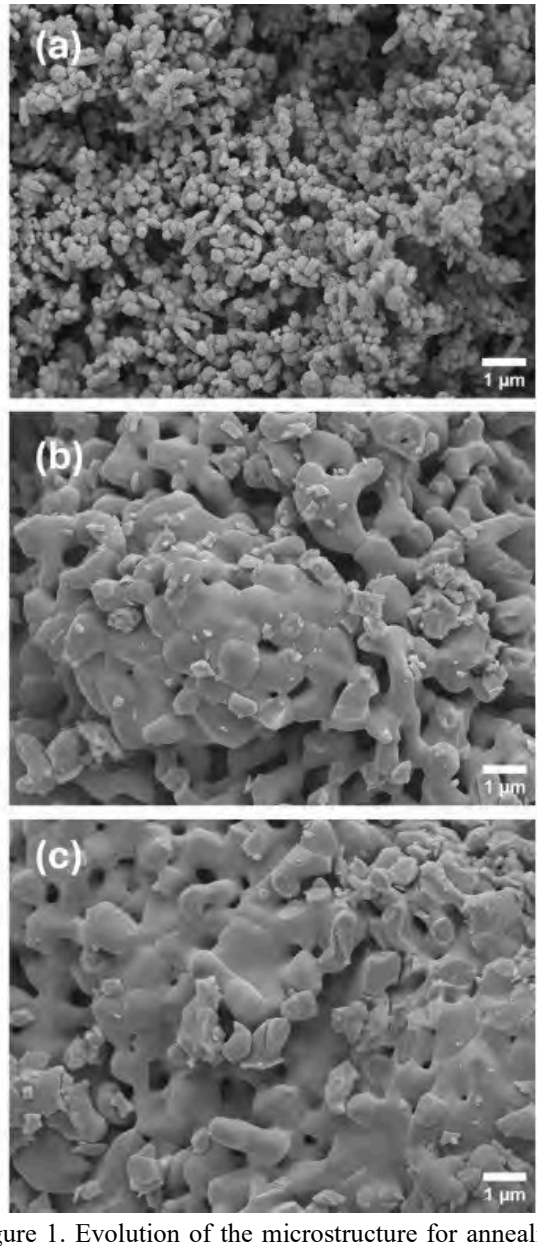

Figure 1. Evolution of the microstructure for annealing at different temperatures (a) 500 °C (b) 950 °C and (c) 1300 °C.

Corresponding author: KroonRE@ufs.ac.za

INSIGHTS INTO THE MORPHOLOGY-PERFORMANCE RELATIONSHIP TOWARDS LPG SENSITIVITY OF Co_3O_4/rGO GAS SENSORS LOADED WITH SILVER NANOPARTICLES

B.C. Tladi[1], Z.P. Tshabalala[1], R.E. Kroon[1], H.C. Swart[1] and D.E. Motaung[1]

[1]Department of Physics, University of the Free State, Bloemfontein

Semiconducting metal oxides (SMOs)-based gas sensors have grown in significance for the monitoring and control of hazardous, flammable, and explosive substances used in daily life and industrial processes. These sensors' poor selectivity and sensitivity to gases at low temperatures is one of its main weaknesses[1]. Surface modification with noble metals is an efficient approach for improving the sensitivity and selectivity of SMOs-based gas sensors at low operating temperatures. There are several ways to decorate the surface of host sensing materials with noble metals, which includes chemical reduction, gamma-ray irradiation, UV reduction, and sputtering[2,3]. To identify the successful surface modification, microscopy techniques such as TEM and EDS elemental mappings are vital, especially EDS elemental mapping as it gives clear confirmation and spatial information.

In this study, Co_3O_4-loaded on reduced graphene oxide (rGO) (Co_3O_4/rGO) was synthesized using microwave-assisted hydrothermal method. Ag nanoparticles of various amounts were then decorated on the surface of Co_3O_4/rGO using precipitation method. The Ag-decorated Co_3O_4/rGO nanocomposite was utilized for the monitoring and detection of liquid petroleum gas (LPG) at low functional temperatures.

Microstructural properties were evaluated using a JEM-F200 HR-TEM fitted with an Oxford Instruments ULTIM MAX EDS detector. The HR-TEM analysis revealed distinct lattice fringes with interplanar spacings corresponding to crystal planes of Co_3O_4 and Ag. The qualitative elemental mapping shown in Fig. 1, revealed adhesion of a few Ag nanoparticles on the surface of Co_3O_4/rGO. Furthermore, the particle size of the Ag NPs as deduced from Fig.1, was estimated using ImageJ and found in the range of 13-15 nm. Gas sensing studies revealed that, at low temperatures of 100 °C, the Ag decorating greatly enhanced the sensitivity and selectivity towards LPG. At an operating temperature of 100 °C, the sensor loaded with 0.5 wt% Ag exhibited a very consistent and selective response to LPG. Ag decorated onto the Co_3O_4/rGO sensor's surface was responsible for the sensor's notable improvement in LPG detection. As a result, the sensor surface developed numerous active sites i.e. defects such as vacancies, dislocations, etc., which greatly contributed to the chemisorption of more LPG molecules due to the spillover effect, and an increasing sensitivity.

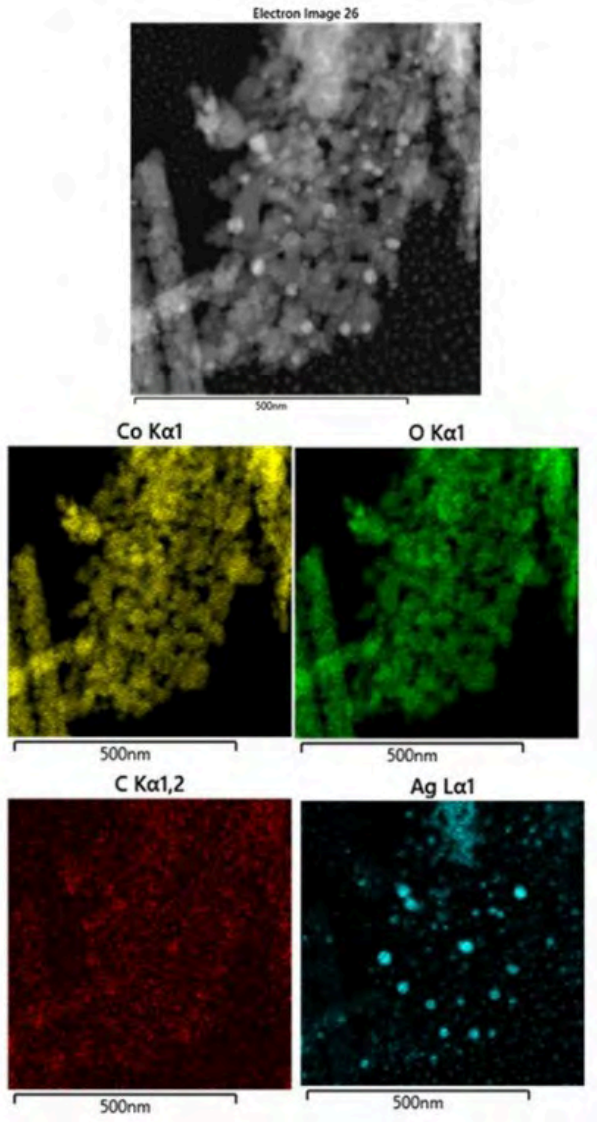

Figure 1. EDS elemental mappings of Co_3O_4/rGO Ag decorated at 2 wt%.

Corresponding author: TladiBC@ufs.ac.za

References:
1.Dey, A., (2018) Mater. Sci. Eng. B 229, 206.
2. Zhu, L.Y., Ou, L.X., Mao, L.W., et al. (2023) Nano-Micro Lett. 15, 89.
3. Moon, Y.K., Jeong, S.-Y., Kang, Y.C., Lee, J.-H., (2019) ACS Appl. Mater. Interfaces 11, 32169.

PREPARATION OF $SrVO_3$ THIN FILMS USING SPIN COATING

E. Lee[1,2], R.A. Harris[2], J.J. Terblans[2] and H.C. Swart[2]

[1]Centre for Microscopy, University of the Free State, [2]Dept. of Physics, University of the Free State, Bloemfontein

Transparent conductive oxides (TCO) thin films are of great importance in commercial electronic devices[1]. This is due to their transparency in the visible light region while still being electrically conductive. Currently indium tin oxide (ITO) films are the most widely used TCOs. However, indium resources are of great concern due to its increasing scarcity, resulting in limited supply and higher cost. Early reports showed that $SrVO_3$ thin films with a thickness of 12 nm displayed a resistivity comparable to that of ITO with a transparency of 80 % in the visible region[2]. More importantly, the cost of the raw materials is significantly lower than that of ITO. This study focuses on the preparation of the glass substrate and strontium vanadate thin film using spin coating.

A 0.2 M strontium solution was prepared by dissolving strontium acetate in distilled water. Similarly, a 0.2 M vanadium solution was prepared by dissolving vanadium acetylacetonate in a 10 % ethanol to distilled water solution. The spin coating solution was obtained by combing the strontium and vanadium solution in equal parts. To improve the wettability of the glass substrate, treating of the glass was performed through two techniques, hydrolysis and $KMnO_4$ submersion. Hydrolysing of the substrate was done by suspending it in a 200 mL hydrothermal reactor containing 70 mL of distilled water and heated at different temperatures. While the $KMnO_4$ treated substrate was prepared by submersing it for 80 min in a 40 mL $KMnO_4$ solution (5 mM) containing 400 µL of methanol, followed by distilled water rinsing then sonication in distilled water for 10 min in an ultrasonic bath. $SrVO_3$ thin films were prepared on both untreated and treated substrates using spin coating. The coating parameters were kept constant cross all substrates: rotation speed (2000 RPM), ramping rate (500 RPM/s), spin duration (30 s), solution volume (100 µL), substrate size (25 mm x 25 mm) and dying (70 °C, 1 min). This coating was repeated 5 times. Transmittance analysis was performed using the PerkinElmer Lambda 950 UV/VIS spectrometer and Thermo Scientific NICOLET 6700 FT-IR. The HR-TEM micrograph and EDS was obtained using the JEOL F200 and Oxford ULTIM MAX, respectively.

Fig. 1(a) shows the transparency of the substrate before and after treatment. The substrate treated through hydrolysis showed a decrease in its transparency compared to an untreated substrate. Whereas the substrate treated using $KMnO_4$ showed little to no change to its transparency compared to the untreated substrate. The change in transparency of the substrate prepared using the hydrolysis technique can be attributed to the amount of hydroxyl group present on the substrate as seen in Fig. 1(b). During hydrolysis the water attacks the Si-O-Si bonds forming Si-OH bonds on the surface of the substrate, and with an increase in temperature this reaction can penetrate and spread into the glass substrate changing its internal composition leading to changes its transparency. To confirm the presence of a strontium vanadate thin film in addition to what was visually observed, a cross section of the sample was prepared. An EDS elemental map was measured and shown in Fig. 2. The elemental map showed a uniform distribution of strontium and vanadium, and the film thickness was 14 nm.

$SrVO_3$ thin films were successfully prepared using the spin coating technique. Treatment of the glass substrate was essential to improve the wettability of the substrate and treatment using $KMnO_4$ was the most optimal in preserving the transparency of the substrate.

References:
1. Jayathilake, D.S.Y. and Mirmal, P.T.A. (2018) J. Mater. Chem. Eng., 1, 1
2. Frank, G. and Höstlin, H. (1982) Appl. Phys. A Soldis Surfaces, 27, 197

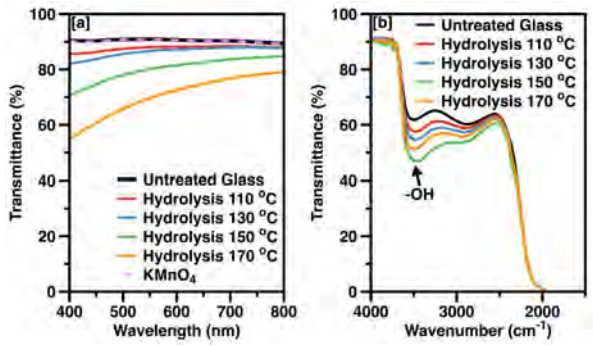

Figure 1. (a) UV-VIS spectrum and (b) FTIR spectrum of untreated and treated glass substrates.

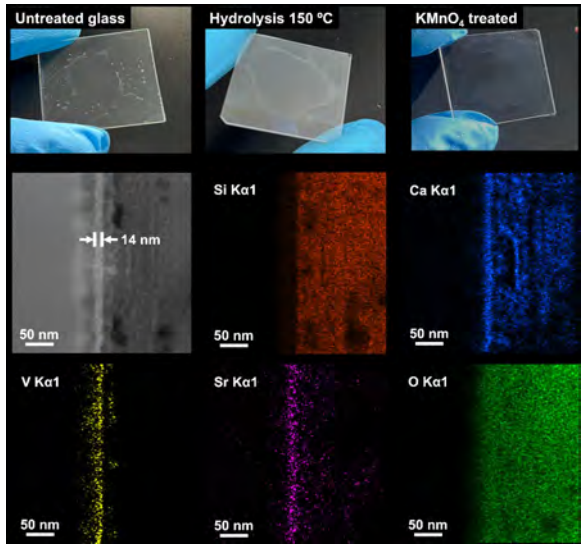

Figure 2. Photographs of the $SrVO_3$ thin film on treated vs untreated substrates and an HR-TEM bright field micrograph with the EDS mappings of the thin film cross section on a hydrolysed substrate.

Corresponding author: LeeE@ufs.ac.za

PHASE EVOLUTION AND SURFACE MORPHOLOGY IN COPPER-INDIUM THIN FILMS: STABILITY OF CO-EVAPORATED FILMS

L.E. Makoloane[1], J.J. Terblans[1], S. Cronje[1] and H.C. Swart[1]

[1]Physics Department, University of the Free State, Bloemfontein.

Co-evaporation is a promising technique for alloy preparation, particularly in advanced applications such as solar cells and electronics[1], where thin films are doped by driving the dopants into the thin films by means of diffusion at a high temperature. When the dopants have a low melting point, like in the case of indium (In) and tin (Sn), the high-temperature annealing causes the dopants to evaporate. A stepwise annealing program can be followed to prevent the loss of dopants; however, it is a time-consuming method as it depends on gradual phase formation starting from low annealing temperatures where diffusion is slow[2]. With co-evaporation, a thin film is grown, and the dopant is included (uniformly at the required doping concentration) during film growth. Annealing of co-evaporated thin films can be initiated at a higher temperature with a reduced time.

These co-evaporated films are artificially homogeneously mixed and are metastable. Phase separation sometimes occurs during co-evaporation or sample storage at room temperature. The phase separation leads to changes in composition and surface morphology over time. This study investigated the phase stability of co-evaporated Cu-In thin films with an In concentration that ranged from 10 to 30 at% In. The thin films were aged at room temperature for 3 years, and the surface morphology was monitored using a JEOL JSM7800F Field of Emission SEM at 10 kV. XRD analysis was utilised to identify and assess the phase evolution during ageing.

From XRD analysis of the films directly after preparation revealed the presence of a $Cu_{11}In_9$ phase in all the films. The broadness of the $Cu_{11}In_9$ reflection, as shown in Fig. 1, indicates the presence of fine crystallites indicative of a smooth surface. SEM analysis of these films confirmed smooth, featureless surfaces for the 10 and 20 at % In films. The SEM image, Fig. 2(a), of the 30 at% In film, displayed small grain-like structures on the surface and the XRD data indicated that the $Cu_{11}In_9$ phase was still present in the film.

The same films were re-examined after 3 years of ageing (storage at room temperature). The films with 10 and 20 at% In remained stable. The 30 at% In film showed the formation of In-rich particles randomly scattered on the surface on a uniform background, an indication of phase separation[3,4]. XRD analysis of this film confirmed the formation of a Cu_2In phase during ageing and SEM analysis revealed particles, as can be seen in Fig. 2(b), present on the surface. EDS analysis of both the background and the particle's ROI suggests that the particles are rich in Indium. The XRD reflection peak corresponding to the $CuIn_2$ phase was also observed in the aged sample, confirming that the particles are the $CuIn_2$ phase.

References:
1. Gossla, M., Metzner, H. and Mahnk, H.E. (1999) J. Appl. Phys. 86 (7), 3624.
2. Madito, M.J. *et al.*, (2012) The Segregation from polycrystalline Copper crystals. University of the Free State, South Africa.
3. Bahari Z., *et al.* (2003) Thermochem. Acta 404, 131.
4. Dzionk Z., *et al.* (1995) J. Appl. Phys. 78 (4), 2151.

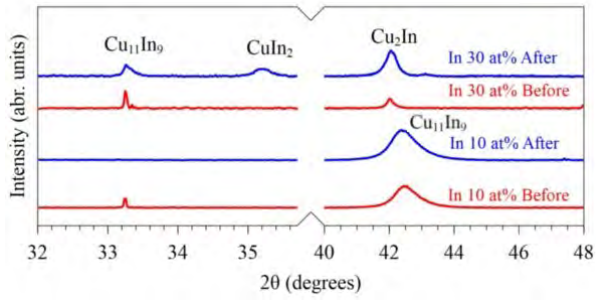

Figure 1. The XRD reflection data of the co-evaporated Cu-In films containing 10 and 30 at% In before (in red) and after ageing (in blue).

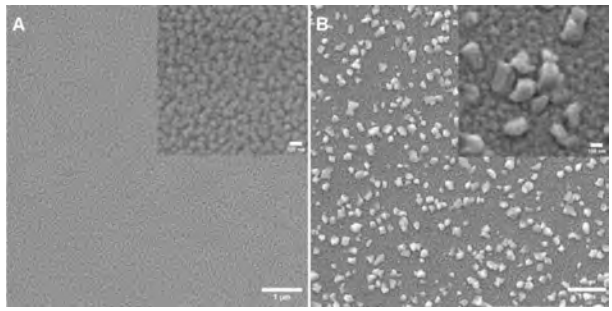

Figure 2. SEM images of the 30 at% In samples with 100 nm thickness. Image (a) is the before ageing, and image (b) is after 3 years of ageing at room temperature.

Corresponding author: eric.makoloane@gmail.com

THE STRUCTURAL AND MORPHOLOGICAL STUDY OF MASK-ASSISTED DEPOSITION OF ZnO/Au MICRO-TOWERS

D.T. Mashilo[1], R.A. Harris[1] and H.C. Swart[1]

[1]Department of Physics, University of the Free State, Bloemfontein

Nanomaterial-based photovoltaics have been at the forefront of alternative research meant to replace traditional thin film-based photovoltaic cells (PVCs). Zinc oxide (ZnO) has excellent light absorbing properties in the ultraviolet range[1]. These properties can improve the power efficiency of a photovoltaic cell[2,3]. This study focuses on the change in crystallographic structure and surface morphology during the formation of ZnO/Au micro-towers.

The sample was prepared by evaporating a thin layer of gold (Au) for 5 minutes (~ 200 nm thickness) using a sputter coater onto an oxidized silicon substrate. The deposition was done for all samples. Then ZnO thin films were deposited using pulsed laser deposition (PLD) with the aid of a mask with 1000 mesh size and 25 um pitch size to form nearly 1 000 discrete ZnO micro-towers per mask used. The ZnO films were deposited at different intervals of 1 minute, 5 minutes, 10 minutes, 15 minutes, 20 minutes and 25 minutes.

X-ray diffraction (XRD) of all deposited ZnO films showed a preferential orientation of (002) along the c-axis perpendicular to the surface of the substrate. As the deposition time intervals increased, the sharp peak intensities of ZnO are also increasing but it is not the case with Au peaks. At 20 minutes, the Au peaks are decreasing, which could suggest that ZnO forms more crystalline structures than Au. Scanning electron microscopy (SEM) only showed (figure 1a and b) morphologies of samples with PLD intervals of 5-20 minutes deposition time, of which particles of various shapes and sizes formed with increasing deposition intervals. SEM micrographs of regions consisting mainly of Au, showed a change in morphology that was later characterized to be Si particles using energy dispersive spectroscopy (EDS). The surface roughness characterized by atomic force microscope (AFM) increased with increasing deposition intervals, with average roughness values of 40.92 nm, 37.39 nm, 69.17 nm 110.52 nm. Reflectance spectra obtained using ultraviolet-visible spectroscopy (UV-Vis) showed an undulating interference pattern which may be attributed to the surface roughness of the deposited films. Since rough surfaces disrupt the phase consistency of the wave, leading to variation in interference pattern.

The ZnO/Au micro-towers were successfully deposited using the masked PLD technique, as the surface morphology and topography of these micro-towers indicated a direct relationship between surface roughness and deposition intervals. Further device characterization is necessary for photovoltaic cell application.

References:
1. Wang, N and Jiang, D (2021) J Mater Sci. 56(9), 5708.
2. O. Cardozo et al. (2024) Journal of Materials Science: Materials in Electronics. 35(12), 876.
3. A. Wibowo et al. (2020) Royal Society of Chemistry 10(70), 42838.

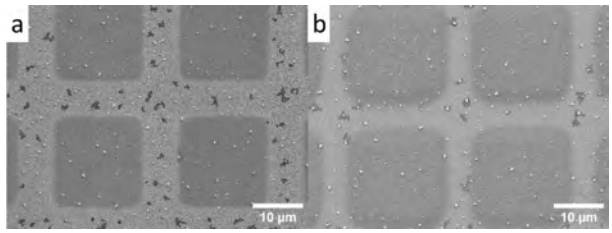

Figure 1. SEM micrographs of ZnO/Au micro-towers deposited at various PLD intervals (a) 5 minutes (b) 20 minutes.

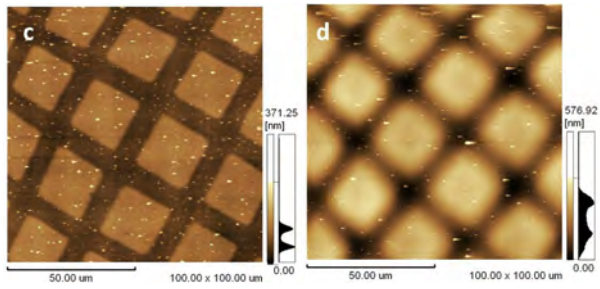

Figure 2. AFM micrographs of ZnO/Au micro-towers deposited at various PLD intervals (c) 5 minutes (d) 20 minutes.

Corresponding author: mashilodt@gmail.com

STUDIES ON THERMAL PROPERTIES OF SPARK PLASMA SINTERED Ti-48Al-2Cr-2Nb ALLOY

M.R. Mphahlele[1], E. Olevsky[2] and P.A. Olubambi[3]

[1]Department of Mechanical Engineering, Durban University of Technology. Durban [2]Powder Technology Laboratory, College of Engineering, San Diego State University, San Diego, CA, United States, [3]Department of Metallurgical Engineering, University of Johannesburg, Doornfontein

To the delight of researchers and scientists, intermetallic titanium aluminide alloys based on the gamma phase are considered to have the potential to meet the requirements of the revolutionary designs essential in modern-day industries. Other payoffs of gamma TiAl include low diffusivity, high thermal conductivity, high temperature-strength retention, low thermal expansion, good structural stability, high hardness, resistance against corrosion, creep, and high ignition[1] when compared with conventional titanium alloys. These properties make TiAl an attractive alternative to Ti-Ni-based superalloys for utilization in aerospace applications, particularly aircraft engine parts operating in the temperature range of 400 – 800 °C[2]. However, for TiAl to be successfully utilized as a structural material in high-temperature applications, it is essential to have a comprehensive understanding of the thermal stability and structural properties of titanium aluminide alloys at high temperatures. This study aimed to investigate the thermal and microstructural properties of SPSed TiAl alloys with a view of their potential use in high-temperature applications.

The laser flash analyzer (LFA) method was done using LFA 427 to determine thermal diffusivity, conductivity, and specific heat of spark plasma sintered Ti-48Al-2Cr-2Nb intermetallic alloy. Temperatures of 25, 300, 600, and 900 °C were used for all tests in an argon atmosphere. Thereafter, scanning electron microscopy-back scatter (SEM-BS), supplied by JEOL, was used to conduct microstructural analysis on the samples. Quantitative analysis of the SEM-BS images was carried out using Phython software to determine the volume of different alloy structures.

The LFA results (Fig. 1) show that both the thermal diffusivity and thermal conductivity first decreased with an increase in temperature up to 300 °C, followed by an increase with increasing temperature. The high thermal conductivity and diffusivity of the TiAl alloy at 600 and 900 °C are owed to the intrinsic low density of TiAl alloys. Generally, diffusivity is proportional to thermal conductivity and inversely proportional to density[2]. SEM images in Fig. 2 & 3 show that while the duplex structure is maintained, it is evident that the dark phase (residual γ-phase) increases with an increase in temperature. It should be noted that the microstructure influences the material's conductivity, and duplex microstructure is characterized by excellent thermal conductivity compared to the lamellar structure.

References:
1. Kim, Y.W. and Dimiduk D.M. (1991). Jom. 43, 40.43, 40.
2. Biswas, R., Kuar A. and Mitra S. (2014). Optics and Lasers in Eng. 60, 1.

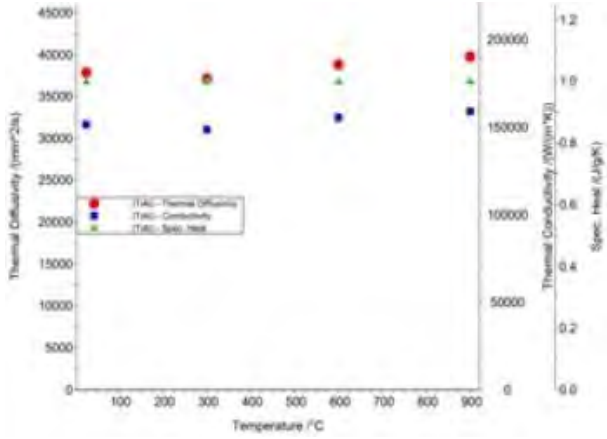

Figure 1. Thermal properties of SPSed Ti-48Al-2Cr-2Nb.

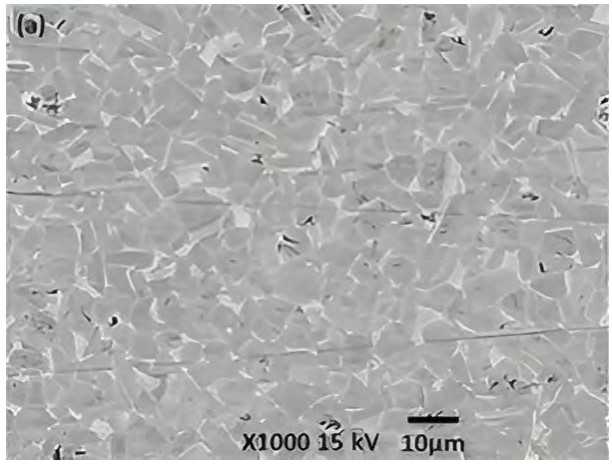

Figure 2. SEM image of TiAl alloy at 25 °C.

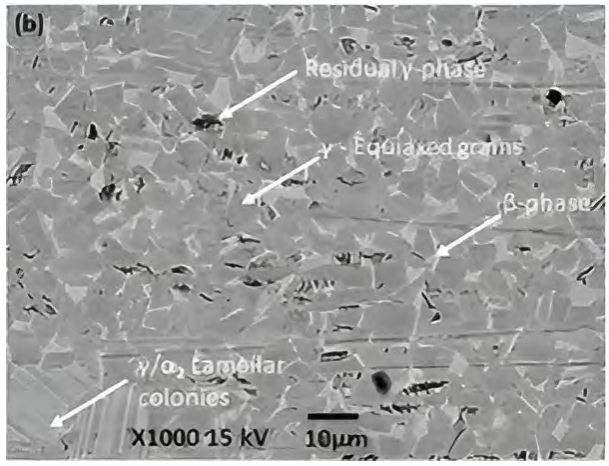

Figure 3. SEM images of TiAl alloy at 300 °C.

Corresponding author: ramimphahlele@gmail.com

SYNTHESIS AND CHARACTERISATION OF ZIRCONIUM SILICIDE LAYERS ON ZIRCONIUM ALLOY FOR NUCLEAR REACTOR APPLICATION

S. Ngongo[1], A. Janse van Vuuren[1] and J.H. Neethling[1]

[1]Centre for HRTEM, Nelson Mandela University, Gqeberha, South Africa

Due to the fast-growing demand for energy and concerns about climate change it is necessary for nuclear energy to play a greater role, in combination with other energy sources, to satisfy the future energy needs of mankind[1]. Given that energy generation currently accounts for 66% of the worldwide greenhouse gas emissions, nuclear energy is considered as an important resource in the management of atmospheric greenhouse gases, since nuclear power has very low carbon emissions[2]. The fission process which is the source of power in nuclear energy production is also the origin of key hazards in the operation of nuclear power plants.

One of the main objectives in nuclear industry is improving the safety, reliability and economic viability of fission reactors, factors that negatively affect the fuel cladding material must be resolved. In certain reactors Zirconium alloy is the main physical barrier between the coolant system and the fuel pin[3]. One of the solutions is to find the suitable coating for the zirconium alloy which would reduce its oxidation rate. When the oxidation takes place on the water side of zirconium alloy, hydrogen is released into the coolant and some of the hydrogen is absorbed by the zirconium alloy leading to formation of zirconium hydrides which are brittle in nature[4]. An ideal coating must improve the reaction kinetics of the fuel tube with steam which should suppress hydrogen generation and related hydrogen gas explosions under accident conditions. Zirconium silicide has been considered since it is known for its outstanding high temperature oxidation resistance. This oxidation resistance is due to the formation of dense silica layer which has self-healing properties[5].

This paper reports some preliminary results of the microstructure of zirconium silicide layers synthesized on zirconium alloy. Samples of 8mm by 2 mm were cut from a zirconium alloy tube and used as the substrate for zirconium silicide surface layers. This process was done by annealing the zirconium alloy in contact with silicon powder at temperatures ranging between 1000 to 1400 ºC for 4 - 8 hours in a Webb 89 furnace under argon gas environment. The annealed samples were sectioned using a diamond wire saw, mounted using epoxy resin and polished down to 1 um finish. The samples were investigated using a JEOL JSM 7001F scanning electron microscope using mainly backscattered electron (BSE) imaging. Elemental mapping was performed by energy dispersive X-ray spectroscopy (EDS). A Helios NanoLab 650 FIBSEM was also used to cut TEM lamellae from specific areas of interest, and these were investigated in a JEOL 2100 LaB_6 TEM operated at 200 kV.

The BSE SEM micrograph in Figure 1 shows a double layer of zirconium silicide that were successfully formed after annealing the zirconium alloy in contact with silicon powder at 1200 °C for 4 hours. These layers will act as a double protection layer against oxidation during operational temperatures of a nuclear reactor. TEM lamellae were also extracted on both silicide layers to determine the type of silicide which formed. SAD patterns shown on Figure 2 suggest that Zr_3Si_2 formed in the area marked as A and Zr_2Si formed in the area marked as B. The Zirconium silicide layers appeared fully dense with no indications of porosity.

The results suggest that fully dense zirconium silicide layers can be successfully produced through this simple technique of annealing zirconium alloys in contact with silicon.

References:
1. Yvon, P., Carre, F. (2009) JNM 385(2) 217.
2. Zinkle, S.J., Was, G.S. (2013) Act. Mater. 61(2) 735.
3. Kim, H.H. *et al.* (2010) J. Mater. Sci. Technol. 26(9) 827.
4. Motta, A.T., Chen, L.Q. (2012) J. Min. Met. Mater. Soc. 64. 12.
5. Cho, I.J., *et al.* (2010) J. Chem. Eng. 165, 728

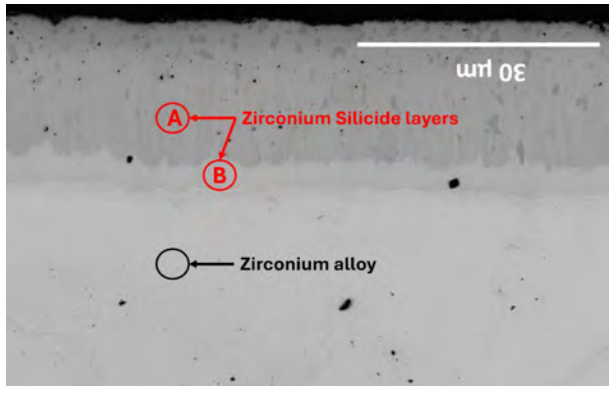

Figure 1. BSE SEM micrograph showing a double layer of zirconium silicide successfully formed on zirconium alloy substrate.

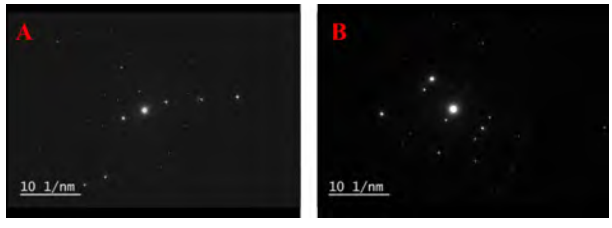

Figure 2. SAD patterns from samples corresponding to area A and B which correspond to Zr_3Si_2 and Zr_2Si respectively.

Corresponding author: ngongosamkelo@gmail.com

ALLOYING INTERMETALLIC $AuIn_2$ AND $AuGa_2$ WITH VARIOUS MACRO AND MICRO ALLOYING ELEMENTS

A. Hefer[1,2] and LA. Cornish[1]

[1]School of Chemical and Metallurgical Engineering, University of Witwatersrand, [2]Rand Refinery (Pty) Ltd

Purple GoldTM[1], a 19ct gold alloy developed in the early 2000s, opened new possibilities for jewellery production. Rand Refinery aimed to produce a workable coloured alloy for the industry. However, coloured gold alloys with aluminium, indium, or gallium are considered undesirable by jewellers due to their brittleness from fluorite-like crystal structures[2]. Blue gold was produced with indium or gallium as the main alloying element, with intermetallic compounds $AuIn_2$ and $AuGa_2$ contributing to colouration through strong covalent bonds. These brittle compounds, along with challenges like oxidation, coarse grain size, insufficient strength, work hardening, and low corrosion resistance, require careful design considerations[3].

The methodology followed up today involved producing a reference sample of 99.99% gold and two baseline AuX_2 (X = In or Ga) samples with approximately 55 wt% indium and 45 wt% gallium, equating to 12 and 14 carat gold alloys. The macro alloying synthesis stage was completed, producing six samples with a chemical composition of AuX_2Z (X = In or Ga, Z = Ni, Pt, Pd). All samples underwent XRD and SEM-EDS analysis, micro-Vickers hardness testing, and CIELAB colour testing to determine the sample with the best blue hue.

The colour achieved by alloying gold and indium or gallium was a light blue. Although it was not an intense blue, initial feedback from the jewellery industry was that by combining this colour with a bright white colour gemstone, the contrast achieved would be attractive and unique.

The CIELAB results showed that the gold-indium-palladium alloy (43% Au, 55% In, 2% Pd) had the highest blue value. Indium formed a more homogeneous alloy with gold compared to gallium, which caused surface patterns and an oxidation layer, potentially compromising functionality (Figures 1 and 2 respectively). Nickel made the alloy extremely brittle, increasing hardness to 145 HV_1, while pure gold (99.99%) had a hardness of 45 HV_1.

Alloying gold with indium and gallium produced a light blue alloy, which could offer a unique contrast with bright white gemstones. However, the indium-containing alloy was more homogeneous and attractive. CIELAB tests identified the gold-indium-palladium alloy (compromising 43% Au, 55% In and 2% Pd) to have the highest blue colour value which will be used further.

References:
1. Loh, P.C. 2001. Jewellery alloy compositions, Singapore Patent No. US6929776B1.
2. Grimwade, M. 1985. Introduction to Precious Metals, 1st Edition, Butterworth & Co.
3. Van der Lingen, E. 2014. Aspects of coloured precious metal intermetallic compounds, The Journal of the Southern African Institute of Mining and Metallurgy, 114, pp 137

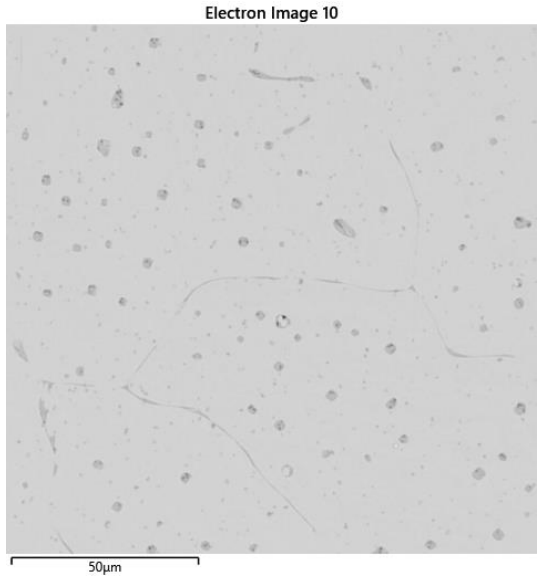

Figure 1. A secondary electron image of the $AuIn_2$ sample at a magnification of 1000x shows a surface pattern that differs from the $AuGa_2$ sample.

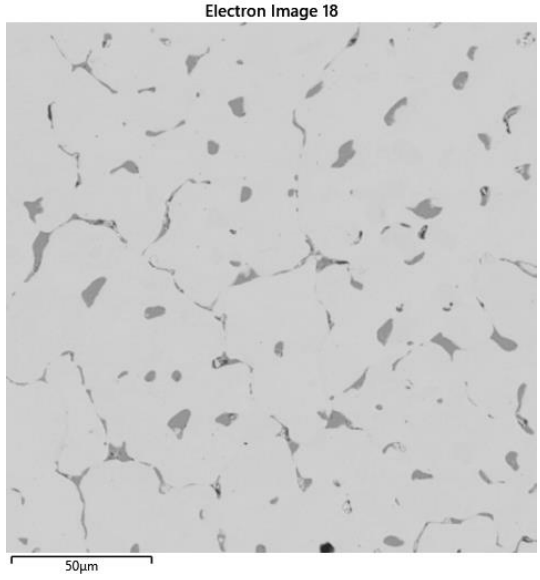

Figure 2. A secondary electron image of the $AuGa_2$ sample, magnified at 1000x, illustrates the surface pattern formed by Gallium, identifiable as the dark grey regions.

Corresponding author: amandah@gold.co.za

ÅNGSTROM

Electron Microscopy

- Scanning Electron Microscopes (SEM)
- Transmission Electron Microscopes (TEM)
- Electron Microprobes (EPMA)
- Nuclear Magnetic Resonance (NMR)
- Electron Spin Resonance (ESR)

Raman / AFM

- Confocal Raman Microscopes
- Scanning Probe Microscopes (SPM)
- Scanning Near Field Optical Microscopes (SNOM)
- Correlative Microscopes
- Atomic Force Microscopes (AFM)

Imaging & Spectroscopy

- Digital Cameras
- Electron Energy Loss Spectroscopy (EELS)
- Cathodoluminescence (CL)

Specimen Preparation

- Carbon Evaporators
- Sputter Coaters
- Microscopy Consumables & Tools

sales@angstrom.co.za | www.angstrom.co.za | +27 (0) 11 462-1347

WITec focus innovations | GATAN | JEOL Solutions for Innovation | Quorum | agar scientific